A multi-wavelength study of intermediate-age open clusters

Nevil Shah

A dissertation submitted for the partial fulfilment of
BS-MS dual degree in Science

Indian Institute of Science Education and Research Mohali
April 2020

Certificate of Examination

This is to certify that the dissertation titled "A multi-wavelength study of intermediate-age open clusters" submitted by Mr. Nevil U. Shah (Reg. No. MS15067) for the partial fulfilment of BS-MS dual degree program of the Institute, has been examined by the thesis committee duly appointed by the Institute. The committee finds the work done by the candidate satisfactory and recommends that the report be accepted.

Dr. H. K. Jassal Dr. S. Mahajan Prof. J. S. Bagla Prof. Kulinder Pal Singh
(Co-Supervisor)   (Supervisor)

Date: April   , 2020

Declaration

The work presented in this dissertation has been carried out by me under the guidance of Prof. Kulinder Pal Singh at the Indian Institute of Science Education and Research Mohali.

This work has not been submitted in part or in full for a degree, a diploma, or a fellowship to any other university or institute. Whenever contributions of others are involved, every effort is made to indicate this clearly, with due acknowledgement of collaborative research and discussions. This thesis is a bonafide record of original work done by me and all sources listed within have been detailed in the bibliography.

Nevil U. Shah

(Candidate)

Date: April 25, 2020

In my capacity as the supervisor of the candidate's project work, I certify that the above statements by the candidate are true to the best of my knowledge.

Prof. Kulinder Pal Singh
(Supervisor)

Acknowledgment

List of Figures

List of Tables

Contents

Abstract

Star clusters are ideal platforms for the study of evolution of X-ray activity as a function of stellar age and binarity, and thus categorising them in different classes. We present a comprehensive multiwavelength study of an open star cluster, NGC2527, by using data from three space observatories: X-rays and UV from XMM-Newton, UV from Swift UVOT and visible from Gaia. Cluster membership of stars and their photometry are taken from Gaia and cross-matched with XMM and UVOT detections. We estimate the age of NGC2527 as ∼630 Myr, reddening as E(B−V)=0.13 mag, and a distance of 642±30 pc using PARSEC isochrones. We detect 5 sub-subgiants and 5 bandgap stars, which defy single star evolution. We estimate the temperature, mass, radius, and luminosity of 53 single stars and 10 potential binary stars using a python code which fits single and composite Kurucz spectra to broad-band Spectral Energy Distribution. Among the 12 coronally active X-ray emitting stars, we find 5 are potential RS CVn type binaries, 2 are potential FK Comae type of red giant branch (RGB) stars, and 5 are main sequence (MS) stars with high coronal activity. Members with strong UV emission comprise of 1 RGB star, and several MS stars with UV excess suggestive of chromospheric activity. Based on comparison with other clusters, we tentatively suggest that X-ray luminosity of both RS CVn and contact binaries increases with age suggesting more active binaries are present in older clusters as compared to younger clusters. This study suggests possible presence of W UMa and FK Comae type stars in younger (age≃630 Myr) clusters.

To extend this work further, we proposed observations with the AstroSat UVIT and XMM-Newton of two open clusters: NGC 2506 and NGC 6940 respectively, both of which were accepted. NGC 2506 has already been observed and we present a preliminary analysis. . A detailed study of these clusters will allow us to connect and bridge gap in between various stages of binary stellar evolution. It will also provide information on the fundamental mechanism of formation and emission from various peculiar binaries such as blue stragglers, red stragglers, sub-subgiants, MS + extremely low mass WD binaries, etc. We give a summary of the objectives and expected results from the proposed observations.

Chapter 1

Introduction

1.1 Star clusters

A star cluster is a group of coeval population of stars that are formed from the same molecular cloud. Star clusters present a snapshot of stars of similar age, chemical composition, and distance, making them ideal laboratories to study stellar evolution. They can be identified by the sudden increase in the concentration of stars as compared to the field. They are found in the halo, disk and bulge of galaxies, as shown in Fig. 1.1. Star clusters can be broadly classified into two main categories: open cluster (OC) and globular cluster (GC).

Figure 1.1: Location of open cluster and globular cluster in the halo, disk and bulge of a galaxy. Image credits - European Space Agency

1.1.1 Open clusters

Open clusters (OCs) of stars are fundamental objects for the study of effects of stellar evolution on their chromospheric and coronal activities. They are primarily found in the disk of a galaxy and are also known as galactic clusters. Trumpler (1930) performed the first comprehensive study of OCs. The age of stars in OCs varies from 10^6 years (recently formed stars) to 6×10^9 years. OCs typically contain a few tens to hundreds of loosely arranged stars located within a radius

of about 5 pc. The stars present in OCs usually belong to Population I type of stars, that are metal-rich stars. The typical number density of stars in OCs is 0.1-10 pc^{-3}. OCs contain mostly intermediate to low mass stars, making them ideal targets to study the evolution of these stars.

1.1.2 Globular clusters

Globular Clusters (GCs) of stars have a tightly bound spherical distribution of stars. They are presumed to be the first objects formed in a galaxy. The age of the stars in GCs is about 10-15 billion years. These stars belong to the class known as Population II, which are very metal poor as compared to the Sun. GCs are typically found in the halo and the bulge of a galaxy. They contain thousands of stars within a radius of 25-50 pc. Since GCs are the oldest objects in the galaxy, they are ideal targets to study the stellar evolution of Population II stars and understand the formation of a Galaxy.
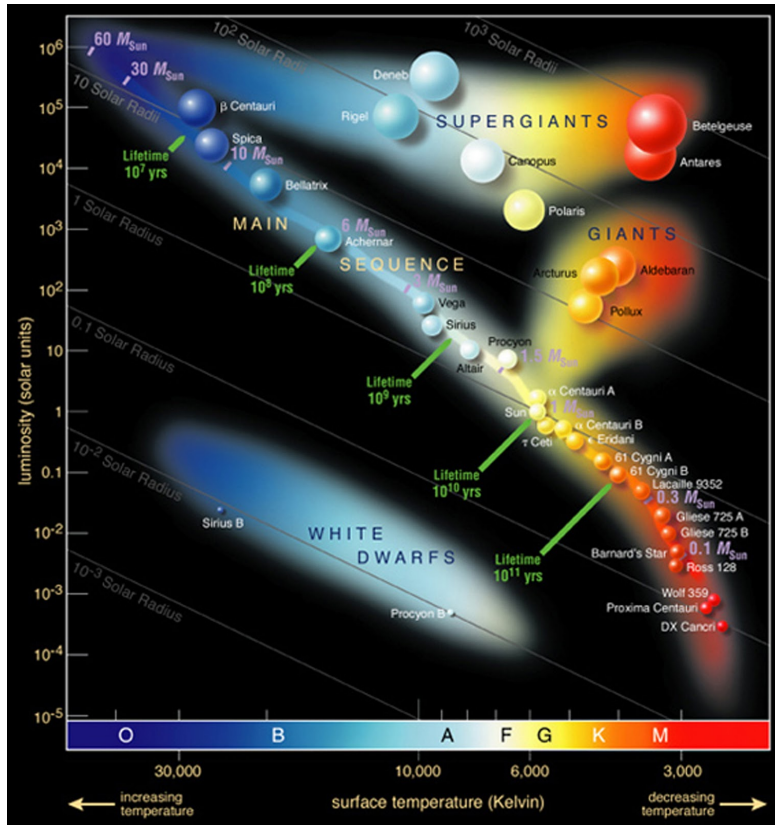
Figure 1.2: Position of stars in H-R diagram in various evolutionary phases.

1.2 H-R diagram of star clusters

The Hertzsprung-Russell (H-R) diagram is a basic plot to study the stellar evolution of stars. It was independently developed by the Danish astronomer E. Hertzsprung in 1911 and the American astronomer H. N. Russel in 1913. It shows the relationship between the luminosity (L/L$_\odot$) versus effective temperature (T$_{eff}$)

of stars, also known as the theoretical H-R diagram. It can also be represented as the variation of magnitude versus the colour index of stars, usually called the observational H-R diagram or the colour-magnitude diagram (CMD).

Hertzsprung and Russell showed that the distribution of stars in these plots is not random, rather they appear to fall into distinct groups. Majority of the stars are found to lie along the main sequence (MS), which spans over a wide range of temperatures from 3000 K to 40000 K. As shown in Fig. 1.2, the MS stretches from the luminous O type stars to cool M type stars. These stars are also known as dwarfs. Other significant groups of stars found on the H-R diagram are luminous stars that have evolved off the main sequence into giants and supergiants, and the hot and faint white dwarfs (WDs) (see Fig. 1.2). Apart from single stars a considerable fraction of stars in these cluster are present as binary systems. The binary stars are generally brighter than the MS stars and lie between single star and binary star isochrones. Stellar iscohrones represent the evolution of a population of stars that have the same age.
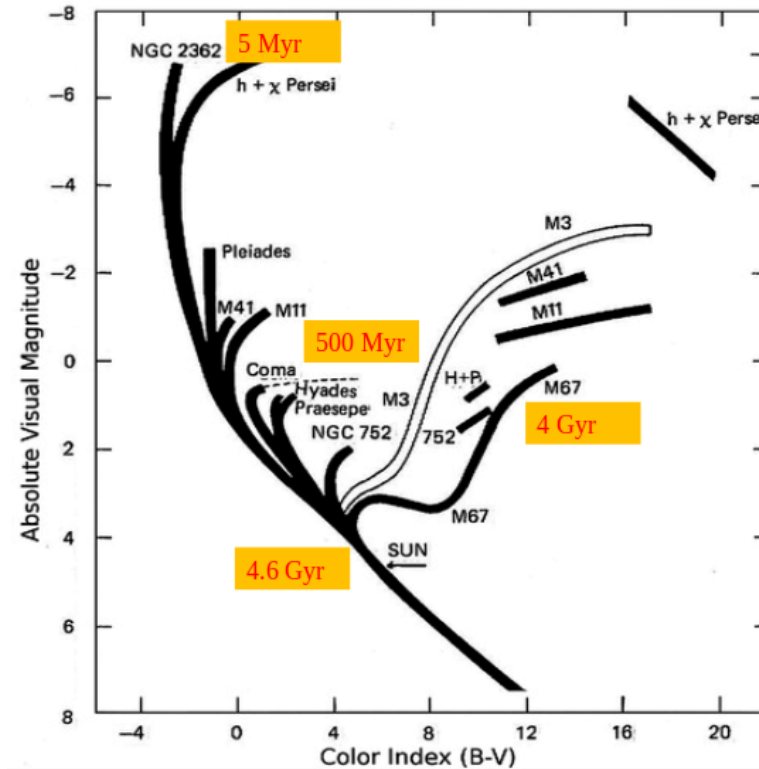
Figure 1.3: CMD of various star clusters (Sandage, 1957).

The H-R diagram or CMDs of star clusters are essential tools to discern stars in various stellar evolutionary phases. A CMD of star cluster represents the snapshot of stellar evolution at various ages. We can determine the age of a star cluster by comparing the observed CMDs of star clusters with stellar evolutionary models or isochrones. These models list the effective temperature, luminosity and mass of stars at various ages.

Massive stars in a star cluster populate the upper bluer part of the MS, followed by lower-mass stars that lie in the lower part of the MS. Massive stars evolve off the MS more rapidly than lower mass stars. In older clusters, most of the stars have evolved off the MS and lie in the giant phase. A comparison of stellar evolution in clusters of various ages is shown in Fig. 1.3.

1.3 Sun type stars

1.3.1 Structure

The internal structure of a star is dependent on its composition, age and mass. Sun serves as a fundamental benchmark to study the structure of stars. Detailed studies of Sun using helioseismology, neutrino detection, and disk-resolved imaging and spectroscopy have allowed us to map the internal structure of Sun. Like an onion model, the structure of Sun can be divided into a few layers (see Fig. 1.4): hydrogen-fusing core, a radiative interior, a convective envelope, a photosphere, and the magnetically-heated outer atmosphere.
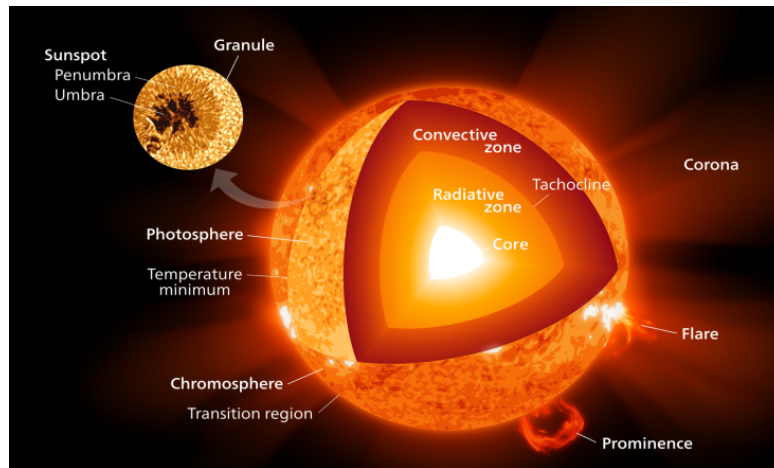
Figure 1.4: Artist impression of structure of the Sun. Image credit-Kelvinsong [CC BY-SA 3.0 (http://creativecommons.org/licenses/by-sa/3.0)

- **Hydrogen-fusing core:** It is the hottest region of the Sun where hydrogen is burnt to form helium via nuclear fusion. These reactions are highly sensitive to the temperature and density of the gas. The temperature at the center of the Sun is about 15,000,000 ° C (27,000,000 ° F) and the density is about 150 g/cm^3 (Carroll & Ostlie, 2007). The temperature and density of the Sun decrease as we move away from the central region of the Sun. At the outer edge of the core, nuclear burning is completely shut off, the temperature drops to half of it's central value and density decreases to 20 g/cm^3.

- **Radiative interior:** In this region, the energy generated in the core is carried by photons that bounce from particle to particle (radiative scattering). As we go from the outer edge of the core to the outer edge of the radiative

4

zone, the density drops from 20 g/cm^3 down to 0.2 g/cm^3, and the temperature falls from 7,000,000 ° C to about 2,000,000 ° C. This region rotates like a solid-body.

- **Tachocline:** The tachocline region lies at the interface of the radiative interior and convective envelope. In this layer, the solid-body rotation of the radiative zone and the differential rotation of material in the convective zone converge, creating shear and turbulent mixing that stretches the magnetic field lines and powers the magnetic dynamo.

- **Convection zone:** The convection zone is the outermost layer of the solar interior. Convection is responsible for carrying the energy from the tachocline region to the photosphere of the Sun. The rapid rise in material or convective motions appear as granulation on the outer layer of the Sun or solar photosphere.

- **Photosphere:** The layer of the Sun that we can directly observe is known as the photosphere. The effective temperature of the photosphere is sim 6500 K. Most of the photosphere is covered by granulation. The differential rotation of Sun leads to the concentration of magnetic fields at few places on the surface of the Sun, which inhibits convection and forms starspots of cooler material.

- **Chromosphere:** According to stellar structure theory, the temperature of the Sun should keep decreasing in the outer atmosphere, but we observe a temperature inversion in this layer. Excess UV emission is an indicator of chromospheric activity. Magnetic activity is the primary source of heating and the chromosphere cools through radiation which we observe as prominent Ca II H & K lines between 3900 and 4000 Åand the Mg II h & k lines in the UV spectrum.

- **Transition region:** The transition region is a narrow region in between the chromosphere and the corona where the temperature rises abruptly from about 8000 to about 500,000° C.

- **Corona:** The corona is the outermost region of the solar atmosphere. It's temperature is around a few million K and emits X-rays. The X-ray emission from the solar corona is an indicator of magnetic activity and heating in solar-type stars.

- **Solar wind and magnetic braking:** Sun type stars lose mass through solar winds driven by magnetic activity. Though these plasma outflows or solar winds do not affect the structure of Sun, the magnetic field lines present on the Sun generate torque against these solar winds that removes angular momentum from the Sun. This phenomenon is known as magnetic braking, which causes stars to spin down over billions of years as shown in Fig. 1.5 (Guinan & Engle, 2009).
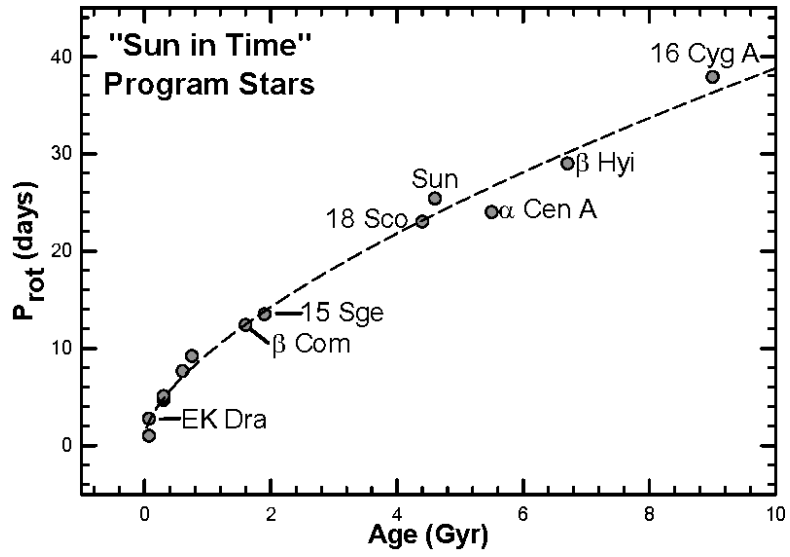
Figure 1.5: Increase in rotation period of stars due to spin-down with age that arises from the loss of angular momentum loss via magnetic breaking (Guinan & Engle, 2009).
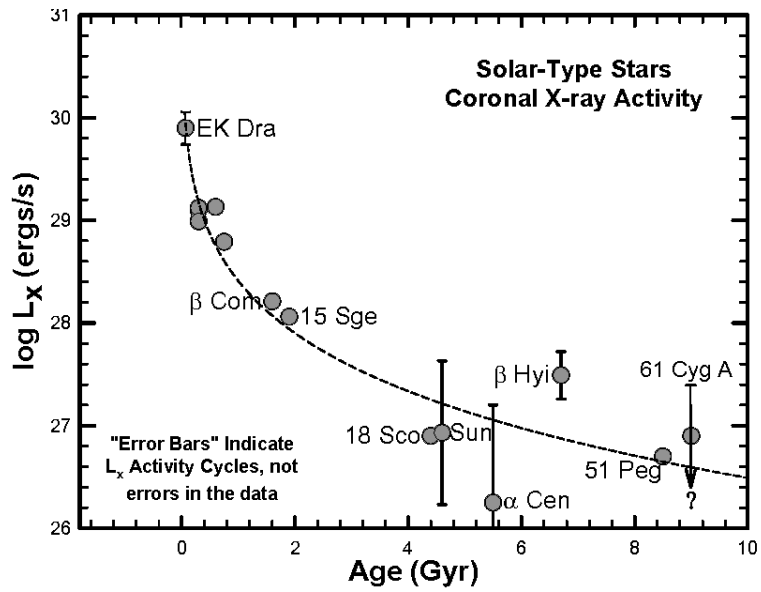
Figure 1.6: X-ray luminosity (Lx) for solar-type stars as a function of age (Guinan & Engle, 2009).

1.3.2   Stellar Evolution

Stars in clusters are formed from the collapse of giant molecular clouds, which fragment to form protostars. Protostars are cool and faint stars that are fully convective in nature. The collapse of a protostar continues until it reaches hydrostatic equilibrium. At this stage, the core temperature of the protostar is high enough to begin hydrogen fusion, and it reaches the MS phase. The time required to reach the MS phase is very small as compared to the lifetime of a star on the MS. A sun type star will stay on the MS for a period of about 10 Gyr. The newly formed stars have high rotation periods ranging from 1 to 10 days. The interaction of rapid rotation with convection leads to high magnetic activity in these young stars, that manifests as starspots on the surface of the sun, excess UV emission and high X-ray luminosity. The active phase in young stars lasts for a period of $\sim$1 Gyr, i.e. as stars age, their X-ray luminosity decreases with time, as shown in Fig. 1.6.

The MS phase comes to an end when hydrogen in the core of the star is exhausted. At the end of the MS phase, hydrostatic equilibrium is disrupted, the gravitational pressure exceeds the internal pressure, and the core starts contracting, leading to a rise in central pressure and temperature. The rise in temperature initiates fusion in the hydrogen shell surrounding the helium core, which increases the luminosity and radius of the star. In the H-R diagram, the star evolves off the MS phase and moves towards the red-giant phase. In the red giant phase, the core temperature rises high enough to start burning helium. The helium-burning leads to a sudden expansion, followed by an explosion known as the helium flash and the star moves towards the asymptotic giant branch (AGB) phase. In the AGB phase, when the central helium supply is exhausted, helium will continue to burn in a shell outside the core, while the hydrogen-burning shell is extinguished. When the helium shell ignition reaches the outer extinguished hydrogen burning layer, the AGB star enters the thermally pulsating phase. During this phase the star is quite unstable, leading to high mass-loss, and shedding of the outer envelope. The outer layers of the AGB star form a circumstellar nebula that is driven outwards by stellar winds. When the nuclear fuel in the core is exhausted, only a hot core is left behind. The hot central core is known as white dwarf (WD), that has a temperature of around 100,000 K. It cools down over the next billion years.

1.4   Aim of the present study

A multi-wavelength study of stars in a cluster allows us to study various stellar properties, such as chromospheric and coronal activity, rotation rate, binarity, etc, for a coeval population of stars. The comparison of stars in clusters of different ages provides information on the evolution of these clusters over time.

X-ray emission from stars in young OCs is primarily from coronal activity driven by stellar rotation, magnetic field and convection. As clusters age, the X-ray luminosity of stars decreases as a result of spin down due to magnetic braking (Pallavicini, 1989; Radich, 1997). Thus study of X-rays from stars in old OCs re-

veals populations of stars spun-up in binary systems, or from systems undergoing accretion. X-ray observations of intermediate age open clusters are especially important for studying both MS coronally active stars and rare interacting binaries. For example, previous X-ray studies of intermediate-age/old open clusters (NGC 6791 ~8 Gyr, van den Berg, et al. 2013; M67 ~3 Gyr, Mooley & Singh 2015; NGC 6940 Belloni & Tagliaferri 1997; NGC6633 and IC4756 ~0.7 Gyr, Briggs, et al. 2000) revealed a significant number of magnetically active - RS CVn, BY Dra, W UMa, FK Comae, Algol, and sub-subgiant (SSG) types of stars and mass transfer systems - Cataclysmic Variables (CVs), Low/High Mass X-ray Binaries (L/HMXB).

UV emission from stars in open clusters, on the other hand, is dominated by luminous hot stars and/or a hidden WD in them forming a binary system as a WD is less prominent in the optical bands wherein a late-type MS or an RGB star dominates. Recent UV studies of OCs (Siegel, et al., 2014; Sindhu, et al., 2018; Siegel, et al., 2019) have shown that UV CMDs are essential tools for identifying and studying the properties of UV bright stellar population such as spatially unresolved MS stars with cool WD companions, post-interaction binaries with hot WD companions, MS and RGB stars with high chromospheric activity, and blue straggler stars (BSS). Though, there have been extensive studies of OCs in the optical and X-ray passbands, detailed studies in UV passbands have been rare, exceptions being old open clusters (M67 Sindhu, et al. 2018; NGC 188 Gosnell, et al. 2014). Another effort in this direction has been the Swift/UVOT Stars Survey (Siegel, et al., 2019) which led to a point-source photometry catalogue for 103 Galactic OC with isochrones fitted to the UV CMDs of stars.

Here, we present the first comprehensive study of UV and X-ray emission from an intermediate-age open cluster, NGC 2527. We also study the evolution of X-ray emission from binary stars over time. The following work has recently been published in a paper by Shah, Singh & Subramaniam (2020).

1.5   Outline of the present study

The thesis is structured as follows: Introduction to NGC 2527 is given in Section 2.1, the XMM-Newton: EPIC and OM, Swift UVOT, and Gaia observations are described in Section 2.2. In section 2.3 we describe reduction of XMM EPIC and OM data, finding of optical counterparts to X-ray and UV sources, analysis of optical and UV CMDs of cluster members, determinaton of X-ray luminosity of stars by using spectral fit parameters of one bright member, and analysis of Spectral Energy Distribution (SED) of X-ray and UV sources. In section 2.4 and 2.5 we present the results and discussion respectively, and summarise the results in section 2.6.

Chapter 2

Discovery of active stars in NGC 2527

2.1 Introduction to NGC 2527

NGC 2527 is one of the nearest open cluster that lies in the southern hemisphere in the Puppis constellation. It is located at $\alpha = 08^h\ 04^m\ 58.0^s$ and δ = -28° 08' 48" (Wu, et al., 2009), at a distance of $\approx$ 600 pc and has a reddening of E(B-V) = 0.038 to 0.1 mag (Dias, et al., 2002; Lindoff, 1973). Previous studies by Lindoff (1973); Dodd, et al. (1977); Cantat-Gaudin, et al. (2018a) give an estimate of the age of the cluster to lie between 450 Myr to 1.1 Gyr. The cluster turn-off mass is about 2.8 $M_\odot$ (Reddy, et al., 2013). Recently, Cantat-Gaudin, et al. (2018b) have determined membership probability of stars using accurate Gaia astrometric measurement. The overall metallicity in the cluster is slightly lower than the solar metallicity with [Fe/H] = -0.10 (Reddy, et al., 2013). The mean radial velocity is 42.4 $\pm$ 1.3 km/s (Conrad, et al., 2014). The apparent diameter of NGC 2527 is 16' (Lindoff, 1973).

2.2 Observations

2.2.1 XMM-Newton

The XMM-Newton satellite (Jansen, et al., 2001) carries 3 X-ray telescopes, that simultaneously observe the same region of the sky. X-ray photons collected by these telescopes form images on the European Photon Imaging Camera (EPIC), that consists of the PN (Strüder, et al., 2001) and the twin MOS1 and MOS2 (Turner, et al., 2001) CCD-like arrays. The Optical Monitor (OM; Mason, et al., 2001) is a 30-cm optical/UV telescope co-aligned with the X-ray telescope that provides simultaneous coverage in optical and UV (1800 Å- 6000 Å). The OM detector has a micro-channel plate (MCP) intensified CCD array that consists of a wheel of three optical and three UV filters: V, B, U, UVW1, UVM2, and UVW2, with effective wavelengths of 5430 Å, 4500 Å, 3440 Å, 2910 Å, 2310 Å, and 2120 Å, respectively. The X-ray detectors cover a field of view of radius 15', whereas the OM detector covers the central part of X-ray cameras with a field of view (fov)
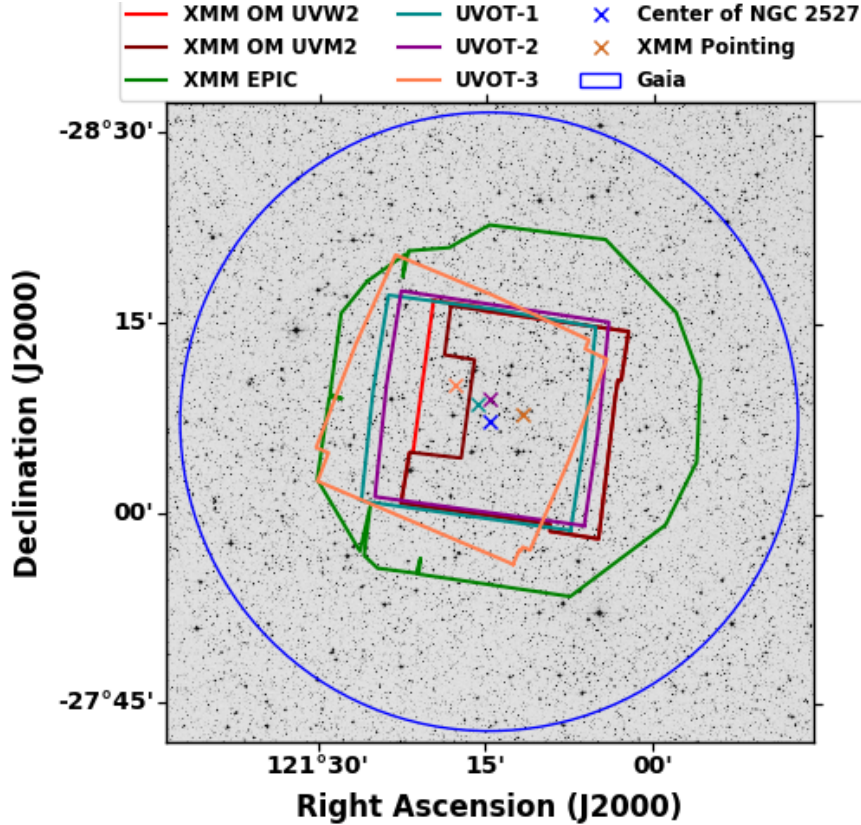
Figure 2.1: Digitized Sky Survey (DSS) image of NGC 2527. The footprints of XMM EPIC (PN, MOS1 and MOS2), and OM (UVW2 and UVW1) and Swift UVOT observations are overplotted over the image. A circle of radius 25' is also shown to indicate the region containing half the cluster members (Cantat-Gaudin, et al., 2018b). The crosses indicate the pointing direction and thus its offset from the center of NGC 2527.

of about $17' \times 17'$.

We have analysed data from the XMM-Newton (Jansen, et al., 2001) observations (ObsId = 0057570101) of NGC 2527 centered on $\alpha = 08^h04^m47.20^s$, $\delta = -28°$ 07' 52.0" performed on March 18, 2002, and March 19, 2002 during orbit 432. During these observations, the PN camera (Strüder, et al., 2001) was active in extended full frame mode, and the MOS cameras (Turner, et al., 2001) were active in the full frame mode, using the medium filter. We have analysed only the deepest XMM-Newton EPIC (PN, MOS1, and MOS2) exposures of NGC 2527. Several simultaneous short exposure OM (Mason, et al., 2001) observations in imaging mode with UVM2 (2310 Å) and UVW2 (2120 Å) filters were also used. In the OM observations with UVM2 filter, one of the mosaic windows needed to cover the full field of view was not taken. The observation log of XMM-Newton observations is given in Table 2.1. The footprints of EPIC (PN and MOS) and OM (UVM2 and UVW2) XMM-Newton observations of NGC 2527 are overplotted on the Digitized Sky Survey (DSS) image of NGC 2527 in Figure 2.1. The details of EPIC and OM data processing and analysis are given in Section 2.3.1.

Table 2.1: Log of XMM-Newton observations of NGC 2527 analysed in this study.

INSTRUMENT (MODE)	FILTER	EXPOSURE TIME (FILTERED) (sec)
EPN (Extended Full Frame)	MEDIUM	45998 (26600)
EMOS1 (Full Frame)	MEDIUM	33283 (25300)
EMOS2 (Full Frame)	MEDIUM	33265 (25600)
OM (Image)	UVM2	4×4300
OM (Image)	UVW2	5×4400

2.2.2 Swift UVOT

UVOT is a modified Richey-Chretien 30 cm telescope aboard the Swift Gamma-Ray Burst mission (Gehrels, et al., 2004). Just like XMM-OM, UVOT has a wide fov of 17' × 17', a microchannel plate intensified CCD operating in photon counting mode and a filter wheel that includes a clear white filter, u, b and v optical filters, UVW1, UVM2 and UVW2 ultraviolet filters, a magnifier, two grisms, and a blocked filter (Roming, et al., 2004). A 2.3" resolution and wide coverage of UVOT in the NUV band with three filters - UVW1, UVM2, and UVW2 (effective wavelengths of 2600 Å, 2246 Å, and 1928 Å, respectively) make it an ideal instrument to study the hot stellar population in OCs.

We obtained the Swift UVOT photometric data of NGC 2527 from Siegel, et al. (2019). These data had been processed using the reduction pipeline outlined in Siegel, et al. (2014). The footprints of multiple UVOT observations in UVW2 (1928 Å), UVM2 (2246 Å), and UVW1 (2600 Å) filters are overplotted on the DSS image of NGC 2527 (see Figure 2.1). Bright sources with high count rates that lead to significant coincidence losses were not included in the Swift UVOT catalogue. We converted the UVOT magnitudes to count rates using the eqn. 2.1 (Poole, et al., 2008).

$$C_{source} = 10^{\frac{Z_{pt}-m}{2.5}} \tag{2.1}$$

where m and C_{source} is the magnitude and count rate of a source in the UVOT filters, and Z_{pt} is the zero point for each UVOT filter obtained from Breeveld, et al. (2011). The flux in each UVOT filter was calculated by converting the estimated count rates to fluxes using the conversion factors for Vega magnitude scale. The conversion factors were obtained from Brown, et al. (2016). The magnitudes and extinction corrected fluxes of cluster members in UVW1, UVW2 and UVM2 filters are given in online-only Table A.

2.2.3 Gaia

The Gaia satellite (Gaia Collaboration, et al., 2016) carries two identical telescope that are separated by a 106.5° angle. The light from these telescopes is merged into a common path and falls upon three instruments: astrometric, photometric and radial velocity spectrometer. The astrometric instrument measures the stellar positions, parallax and distance of stars, and proper motion velocity of stars on the sky. The photometric instrument estimates the colour of the stars from low-resolution spectra in blue and red range of the optical spectrum. The Radial

Velocity Spectrometer estimates the radial velocity i.e. the velocity along the line of sight of the star by measuring the Doppler shift of absorption lines in a high-resolution spectrum covering a narrow wavelength range.

Gaia Data Release 2 (DR2) offers a precise and accurate 5-parameter astrometric solution i.e. positions (α and δ), proper motions in right ascension (μ_α) and declination (μ_δ), and parallaxes (ϖ), magnitudes in three photometric filters (G, G_{BP}, and G_{RP}) for more than 1.3 billion sources and radial velocities (RV) for more than 7 million stars (Gaia Collaboration, et al., 2018). Cantat-Gaudin, et al. (2018b) used precise and accurate astrometric (proper motion and parallax) measurements from Gaia DR2 catalogue to determine the cluster membership probability of stars for 1229 OCs in the Milky Way. They have excluded sources fainter than G = 18 mag because of high uncertainties in parallax and proper motion values for such sources. NGC 2527 is part of the Gaia DR2 open cluster population in Milky Way Catalogue (Cantat-Gaudin, et al., 2018b). The catalogue gives membership probabilites of 400 potential members stars that lie around the center of NGC 2527. Out of these 400 stars, only 356 stars have membership probability > 50% that are considered as highly probable members of NGC 2527. As per Cantat-Gaudin, et al. (2018b), half of the cluster members are present within a a circle of radius $\approx 25'$ from the cluster centre as shown on the DSS image of NGC 2527 in Figure 2.1. The Gaia DR2 catalogue gives radial velocity of 43 bright highly probable members of NGC 2527. The mean radial velocity of these stars is 41 ± 9 km/s. It is consistent with the previous estimates of radial velocity (42.4 ± 1.3) by RAVE survey of OCs (Conrad, et al., 2014).

2.3 Data Analysis

2.3.1 X-ray Data Reduction

Raw data obtained from the XMM-Newton Science Archive were processed using the XMM-Newton Science Analysis Software (SAS 17.0.0). SAS tasks 'emchain' and 'epchain' were used to generate event files for the MOS and PN detectors, respectively. These tasks perform energy and astrometry calibration of events registered on each CCD chip and combine them into a single data file. The event lists of both MOS and PN were filtered using SAS task 'evselect' in the 0.3-7.0 keV energy band and only the single, double, triple, and quadruple pixel events were retained as genuine X-ray events. This removes the contamination due to low pulse height events. Furthermore, the data from all three cameras were individually screened for soft proton background flaring, by applying the criterion of total count rate for single events with energy > 10 keV that exceeded 0.4 counts s^{-1} and 1.0 counts s^{-1} for the MOS and PN detectors respectively. The time intervals affected by soft proton flares were thus excluded from the analysis. The observation log and useful exposure time for XMM-Newton observations are summarised in Table 2.1.
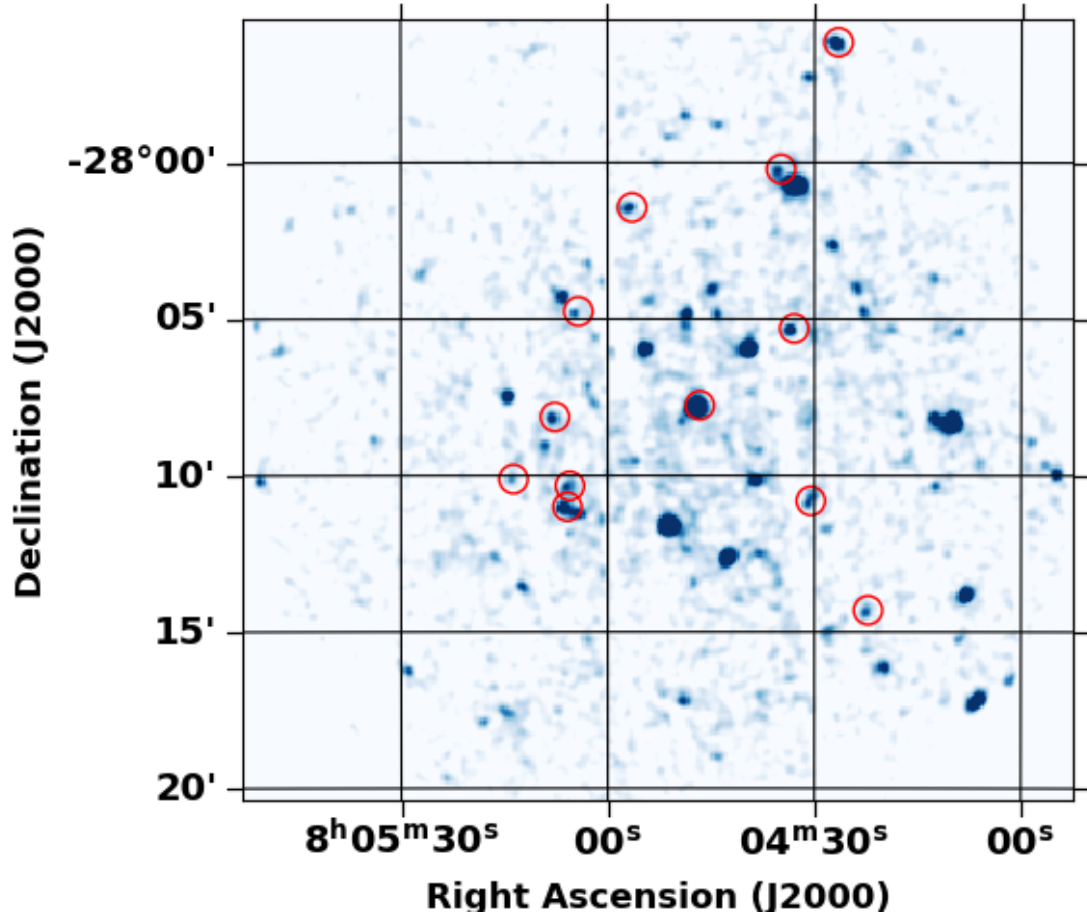
Figure 2.2: Mosaic of PN and MOS soft band (0.3-2.0 keV) X-ray image of NGC2527 smoothed with a 2D Gaussian $\sigma = 2$ pixel. The circles indicate the position of the soft band X-ray sources which are members of NGC 2527 and have distinct optical counterparts.
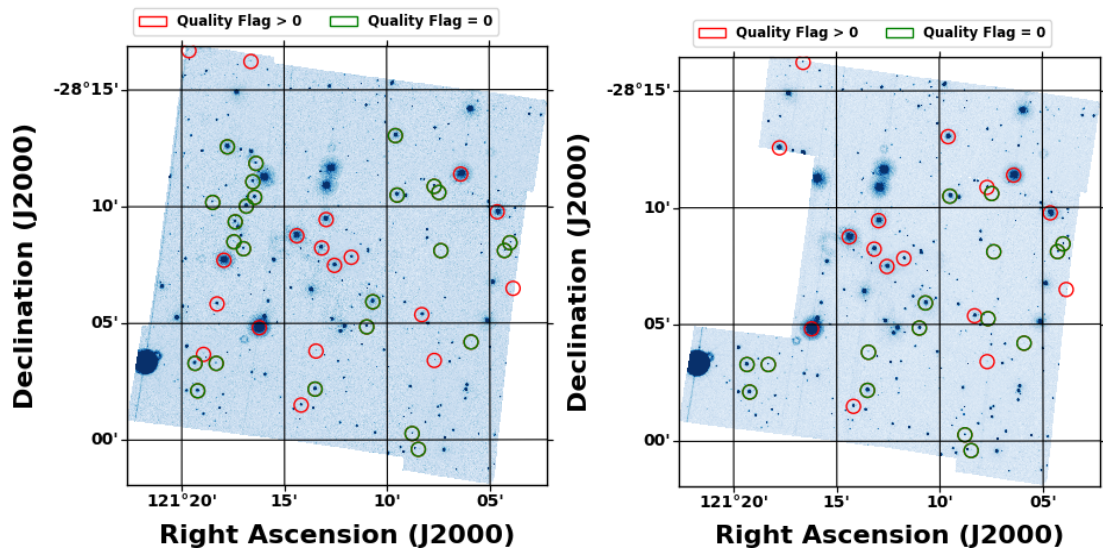
Figure 2.3: Mosaic of all the OM exposures in UVW2 filter (left) and UVM2 filter (right). The green circles represent the detected sources in each filter which are members of NGC 2527 and have distinct optical counterparts.

13

2.3.2 X-ray Images and Source Detection

We produced images in two energy bands, a soft band (0.3-2.0 keV), and a hard band (2.0-7.0 keV) for all three EPIC detectors using the 'evselect' and 'emosaic' SAS tasks with the filtered MOS and PN event lists. During the imaging process, only the events with FLAG = 0, PATTERN$\leq$4 (single and double pixel events) in the hard band and PATTERN == 0 (single pixel events) in the soft band were selected. These events were selected to reject noise at the extremities of the PN detector along Y-direction. Default image binning of 600×600 pixels was chosen, similar to the one used in the 3XMM catalogue.

We used the SAS task 'edetect_chain' to search for sources present in both the soft and hard bands in the XMM-Newton EPIC (PN, MOS1 and MOS2). The 'edetect_chain' task is a script which runs a series of subtasks to detect point sources from the input filtered event files. It determines the source parameters such as coordinates, count, count rates, etc through simultaneous maximum likelihood PSF (point spread function) fitting to the source count distribution in the given energy bands of each EPIC instrument. A combined Maximum Likelihood (ML) value for all three instruments was taken to be greater than 10. We detect 64 sources in the soft band and 34 sources in the hard band. The merged PN and MOS soft band X-ray image of NGC 2527 smoothed with a 2D Gaussian $\sigma = 2$ pixel is shown in Figure 2.2.

2.3.3 OM Data Reduction

The OM observations taken in Imaging mode were processed using the SAS task 'omichain' with default parameters. This task is a script which detects sources in the OM image and performs aperture photometry on the detected sources. It processes the data from multiple exposures simultaneously and returns various data products. We obtained images and source lists for individual exposures in each filter, mosaiced images, and merged source list from all the observations. The merged source list contains information of source position, count rates, fluxes, magnitudes, and quality flags. The SAS pipeline corrects the count rates and fluxes for coincidence losses, dead time and time dependent sensivity of the detector. The combined multiple exposures of OM images in UVW2 and UVM2 filters is shown in Figure 2.3. A total of 729 sources were thus detected in the merged OM catalogue. The extinction corrected fluxes and the quality flags of cluster members detected in OM are given in online-only Table A. The SAS pipeline provides a quality flag for each OM source. The sources with quality flag equal to zero are good detections. SAS task detects a significant number of sources which have quality flag > 0 that lie on a readout streak, a bad pixel, near a bright source, near the edge or on a star-spike which are spurious detections and sources with high count rates (rate ¿ 0.97 c/frame). Out of the 729 sources, only 316 detected in UVW2 filter and 217 sources in UVM2 are good detections and not artefacts. The OM sources with bad quality flags were excluded from the subsequent analysis for Spectral Energy Distributions.

Table 2.2: Summary of total number of sources, and cluster members observed in Gaia, XMM and Swift fov of NGC 2527.

Energy Band	No. of observed sources	No. of cluster members
Gaia Optical	400	358
OM UVM2	600	32
OM UVW2	426	43
UVOT UVW1	1292	51
UVOT UVM2	1025	51
UVOT UVW2	1279	51
X-ray soft band	64	12
X-ray hard band	34	0

2.3.4   Optical Counterparts

In order to determine the nature of sources detected in Swift UVOT and XMM observations, we searched for their optical counterparts in the Gaia members catalogue of NGC 2527.

We determined the optimum cross-correlation separation between soft band X-ray catalogue and optical counterparts using the method outlined by Jeffries, et al. (1997). We find that the best cross-correlation radius of 3" optimizes the number of real identifications while minimizing the number of spurious detections due to background sources. The details of the best fit cross-correlation function is given in Appendix A. Within a radius of 3", 12 soft band X-ray sources possess a unique optical counterpart that is a cluster member. None of the hard band X-ray sources has an optical counterpart that is a cluster member within a radius of $\leq$ 30" from the hard band X-ray source position, suggesting that the sources in the hard X-ray band are not members of the cluster. X-ray sources that have a unique optical counterpart that is a proper motion member of the cluster have been considered as real sources, and other sources are considered as spurious detections. To identify optical counterparts to the UV (OM/UVOT) sources, we assumed a cross-correlation radius of 3". Within a 3" radius, we find that 44 XMM-OM, and 54 UVOT sources have unique optical counterparts (see Table 2.2).

The total Galactic column density along the line of sight of NGC 2527, but extending to the edge of the Galaxy as given by the (HI4PI Collaboration, et al. 2016; see HEASARC N_H column density tool[1]) is $N_H = 44.2 \times 10^{20}$ cm^{-2}. To estimate the number of extragalactic sources in the field of view (fov) of XMM-Newton, we assumed a power-law model with a photon index $\Gamma = 2$, and the quoted value of N_H. An upper limit on the background count rate in the hard band for EPIC MOS1 observations was found to be ~ 0.002 counts/s (see also Sect. 3.6). Since the log N − log S distribution derived from the ROSAT deep sky survey (Hasinger, et al., 1993) gives flux in the $0.5 - 2.0$ keV energy band, we determined the total flux for the power-law model in this energy band using the HEASARC WebSpec[2] tool. For a count rate of $\sim$0.002 counts/s, exposure time of 25300 sec, the $\Gamma = 2$ power law with $N_H = 44.2 \times 10^{20}$ cm^{-2} and normalization $= 1.63 \times 10^{-5}$

---

[1]https://heasarc.gsfc.nasa.gov/cgi-bin/Tools/w3nh/w3nh.pl
[2]https://heasarc.gsfc.nasa.gov/webspec/webspec.html

has a flux of 1.3×10^{-14} ergs cm^{-2} s^{-1} and 3.1×10^{-14} ergs cm^{-2} s^{-1} in 0.5-2.0 keV and 2.0-7.0 keV energy band respectively. A comparison of the background flux in the 0.5-2.0 keV energy band with the log N $-$ log S distribution suggests that approximately 30-35 extragalactic sources are likely to be detected above a maximum likelihood threshold of 10. The number of hard band X-ray sources detected in our XMM-Newton observations is consistent with the estimated number of background sources.

X-ray properties of cluster members are given in Table 2.3. Positions of X-ray, OM - UVW2, and UVW1 sources which have unique optical counterparts that are cluster members are shown in Figure 2.2 and Figure 2.3. In the OM images, sources with good and poor quality flags are marked with green and red colours respectively to distinguish between good and bad quality detection. A unique object id SwiftXMMOM (SXOM) has been assigned to the cluster members that are detected in the XMM and Swift UVOT observations. Sources that have been detected only in the XMM-OM and not in the Swift UVOT observations are considered as spurious detections. SXOM30 and SXOM46 are two such sources which were excluded from further analysis.

Figure 2.4: Optical CMD of NGC 2527 based on Gaia magnitudes. The best fitting PARSEC isochrone along with an equal mass binary isochrone are overlaid on the observed CMD.

2.3.5   Optical and UV Color Magnitude Diagram

The Hertzsprung-Russell (H-R) Diagram or the Color-Magnitude Diagram (CMD) of OCs can be used to distinguish between stars in various stellar evolutionary stages and identify peculiar stars that deviate from standard evolutionary models. These are essential tools to determine the fundamental properties of a cluster like age and extinction. These parameters can be determined by fitting standard

Table 2.3: Properties of cluster members detected in the XMM observations. The superscript $^\alpha$ on the source ID denotes that the corresponding X-ray properties are from the PN detector as the source lies outside the MOS CCD. Column 1 gives the ID of stars detected in X-ray or UV, Columns 2, 3, 4, 5 & 8 list the RA, Dec, distance, radial velocity from Gaia DR2, and membership probability of stars obtained from Cantat-Gaudin, et al. (2018b), columns 6 & 7, give the G mag and the G_{BP}-G_{RP} colour taken from Gaia DR2 catalogue, columns 9, 10 & 11 give the countrate, flux and X-ray luminosity of sources that lie in the field of view of XMM detector, and column 12 gives the type of stars depending upon their position in the optical CMD.

SXOM	RA (^{h} $'$ $''$)	Dec ($^\circ$ $'$ $''$)	Distance (pc)	Radial Velocity (km/s)	G (mag)	G_{BP}-G_{RP} (mag)	PMemb	Rate (10^{-3} counts s^{-1})	F_X (10^{-15} ergs s^{-1} cm^{-2})	L_X (10^{29} ergs s^{-1})	Type
1	8:05:27.17	-28:17:33.29	645.0±18.6	-	11.31	0.52	1.0	<1.867	<3.22	<1.6	B[1]
2	8:05:33.73	-28:12:43.42	623.8±13.5	-	12.6	0.65	1.0	<1.867	<3.22	<1.5	MS[2]
3	8:05:35.17	-28:13:12.38	656.4±15.9	41.77±2.28	12.17	0.58	1.0	<1.867	<3.22	<1.66	MS
4	8:05:18.65	-28:16:41.64	639.9±9.2	-	13.87	0.88	1.0	<1.867	<3.22	<1.58	MS
5	8:05:16.3	-28:16:52.21	617.7±14.5	-	11.52	0.43	1.0	<1.867	<3.22	<1.47	MS
6	8:05:36.06	-28:16:53.53	670.3±16.2	-	10.77	0.31	1.0	<1.867	<3.22	<1.73	MS
7	8:04:30.86	-28:10:52.97	642.6±11.8	33.52±13.54	12.86	0.69	1.0	1.44±0.4	2.49	1.23	MS
8	8:04:29.89	-28:10:35.99	635.8±8.0	-	13.67	1.0	1.0	<1.867	<3.22	<1.56	B
9	8:04:38.37	-28:13:02.64	629.4±14.6	-	11.29	0.39	1.0	<1.867	<3.22	<1.52	MS
10	8:04:54.64	-28:18:08.26	628.3±7.0	-	13.07	0.76	1.0	<1.867	<3.22	<1.52	MS
11	8:05:06.52	-28:16:13.63	634.1±8.4	-	13.9	0.87	1.0	<1.867	<3.22	<1.55	MS
12	8:04:32.53	-28:12:02.0	631.1±12.4	-	15.32	1.26	1.0	<1.867	<3.22	<1.53	MS
13	8:04:15.48	-28:06:29.1	637.0±9.7	-	14.19	0.94	1.0	<1.867	<3.22	<1.56	MS
14	8:04:38.09	-28:10:30.78	638.2±15.0	-	11.43	0.46	1.0	<1.867	<3.22	<1.57	PB[3]
15	8:04:29.57	-28:08:06.18	633.6±9.6	-	14.39	0.99	1.0	<1.867	<3.22	<1.54	MS
16	8:04:16.1	-28:08:26.46	636.5±7.3	-	13.26	0.9	1.0	<1.867	<3.22	<1.56	B
17	8:04:35.46	-28:10:42.69	608.5±28.7	-	16.35	1.87	1.0	<1.867	<3.22	<1.43	B
18	8:04:18.54	-28:09:46.17	661.4±17.8	-	10.8	0.27	1.0	<1.867	<3.22	<1.68	MS
19	8:04:25.65	-28:11:23.72	674.0±16.4	-	10.11	0.23	1.0	<1.867	<3.22	<1.75	MS
20	8:04:17.16	-28:08:06.61	631.0±10.0	-	12.97	0.82	1.0	<1.867	<3.22	<1.53	B
21	8:04:44.06	-28:04:52.13	630.7±12.4	-	12.34	0.6	1.0	<1.867	<3.22	<1.53	MS
22	8:05:05.56	-28:11:51.47	633.1±13.7	-	12.9	0.7	1.0	<1.867	<3.22	<1.54	MS
23	8:04:35.19	-28:00:16.71	567.0±11.8	-	13.31	0.95	0.9	1.65±0.49	2.85	1.1	B
24	8:05:47.42	-28:05:53.4	661.8±15.0	32.23±5.74	12.54	0.71	1.0	<1.867	<3.22	<1.69	PB
25	8:05:48.68	-28:07:07.07	626.2±8.7	-	14.14	0.94	1.0	<1.867	<3.22	<1.51	MS
26	8:05:17.44	-28:03:17.37	621.0±13.2	38.28±0.87	11.93	0.54	1.0	<1.867	<3.22	<1.48	MS
27	8:05:29.77	-28:09:03.37	601.0±36.4	-	11.09	0.35	0.5	<1.867	<3.22	<1.39	PB
28	8:05:04.97	-28:04:50.36	678.0±23.5	-	9.46	0.23	1.0	<1.867	<3.22	<1.77	MS
29	8:05:09.61	-28:09:21.13	626.7±11.7	-	11.95	0.52	1.0	<1.867	<3.22	<1.51	MS
30	8:04:23.71	-28:04:11.78	628.2±9.4	-	14.39	0.99	1.0	<1.867	<3.22	<1.52	MS
31	8:05:05.82	-28:10:24.09	618.7±12.0	42.66±6.36	11.69	0.6	0.8	1.72±0.43	2.98	1.36	B
32	8:04:57.65	-28:08:46.31	652.8±16.1	-	10.09	0.32	1.0	<1.867	<3.22	<1.64	B
33	8:05:06.18	-28:11:4.33	612.7±11.6	-	11.79	0.63	1.0	3.74±0.6	6.47	2.91	B
34	8:04:56.79	-28:01:30.34	715.0±17.3	43.32±2.86	12.34	0.71	1.0	2.83±0.55	4.9	2.99	B
35	8:05:13.13	-28:05:50.23	630.7±14.2	40.67±1.46	12.09	0.58	1.0	<1.867	<3.22	<1.53	MS
36	8:05:11.14	-28:12:34.01	641.6±15.4	-	11.05	0.38	1.0	<1.867	<3.22	<1.58	PB
37	8:04:50.25	-28:07:29.2	653.4±12.9	-	11.76	0.49	1.0	<1.867	<3.22	<1.64	MS
38	8:05:11.83	-28:07:42.43	677.5±16.6	-	9.57	0.34	0.7	<1.867	<3.22	<1.77	MS
39	8:05:15.75	-28:03:40.07	651.2±13.0	-	14.64	1.03	1.0	<1.867	<3.22	<1.63	MS
40	8:05:07.45	-28:10:01.78	626.0±11.7	27.4±11.79	11.66	0.48	1.0	<1.867	<3.22	<1.51	MS
41	8:05:16.9	-28:02:06.61	607.8±12.9	41.26±16.89	12.07	0.57	1.0	<1.867	<3.22	<1.42	MS
42	8:05:33.91	-28:08:58.2	643.3±16.0	40.26±0.11	9.3	1.13	1.0	<1.867	<3.22	<1.59	RGB[4]
43	8:04:54.06	-28:02:11.25	654.5±15.7	41.41±3.53	11.88	0.5	1.0	<1.867	<3.22	<1.65	MS
44	8:05:05.48	-27:59:44.17	625.0±18.6	-	10.84	0.31	1.0	<1.867	<3.22	<1.5	B
45	8:05:40.68	-28:02:25.15	615.6±11.1	40.59±2.9	12.12	0.57	1.0	<1.867	<3.22	<1.46	MS
46	8:04:33.98	-27:59:36.88	633.8±19.1	-	16.15	1.51	1.0	<1.867	<3.22	<1.55	MS
47	8:04:51.94	-28:09:27.85	628.1±13.6	-	10.51	0.4	0.6	<1.867	<3.22	<1.52	SSG[5]
48	8:04:33.28	-28:05:22.32	616.0±12.1	39.41±11.09	11.57	0.6	1.0	1.75±0.39	3.03	1.37	B
49	8:05:22.42	-28:10:18.65	637.8±16.0	-	15.65	1.34	1.0	<1.867	<3.22	<1.57	MS
50	8:05:36.6	-28:03:38.58	593.3±17.2	-	11.14	0.48	1.0	<1.867	<3.22	<1.35	B
51	8:04:42.42	-28:08:56.32	643.3±14.8	-	15.56	1.33	1.0	<1.867	<3.22	<1.59	MS
52	8:04:30.69	-28:05:14.74	623.6±11.8	-	14.62	1.04	1.0	<1.867	<3.22	<1.5	MS
53	8:05:07.99	-28:08:12.08	619.5±10.4	-	12.94	0.7	1.0	1.9±0.45	3.29	1.51	MS
54	8:04:42.86	-28:05:56.44	615.8±11.9	-	11.53	0.49	1.0	<1.867	<3.22	<1.46	PB
55	8:04:30.88	-28:03:24.34	644.9±9.8	-	14.36	0.97	1.0	<1.867	<3.22	<1.6	MS
56	8:04:54.11	-28:03:50.29	638.0±11.9	-	15.04	1.14	1.0	<1.867	<3.22	<1.57	PB
57	8:05:13.31	-28:03:17.53	614.1±8.4	-	13.68	0.84	1.0	<1.867	<3.22	<1.45	MS
58	8:05:24.96	-28:13:14.44	619.6±10.8	-	14.8	1.09	1.0	<1.867	<3.22	<1.48	MS
59	8:05:14.0	-28:10:11.19	634.8±7.2	-	13.32	0.77	1.0	1.17±0.41	2.02	0.98	MS
60	8:04:52.8	-28:08:14.82	664.5±15.0	46.43±3.2	11.42	0.43	0.9	<1.867	<3.22	<1.7	PB
61	8:04:46.96	-28:07:49.84	644.3±12.7	40.32±0.29	9.34	1.12	1.0	12.06±0.82	20.86	10.36	RGB
62	8:05:09.88	-28:08:29.82	643.1±9.9	-	13.9	0.88	1.0	<1.867	<3.22	<1.59	MS
63	8:04:22.53	-28:14:22.79	659.7±48.1	-	17.75	2.06	0.8	1.73±0.48	2.99	1.56	MS
64	8:05:04.59	-28:04:49.57	626.4±9.7	-	13.6	0.77	1.0	1.55±0.39	2.68	1.26	MS
65	8:04:26.85	-27:56:13.49	646.0±14.4	38.63±0.23	9.5	1.15	1.0	3.79±0.74	6.56	3.27	RGB

[1] B : Binary
[2] MS : Main Sequence
[3] PB : Potential Binary
[4] RGB : Red Giant Branch
[5] SSG : Sub-subgiant

17

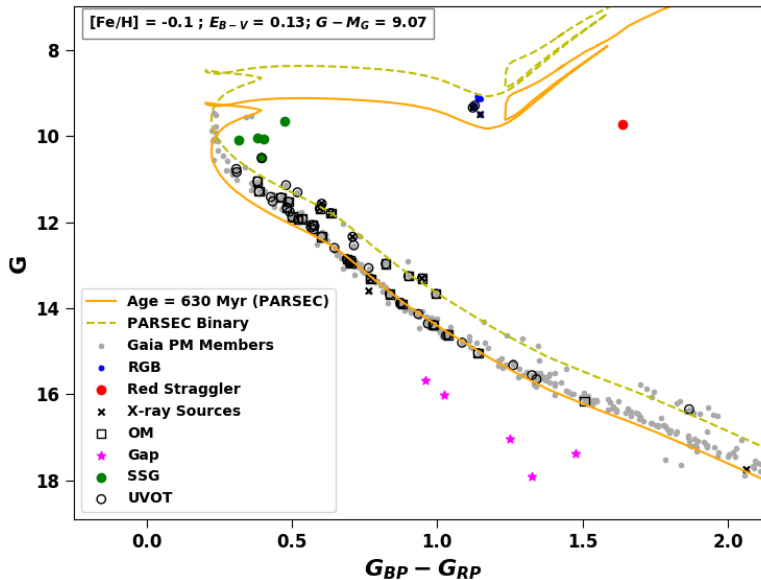stellar evolutionary tracks or isochrones to the observed CMD.

Figure 2.5: UV-optical CMD of NGC 2527 based on UVW2 magnitude. The best fitting PAR-SEC isochrone along with an equal mass binary isochrone are overlaid on the observed CMD.

The optical CMD of NGC 2527 based on the Gaia magnitudes (G, $G_{BP} - G_{RP}$) is shown in Figure 2.4. The main sequence, as well as the binary sequence, can be distinctly identified in the optical CMD. Previous ground-based optical photometric studies of NGC 2527 using CMD (Lindoff, 1973; Dodd, et al., 1977) were limited only to a few cluster members and the distance to NGC 2527 was not well known. Therefore, the fundamental parameters of NGC 2527 given in the literature have high uncertainty. The distance to NGC 2527 can now be calculated fairly accurately from the average of Gaia DR2 parallaxes of cluster members. We have corrected the Gaia DR2 parallaxes for bias by adding +0.029 mas to the parallax values as prescribed by Lindegren, et al. (2018) and inferred the mean distance to NGC 2527 to be 642 ± 30 pc, which corresponds to a distance modulus of $G - M_G = 9.0 \pm 2.4$ mag. The PARSEC-COLIBRI isochrone (Marigo, et al., 2017) of log(age) = 8.8 or 630 million years with a reddening of E(B-V) = 0.13, fixed metallicity [Fe/H] = -0.1 (Reddy, et al., 2013) and distance modulus of $G - M_G = 9.0$ mag is found to match the observed MS and main sequence turn off (MSTO) very well. The extinction coefficients used for the Gaia and UVOT filters were obtained from the VOSA Filter Profile Service (Rodrigo, et al., 2012). The PARSEC-Isochrone with these parameters along with an equal mass binary isochrone are superimposed over the observed optical Gaia CMD in Figure 2.4.

Of the 44 cluster members detected in the OM only 16 (and 25) have good quality flags in the UVM2 (in the UVW2) filter, as compared to 51 cluster members in each UVOT (UVM2, UVW2, and UVW1) filter. Since there are fewer sources in OM, it is difficult to distinctly visualize the main sequence in UV-optical CMDs with OM magnitudes. Therefore, we only use UVOT magnitudes
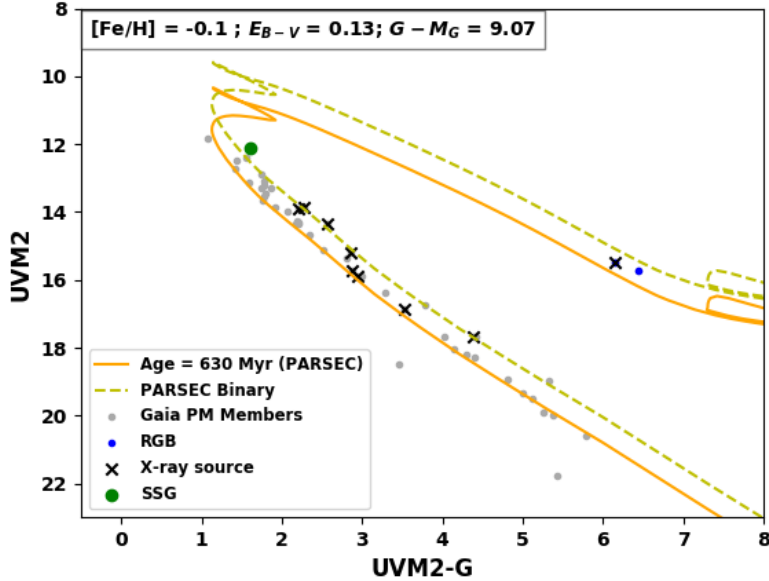
Figure 2.6: UV-optical CMD of NGC 2527 based on UVM2 magnitude. The best fitting PARSEC isochrone along with an equal mass binary isochrone are overlaid on the observed CMD.

for UV-optical CMDs. The UV-optical CMD based upon UVOT photometry in the UVW2, UVM2, and UVW1 filters is shown in Figures 2.5, 2.6 and 2.7. The PARSEC-COLIBRI isochrones with the same parameters as the optical isochrones are overlaid on UV-optical CMDs. The stars near the main sequence turn-off are not detected in the Swift UVOT because they are saturated or lie outside the fov of Swift UVOT. The PARSEC isochrones fit the MS very well in the UV-optical CMDs based on the UVW1-G and UVM2-G colours. The faint MS stars in the UVW2-G CMD have an excess blue colour as compared to the PARSEC isochrones. Siegel, et al. (2019) had also found an excess in the UVW2 - UVW1 colours of faint MS stars as compared to the isochrones.

We checked the position of each star in the Gaia optical CMD and UV-optical CMD, and have classified those which lie close to the binary isochrone as Binary (B). Similarly those lying close to the single star isochrone have been classified as Main Sequence (MS), the ones near the red giant phase of the isochrone as RGB, and the ones lying between single star and binary isochrone in the optical CMD but closer to the binary isochrone in the UV CMD as Potential Binaries (PBs) (see Table 2.3). A few stars that deviate from the standard evolutionary models are classified as red straggler (RS) or sub-subgiant (SSG) depending upon whether they lie in the RS or the SSG region. As per Geller, et al. (2017), SSG refer to stars that are fainter than the normal subgiants and redder than the normal MS star, whereas the RS stars are brighter than the normal subgiants and redder than the normal RGB. The fundamental parameters of the peculiar stars that lie outside the fov of XMM and Swift UVOT detectors are given in the appendix Table D. Below, we focus only on the stars which are detected in either XMM-OM, Swift UVOT, and XMM-EPIC observations.
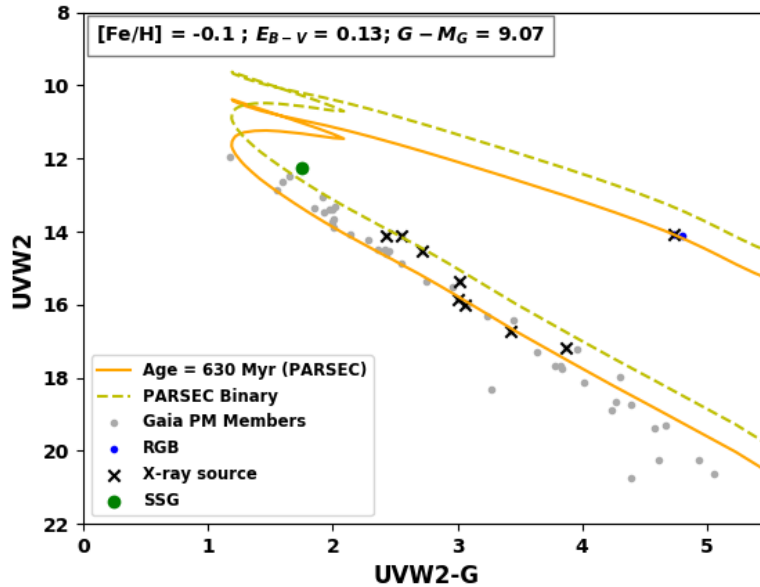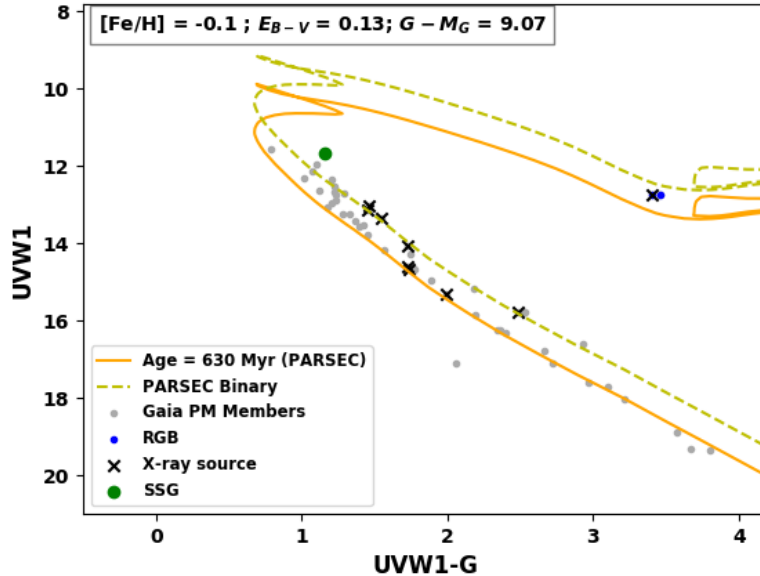
Figure 2.7: UV-optical CMD of NGC 2527 based on UVW1 magnitude. The best fitting PAR-SEC isochrone along with an equal mass binary isochrone are overlaid on the observed CMD.

Table 2.4: Results of fitting tbabs*apec model to the observed PN, MOS1 and MOS2 X-ray spectrum of SXOM61. Column density of the absorber, N_H, in the tbabs model was fixed at 8.12×10^{20} cm^{-2}. The errors quoted are with 90% confidence. Column 1 gives the common elemental abundance value used by the model, Column 2 gives the plasma temperature of the best fitting apec model, Column 3 gives the total flux in the 0.3-2.0 keV energy band, and Column 4 gives the reduced χ^2 of the fit and the degrees of freedom (dof: equal to the number of channel groups minus one).

Abundance	kT (keV)	$\log_{10}$ Flux (ergs cm^{-2} s^{-1})	χ^2_{red} (dof)
1.0 (fixed)	0.613±0.05	-13.69±0.04	1.123(39)
$0.33^{+0.34}_{-0.13}$	0.62±0.06	-13.67±0.04	1.015(38)
0.3 (fixed)	0.62 ± 0.06	-13.67 ± 0.4	0.991(39)

2.3.6 Spectral Fitting and Luminosity of X-ray Sources

A bright X-ray source SXOM61 is the only source that is found to have a significant number of counts (> 100) for spectral analysis. We extracted PN and MOS spectra for the source and background regions. The source spectrum was extracted from a circular region of radius 30" centred on the X-ray source. For the MOS, the background spectrum was extracted from an annulus with inner radius of 40" and outer radius of 60" centered on the X-ray source. For the PN, such an annular region coincided with PN chip gap, so the background spectrum was extracted from a circle with a radius of 60" close to the source position. We used the SAS task 'especget' to extract these spectra from the filtered PN and MOS event files. We grouped the spectral (PHA) channels using the 'specgroup' task such that each grouped PHA channel had at least 16 counts, sufficient for the assumption of Gaussian distribution of uncertainties. This task also performs the subtraction of the background spectrum from the source spectrum.
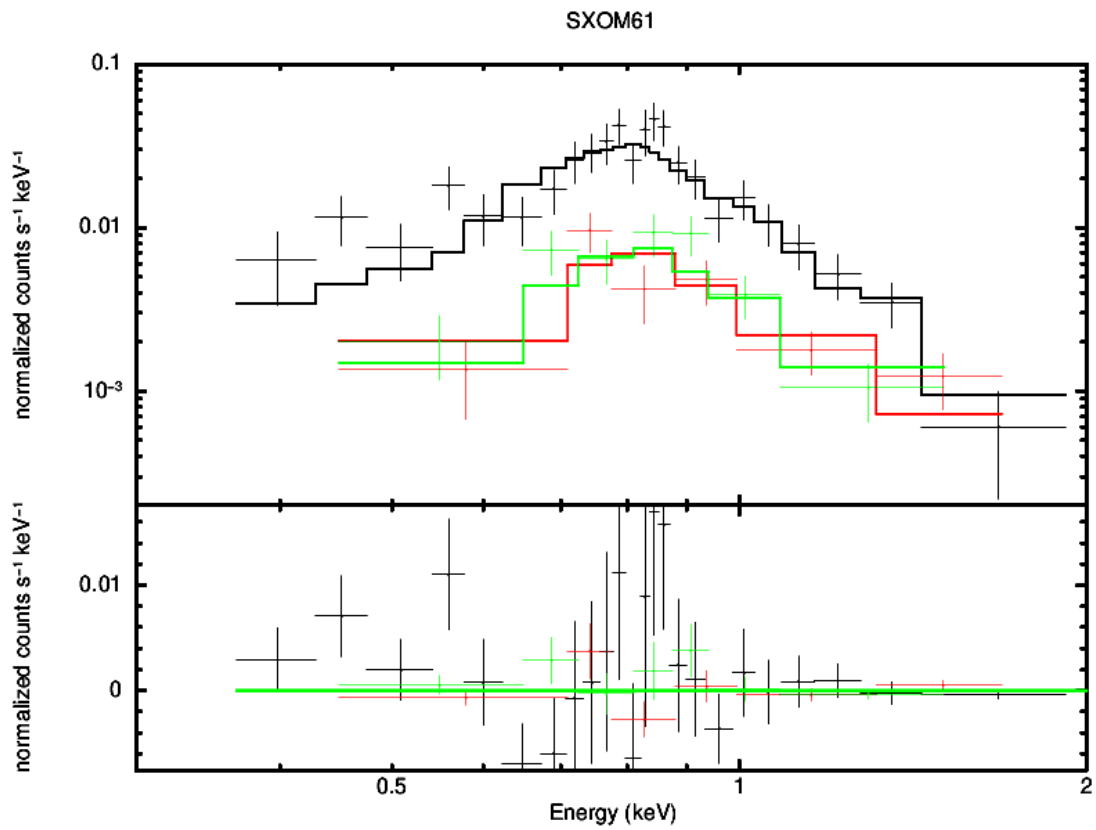
Figure 2.8: X-ray spectrum of SXOM61. The black, red and green points are MOS1, MOS2 and PN observed flux data points with error bars respectively. The best fitting tbabs*apec model is indicated by black, green and red lines for MOS1, PN and MOS2 respectively.

We performed the spectral fitting using the XSPEC (Arnaud, 1996) software package. The PN, MOS1 and MOS2 background subtracted source spectra were loaded in XSPEC, and the spectral groups containing channels with energies < 0.3 keV and > 2.0 keV were ignored. The X-ray spectra of SXOM61 obtained from PN, MOS1, and MOS2 were fitted simultaneously using collisionally-ionised plasma (apec) model with one characteristic plasma temperature multiplied with an absorber model (tbabs). We estimated the hydrogen column density N_H value from the standard relation for dust and extinction for our Milky Way Galaxy, $N_H/A_V = (2.08 \pm 0.02) \times 10^{21}$ H cm^{-2} mag^{-1} (Zhu, et al., 2017). For an E(B-V) = 0.13 along the line of sight of NGC 2527, we found that $N_H = (8.12 \pm 0.08) \times 10^{20}$ cm^{-2}, and we fixed the column density to this value in the tbabs model. We used a common value for the metallicity of all the elements relative to the solar abundance values as given by Asplund, et al. (2009). We used the χ^2_{red} minimization method to determine the best fitting model. At first we determined the best fit parameters for the models using the elemental abundance values fixed to 1 relative to the solar. The observed X-ray spectra of SXOM61, along with the best fitting model are shown in Figure 2.8. The best fit model parameters are given in Table 2.4. We also tried a fixed value for the sub-solar metallicity, fixed to 0.3 solar usually seen in many X-ray active late type stars Briggs & Pye (2003) and performed the spectral fitting again and obtaining the best fit temperature of the plasma and its normalization. There was little change in the χ^2_{red} value in between the sub-solar and solar fits (see Table 2.4). We estimated the X-ray flux coming from SXOM61 in the 0.3-2 keV energy band for both the solar and sub-solar fits using the task 'flux' in the XSPEC. The total flux in the 0.3-2 keV energy band of SXOM61 from the X-ray spectrum is $(2.1 \pm 0.2) \times 10^{-14}$. There is no significant difference in the estimated flux from a solar and sub-solar fits (see Table 2.4).

We obtained the energy conversion factor (ECF = Flux/Rate) using the estimated flux and MOS1 count rate of SXOM61 in the 0.3-2 keV energy band. The value of the ECF is found to be 1.73×10^{-12} ergs cm^{-2} counts^{-1}. We used this value of ECF to calculate the X-ray fluxes of the other 11 X-ray cluster members. The corresponding X-ray Luminosity was calculated using the formula L = $4\pi \, d^2 \, F_X$ where F_X is the X-ray flux of sources and d is the distance of source obtained from Gaia. The estimated X-ray fluxes and luminosity are reported in Table 2.3. We used the 'esensmap' task to generate a background sensitivity map of MOS1 soft and hard band image for an ML of 10 and took it's median value to estimate the detection limit of rate (counts s^{-1}). For a given XMM EPIC image, the 'esensmap' task (part of the 'emchain' task) creates a sensitivity map giving point source detection upper limits for each image pixel. The median background count rate in the soft band and hard band in the XMM MOS1 image is 0.00187 counts s^{-1}. The detection limit for the X-ray luminosity of cluster members is thus found to lie between $1.35 \times 10^{29} - 1.77 \times 10^{29}$ ergs s^{-1} cm^{-2}.

2.3.7   Spectral Energy Distribution of UV sources

The optical CMD given in Figure 2.4 shows that many sources detected in the UV and X-rays are located along single and binary isochrones, while a few other

stars deviate from these isochrones. To understand the physical properties of these stars, it is essential to estimate their fundamental parameters that include luminosity ($L_\odot$), radius ($R_\odot$), mass ($M_\odot$), and effective temperature (T_{eff}). These parameters can be derived by fitting UV to IR Spectral Energy Distribution (SED) of these stars with Kurucz models (Castelli, et al., 1997). Kurucz model library consists of 3808 discrete stellar atmosphere models with a unique set of T_{eff}, metallicity and $\log g$ parameters. The T_{eff} of these models ranges from 3500 to 50000 K and $\log g$ from 0.0 to 0.5 dex. The available Kurucz model metallicities are -2.5, -2.0, -1.5, -1.0, -0.5, 0.0, 0.2 and 0.5.

The SEDs of X-ray and UV bright stars were constructed by combining observed photometric data from UV (XMM OM - UVW2 and UVM2; UVOT - UVM2, UVW2, and UVW1), optical (Gaia - G, G_{BP} and G_{RP}; Paranal - u, g, r, Halpha, and i; MISC/APASS B and B; PAN-STARRS - g, r, z, y and i), near-infrared (2MASS - J, H, and K_s), and mid-infrared (WISE - W1, W2) observations. We used the Virtual Observatory SED Analyzer (VOSA) (Bayo et al., 2008) tool to obtain the fluxes in optical (Gaia, APASS, Paranal, and PAN-STARRS) and IR (2MASS and WISE) bands within a search radius of 5". We downloaded the Kurucz model synthetic flux from VOSA for these bands. VOSA corrects the observed flux for extinction in their respective wavebands using the extinction law of Fitzpatrick (1999) improved by Indebetouw, et al. (2005) in the infrared. The dereddened fluxes in optical and infrared bands are given in online-only Tables B and C.

Since VOSA only performs single spectrum SED fitting which is not suited for potential binary stars, we developed a python code for SED analysis that can perform both single and composite spectral fitting. The code constructs the observed SED and compares the observed flux with the synthetic Kurucz model flux using χ^2_{red} statistical analysis. The synthetic Kurucz model fluxes are scaled by a variable scaling parameter $M_d = (\frac{R}{D})^2$, which is optimized using Nelder-Mead optimization technique to get the least χ^2_{red} for each model. For each Kurucz model, the code finds the optimum scaling parameter to minimize the χ^2_{red}. It compares the optimum value of χ^2_{red} for each model and returns the best fit model parameters whose χ^2_{red} is closest to 1. The code also estimates the residual flux, where Residual $= \frac{ObservedFlux - ModelFlux}{ObservedFlux}$.

For a single spectrum SED fitting, the χ^2_{red} function is given by eqn. 2.2. In the case of composite spectrum fitting, the sum of fluxes of two Kurucz models is compared with the observed fluxes using eqn. 2.3. The composite spectrum obtained by the addition of two Kurucz model spectra is referred to as Kurucz and Kurucz model.

$$\chi^2_{red} = \frac{1}{N - N_{fit}} \sum_{i=1}^{N} \left\{ \frac{(F_{o,i} - M_d F_{m,i})^2}{\sigma^2_{o,i}} \right\} \qquad (2.2)$$

where N is the number of photometric data points, N_{fit} is the number of free

parameters in the model, $F_{o,i}$ is the observed flux, $M_d F_{m,i}$ is the model flux of the star, and $\sigma_{o,i}$ is the error in the observed flux, $M_d = (\frac{R}{D})^2$ is the scaling parameter, R is the radius of the star, and D is the distance to the star.

$$\chi^2_{red} = \frac{1}{N - N_{fit}} \sum_{i=1}^{N} \left\{ \frac{(F_{o,i} - M_d^1 F_{m,i}^1 - M_d^2 F_{m,i}^2)^2}{\sigma_{o,i}^2} \right\} \tag{2.3}$$

where N is the number of photometric data points, N_{fit} is the number of free parameters in the model, $F_{o,i}$ is the observed flux, $F_{m,i}^1$ and $F_{m,i}^2$ is the model flux of first and second component respectively, $\sigma_{o,i}$ is error in the observed flux, M_d^1 and M_d^2 are the scaling parameters for the first and second component.

We obtained T_{eff}, log g, and metallicity from the best fitting Kurucz model parameters. We estimated the radius, $R_\odot$, from the scaling parameter M_d, and bolometric luminosity ($L_\odot$) of the star using eqn 2.4. We found the mass of the star by comparing the estimated luminosity and temperature with the best fitting PARSEC isochrone. The uncertainties in $R_\odot$ and $L_\odot$ were estimated using eqn. 2.5 and eqn. 2.6 respectively.

$$L = 4\pi R^2 \sigma T^4 \tag{2.4}$$

where R is the radius of star, σ the Stefan-Boltzmann constant and T is the effective temperature of star estimated from SED fitting.

$$\triangle R = \frac{R \triangle D}{D} \tag{2.5}$$

where $\triangle D$ is the uncertainty in distance for each star given in Table 2.3.

$$\triangle L = L \sqrt{\left(\frac{2 \triangle R}{R}\right)^2 + \left(\frac{4 \triangle T}{T}\right)^2} \tag{2.6}$$

where $\triangle T$ is the uncertainty in T.

We estimated the fundamental parameters of 53 cluster members that were detected by XMM-OM and Swift UVOT. The metallicity of the NGC2527 cluster is near solar ([Fe/H] = -0.1, Reddy, et al. 2013). The metallicities of Kurucz models that bracket this value are [Fe/H] = 0.0 and -0.5. In our analysis, we thus adopted the [Fe/H] = 0.0 models. Given the near-solar metallicity of the cluster, this simplification is unlikely to have a significant impact on the SED fits.

If a star shows residual flux in excess of more than 50% in UV band, it is classified as having UV excess. 23 out of 53 stars are found to show an excess in the UV band. 10 stars are found to show a prominent dip feature near 2250 Å. The fundamental parameters of these stars are given in Table 2.5. A closer inspection of PAN-STARRS, 2MASS, and WISE images shows that three stars SXOM12, SXOM17, and SXOM56 are multiple stars that are resolved in the PAN-STARRS

image but are unresolved in the WISE and 2MASS images. So the results obtained from SED fitting of these stars are deemed spurious.

Of the remaining 20 stars that show UV excess, 14 are MS stars, 4 are binary stars, and 2 are RGB stars according to their position in the CMD. In order to understand the nature of excess UV residual, and determine the fundamental parameters of both the components in binaries, we performed composite spectrum SED fitting for 4 binaries and 2 RGB stars that show UV excess. In addition, we also performed composite spectrum SED fitting for 4 more binary stars which emit in X-rays. A comparison of single and composite spectrum SED fit of these stars is summarized in Table 2.6. The single component and double component SED fits are shown in Fig. C and Fig. D respectively. We present the results below.

2.4 Results

2.4.1 Fundamental properties of NGC 2527

In the very early studies of NGC 2527 by Lindoff (1973) and Dodd, et al. (1977), they had estimated the age to be around 500 Myr and 1 Gyr, with reddening E(B−V) = 0.077 ± 0.016, and a distance modulus of 8.70 mags. Since these studies had limited coverage in area and photometric depth, the sample of cluster members is incomplete, and estimated parameters were not reliable. Cantat-Gaudin, et al. (2018a) determined the membership of cluster stars using Gaia-TYCHO astrometric solution and found the age of NGC 2527 to be around 1 Gyr, metallicity [Fe/H] = -0.26 ± 0.11, E(B−V) = 0.077 ± 0.016 and V−M_V = 8.37 ± 0.10 mag by fitting isochrones to CMD based on 2MASS magnitudes. They used an automated code BASE-9 to determine these parameters, but the estimated metallicity is relatively lower as compared to the average value of [Fe/H] = -0.1 (Reddy, et al., 2013) obtained from spectroscopic studies of RGB stars. Also, the distance modulus was lower than that obtained from Gaia DR2. Siegel, et al. (2019) fitted PARSEC isochrones to UV CMDs and found an age of 450 Myr, with a distance modulus of V−M_V = 8.7 and a reddening E(B−V) = 0.04 mag. They assumed a lower distance modulus obtained from early studies of the cluster by (Dodd, et al., 1977), which led them to estimate a younger age for the cluster.

In this study, we determined the fundamental parameters of NGC 2527 by fitting PARSEC isochrones to the CMD based on Gaia magnitudes. The unprecedented coverage and depth in the photometry offered by Gaia DR2, allows us to cover a complete sample of cluster members. We find that the age of NGC 2527 is ∼ 630 Myr, reddening as E(B−V) = 0.13 mag, and distance modulus as $G − M_G$ = 9.0 ± 2.4 mag from the isochrone fitting. The average radial velocity of cluster members from Gaia DR2 radial velocity measurements is 41 ± 9 km/s.

Table 2.5: Fundamental parameters of cluster members detected in X-ray and UV, estimated from single Kurucz spectrum SED fitting. Column 1 gives the ID of stars detected in X-ray or UV, columns 2, 3 and 6 list the T_{eff}, log g and reduced χ^2 of the best fitting Kurucz spectrum, columns 4 & 5 list the estimated luminosity and radius, columns 7 and 8 indicate whether a Excess and Dip feature is observed in the residual plots of the single spectrum SED fit.

SXOM	T_{eff} (K)	log g	Radius $(R_\odot)$	Luminosity $(L_\odot)$	Mass $(M_\odot)$	χ^2_{red}	Excess	Dip
1	7750±250	4.5±0.5	2.05±0.06	13.7±1.94	1.78	28.1	N	N
2	7250±250	3.5±0.5	1.24±0.03	3.8±0.55	1.35	48.81	N	N
3	7500±250	4.0±0.5	1.49±0.04	6.32±0.9	1.51	26.52	N	N
4	6250±250	3.5±0.5	0.93±0.01	1.19±0.19	1.09	70.31	Y	Y
5	8000±250	4.0±0.5	1.7±0.04	10.64±1.42	1.68	28.87	N	N
6	8750±250	4.5±0.5	2.25±0.05	26.66±3.31	2.03	14.47	N	N
7	7000±250	3.5±0.5	1.21±0.02	3.15±0.47	1.32	73.48	N	N
8	5750±250	3.0±0.5	1.2±0.02	1.41±0.25	1.1	65.94	Y	N
9	8500±250	4.0±0.5	1.73±0.04	14.13±1.79	1.78	29.83	N	N
10	6500±250	5.0±0.5	1.23±0.01	2.43±0.38	1.24	16.48	Y	N
11	6250±250	5.0±0.5	0.92±0.01	1.16±0.19	1.04	102.64	Y	Y
12	5250±250	0.5±0.5	0.68±0.01	0.32±0.06	0.82	165.27	Y	N
14	8000±250	4.0±0.5	1.8±0.04	11.91±1.59	1.73	31.54	N	N
15	5750±250	3.5±0.5	0.87±0.01	0.74±0.13	0.99	41.51	Y	N
16	6250±250	4.0±0.5	1.23±0.01	2.08±0.34	1.19	70.46	Y	Y
17	3500±250	3.0±0.5	1.75±0.08	0.41±0.12	0.85	2308.31	Y	N
20	6500±250	4.0±0.5	1.29±0.02	2.67±0.42	1.24	59.05	Y	Y
21	7500±250	3.5±0.5	1.33±0.03	5.0±0.7	1.44	58.19	N	N
22	7000±250	3.5±0.5	1.15±0.02	2.88±0.43	1.29	76.85	N	Y
23	6000±250	4.0±0.5	1.17±0.02	1.61±0.28	1.14	43.91	Y	N
24	7000±250	3.5±0.5	1.45±0.03	4.54±0.68	1.42	36.64	N	N
25	6000±250	3.0±0.5	0.89±0.01	0.91±0.15	1.0	37.52	Y	Y
26	7750±250	3.5±0.5	1.49±0.03	7.21±0.98	1.56	29.36	N	N
27	8500±250	4.5±0.5	1.82±0.11	15.53±2.62	1.83	19.76	N	N
29	7750±250	4.0±0.5	1.49±0.03	7.19±0.97	1.56	30.29	N	N
31	7500±250	3.5±0.5	1.78±0.03	9.03±1.25	1.63	49.17	N	N
33	7250±250	3.5±0.5	1.78±0.03	7.91±1.13	1.58	67.17	N	N
34	7000±250	4.0±0.5	1.71±0.04	6.34±0.96	1.51	84.42	N	Y
35	7500±250	4.0±0.5	1.48±0.03	6.27±0.88	1.51	27.38	N	N
36	8250±250	4.5±0.5	2.06±0.05	17.74±2.31	1.88	18.19	N	N
37	7750±250	4.5±0.5	1.7±0.03	9.44±1.27	1.63	36.24	N	N
39	5750±250	3.0±0.5	0.79±0.02	0.62±0.11	0.95	62.21	Y	N
40	8000±250	3.5±0.5	1.62±0.03	9.69±1.26	1.63	32.32	N	N
41	7500±250	4.0±0.5	1.45±0.03	5.97±0.83	1.49	26.99	N	N
42	5500±250	2.5±0.5	10.07±0.25	83.5±15.74	2.55	528.64	Y	N
43	8000±250	4.0±0.5	1.51±0.04	8.39±1.12	1.58	35.79	N	N
44	8750±250	2.0±0.5	1.99±0.06	20.92±2.69	1.95	11.07	N	N
45	7500±250	5.0±0.5	1.44±0.03	5.92±0.82	1.49	6.95	N	N
47	8000±250	4.5±0.5	2.71±0.06	27.0±3.57	2.03	14.05	N	N
48	7250±250	4.5±0.5	1.96±0.04	9.58±1.37	1.63	28.41	N	N
49	5000±250	0.5±0.5	0.67±0.02	0.25±0.05	0.8	43.69	Y	N
50	8000±250	4.0±0.5	1.93±0.06	13.8±1.9	1.78	27.81	N	N
51	5000±250	1.0±0.5	0.7±0.02	0.28±0.06	0.8	22.05	Y	N
52	5750±250	2.0±0.5	0.76±0.01	0.57±0.1	0.95	39.22	Y	N
53	7000±250	3.5±0.5	1.12±0.02	2.71±0.4	1.29	62.12	N	Y
54	8000±250	4.0±0.5	1.67±0.03	10.3±1.35	1.67	39.78	N	N
55	6000±250	2.5±0.5	0.82±0.01	0.78±0.13	0.99	38.47	Y	N
56	5500±250	5.0±0.5	0.72±0.01	0.43±0.08	0.85	339.48	Y	N
57	6500±250	3.0±0.5	0.92±0.01	1.35±0.21	1.1	94.06	Y	Y
58	5500±250	2.5±0.5	0.76±0.01	0.47±0.09	0.9	35.65	Y	N
59	6500±250	3.5±0.5	1.09±0.01	1.91±0.3	1.19	108.31	Y	N
60	8000±250	3.5±0.5	1.89±0.04	13.19±1.75	1.78	22.31	N	N
61	5500±250	2.5±0.5	9.68±0.19	77.21±14.37	2.45	228.28	Y	N
62	6250±250	3.5±0.5	0.92±0.01	1.17±0.19	1.09	72.79	Y	Y
65	5250±250	2.5±0.5	10.17±0.23	70.69±13.83	2.49	5.12	N	N

Table 2.6: Comparison of fundamental parameters of cluster members detected in X-ray and UV, estimated from single and composite Kurucz spectrum SED fitting. Column 1 gives the ID of stars detected in X-ray or UV. Columns 2 & 3 are T_{eff} and reduced χ^2 of the best fitting single Kurucz spectrum. Columns 4, 7, 9, and 11 list the estimated parameters of the first component in the Kurucz and Kurucz composite spectrum fit. Columns 5, 8, 10, and 12 list the estimated parameters of the second component in the Kurucz and Kurucz composite spectrum fit. Column 6 gives the reduced χ^2 of the best fitting composite spectrum.

| SXOM	T (K)	χ^2_{red}	T_1 (K)	T_2 (K)	χ^2_{red}	R_1 ($R_\odot$)	R_2 ($R_\odot$)	L_1 ($L_\odot$)	L_2 ($L_\odot$)	M_1 ($M_\odot$)	M_2 ($M_\odot$)
8	5750±250	65.9	7000±250	5500±250	37.0	0.37±0.0	1.18±0.01	0.3±0.04	1.14±0.21	0.82	1.04
16	6250±250	70.5	6000±250	8500±250	16.5	1.28±0.01	0.17±0.0	1.93±0.32	0.14±0.02	1.19	0.7
20	6500±250	59.0	7750±250	6000±250	21.1	0.46±0.01	1.31±0.02	0.67±0.09	1.99±0.34	0.95	1.19
23	6000±250	43.9	5750±250	8000±250	19.6	1.2±0.02	0.23±0.0	1.41±0.25	0.2±0.03	1.1	0.75
31	7500±250	49.2	8250±250	6500±250	4.5	1.09±0.02	1.56±0.03	4.96±0.63	3.91±0.62	1.44	1.34
33	7250±250	67.2	6500±250	8250±250	16.0	1.63±0.03	0.92±0.02	4.28±0.68	3.51±0.45	1.39	1.34
34	7000±250	84.4	6500±250	8500±250	25.7	1.73±0.04	0.55±0.01	4.79±0.77	1.42±0.18	1.42	1.1
42	5500±250	528.6	49000±1000	5250±250	496.6	0.01±0.0	11.17±0.28	0.65±0.06	85.38±16.81	-	2.55
48	7250±250	28.4	6750±250	8250±250	2.0	1.71±0.03	0.99±0.02	5.48±0.84	4.08±0.52	1.46	1.39
61	5500±250	228.3	5250±250	49000±1000	135.5	10.87±0.21	0.01±0.0	80.8±15.72	0.86±0.08	2.52	-
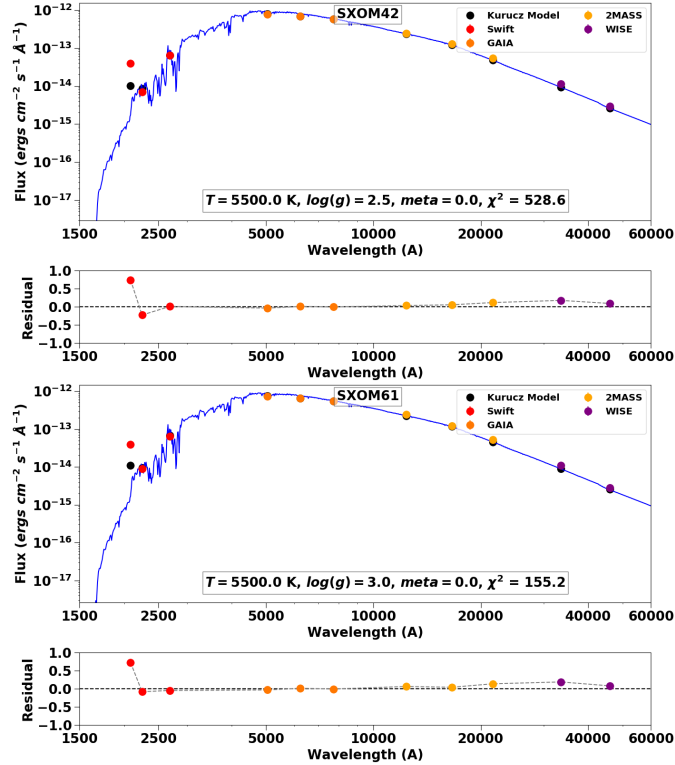
Figure 2.9: Broad band SED of two red giants that show excess UV flux. The best fit Kurucz spectrum is plotted over the observed SED and the fundamental parameters are given in each plot.

2.4.2 Red Giants

We detect 3 RGB stars in either X-ray or UV that lie in between single and binary isochrones in the optical CMD. SXOM61 emits in both X-ray and UV. SXOM42 lies in the field of view of XMM-EPIC detectors but is only detected in the UV. SXOM65 emits X-rays but is not detected in the UV observations because it lies outside the field of view of Swift UVOT and XMM-OM detectors. The RGB stars have high proper motion membership probability (given in Table 2.3), and their Gaia radial velocities are close to the mean radial velocity of the cluster. Therefore the RGB stars are kinematic members of the cluster.

SXOM61 and SXOM42 occupy a similar position in between the single and binary isochrone in UV CMDs, except in UVW2-G CMD. In UVW2-G CMD, they show an excess UVW2-G colour and lie close to the single star isochrone. The single spectrum SED fits to these 3 stars estimate $R_\odot \approx 10 \ R_\odot$ and $T_{eff} \approx 5500$ K respectively, which corresponds to a spectral type G2 III. SED residual plots of SXOM42 and SXOM61 (see Figure 2.9) show a 75% excess in UVW2 flux as compared to the Kurucz model flux of a G2 III star. The origin of excess flux in the UVW2 band in these stars could be due to chromospheric activity, presence of a hotter companion, or red leakage in the UVW1 filter. The composite spectrum fitting using a combination of Kurucz and Kurucz models does not significantly decrease the excess flux, and the best fit temperature of individual components is exceptionally high, making the fit unreliable. The flux of these RGB stars in UV filters is at least 10^4 times higher as compared to the detection limits suggests that the high flux is unlikely due to red leakage. Hence, the excess in UV is most likely due to high chromospheric activity or a hotter companion.

The X-ray spectrum of SXOM61 shown in Figure 2.8 is fitted by a single component plasma model that has a temperature of 0.62 ± 0.06 keV or $(7.1 \pm 0.7) \times 10^6$ K. The high plasma temperature is suggestive of a highly active corona. The X-ray luminosity (Lx) of SXOM61 and SXOM65 is 10.2×10^{29} ergs s^{-1} and 3.8×10^{29} ergs s^{-1} suggesting that both the stars have an active corona. As stars evolve off the main sequence, they undergo rapid loss of angular momentum as a result of magnetic breaking through coronal winds. Therefore, the RGB stars are slowly rotating stars with relatively less active corona. It is highly unlikely for a RGB star to have an active corona, unless it is tidally locked in a binary system or a fast rotating merger remnant of a contact binary, like FK Comae. The high coronal activity and excess UV flux hints that these stars are potential FK Comae candidates. It is a rare class of rapidly rotating late-type giants or subgiants, which show signs of active chromospheres and X-ray emission (Bopp & Stencel, 1981).

2.4.3 Main sequence stars

Coronally active

We detect X-ray emission from 5 main sequence stars. Two of these stars, SXOM63 and SXOM64, lie outside the field of view of XMM OM and Swift UVOT detectors;

therefore, we could not detect UV emission from them. We determined the fundamental parameters of other three stars (SXOM7, SXOM53, and SXOM59) by performing single spectrum SED fitting. The temperature of these stars suggests that they are F type stars and their X-ray luminosity is $\sim 10^{29}\ ergs\ s^{-1}$, suggesting that they are coronally active. The origin of the active corona is directly linked to the coupling of convection and rotation in these stars, which produces a solar-type dynamo. The magnetic field produced by the solar dynamo heats the plasma in stellar corona, which produces X-rays (Rosner, et al., 1978).

UV excess

The residuals of single spectrum SED fit of 10 stars (see Table 2.5) shows a decrease in flux around 2250 Å by $\sim$50% and then rise in flux around 1930 Å by $\sim$50%, as compared to the model flux (see Figure 2.10). The estimated temperature of these stars suggests that they are solar-type stars with temperature $\leq$ 6500 K. The prominent saddle dip in the observed SED of SXOM16, SXOM20, and SXOM57, hints towards the inefficiency of atmospheric models to characterize the absorption lines of cool stars. The combined spectro-photometric coverage of XMM-OM and Swift UVOT allows us to visualize the poorly characterized absorption line feature. SXOM16 and SXOM20 lie close to the binary isochrone, but their composite spectrum fit are ineffective because of the poor model fit in the UV band.

The single spectrum SED fitting of many MS stars show an excess in the UV band suggestive of chromospheric activity or the presence of a hot WD companion. The absence of a far-UV (FUV) flux data point makes it difficult to determine the nature of excess UV flux. The broad-band SEDs of these stars are shown in Figure 2.11. Sindhu, et al. (2018) also found several stars near and below the MSTO in M67 to show an excess in NUV band. They suggested that these stars could have high chromospheric activity. Reiners & Giampapa (2009) studied 15 solar-type stars in M67 and concluded that rapid rotation is the reason for the high chromospheric activity in these stars.

The broad-band SED of two of these stars, SXOM49 and SXOM51 shows huge excess flux in the Swift UVW1 and UVW2 filters, but are not detected in Swift UVM2 filter (see Figure 2.12). However, since these stars are not detected in UVM2, the excess flux in UVW1 and UVW2 filters could be due to red leak usually observed in Swift UVW1 and UVW2 filters, or the presence of a hot WD companion. Siegel, et al. (2012) have shown that if a cool K type star is detected and shows an excess in all three UVOT filters, only then it has a potential hot WD companion. Since SXOM49 and SXOM51 are not detected in UVM2 filter, the excess UV flux could be an artefact. A comparison of the best fitting model flux and observed flux of SXOM49 and SXOM51 with the detection limits (see Appendix B) of UVOT filters is given in Table 2.7. The observed flux in UVW2 and UVW1 bands are at least 10 times higher than the model flux and the detection limits. For the given detection limits, if the UV excess is due to the presence of a hot WD companion, we should have detected an excess flux in the UVM2 band as well.
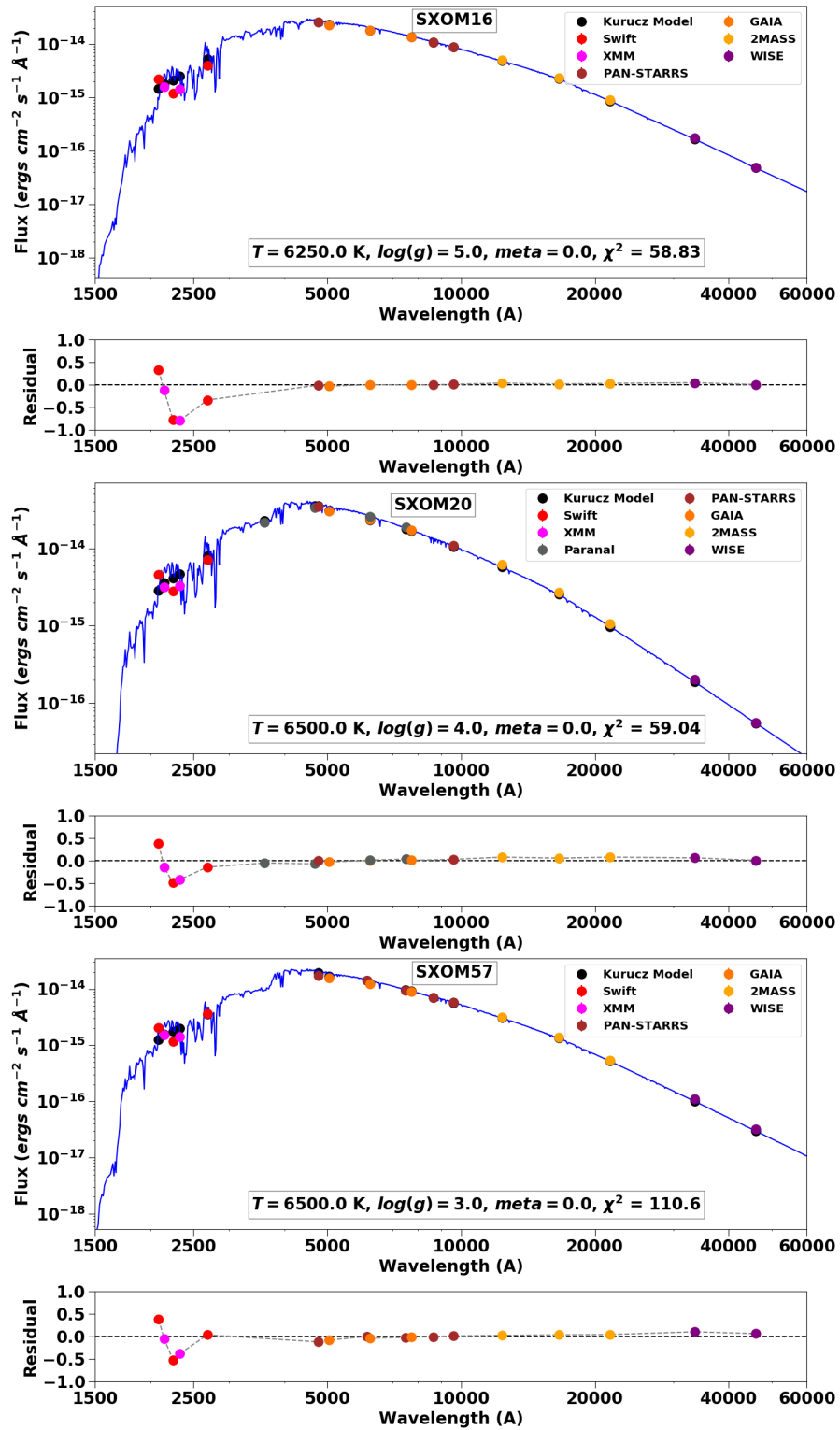
Figure 2.10: SED of stars that show a prominent dip around 2250 Å.
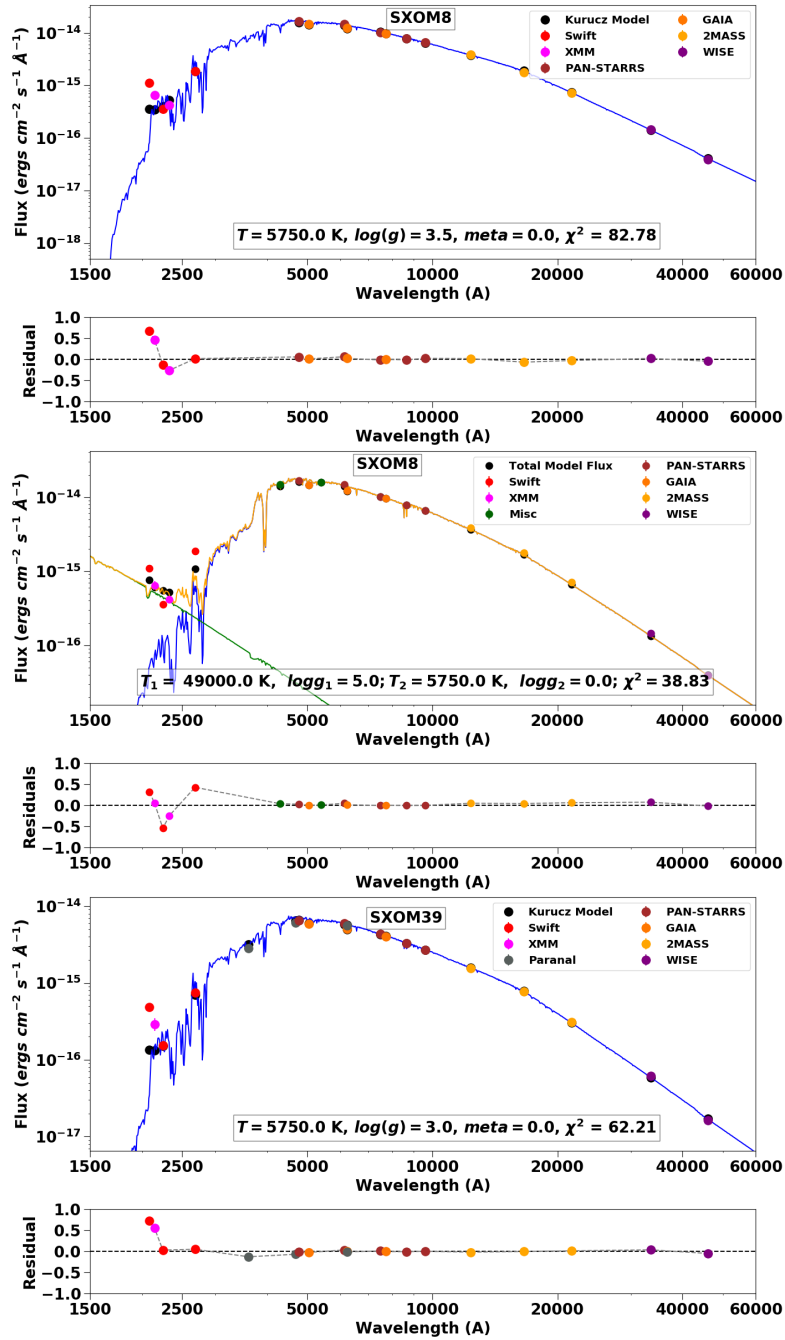
Figure 2.11: Spectral Energy Distribution of a few stars that show excess UV flux mostly due to high chromospheric activity. A comparison of single and double spectrum fitting of an active binary SXOM8 is shown.
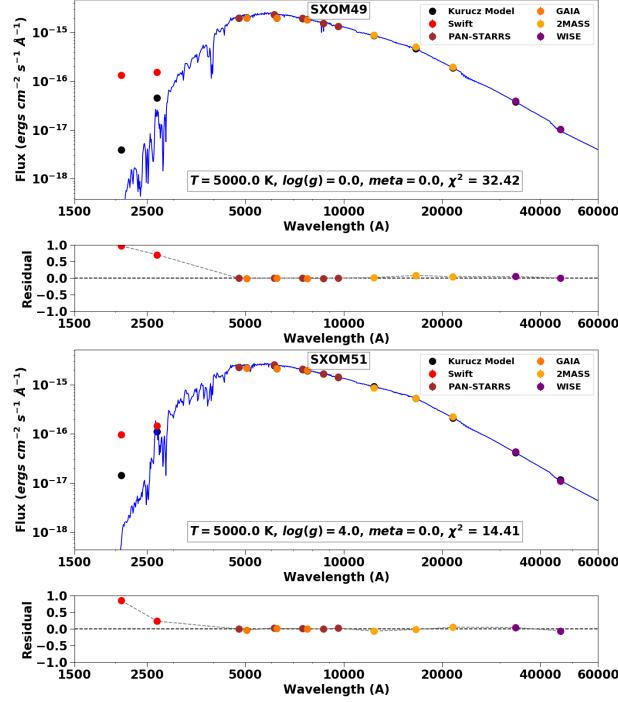
Figure 2.12: SED of two faint subgiant stars that show excess UV flux mostly due to red leak in UVW1 and UVW2 filters.

Table 2.7: Red-leak corrected observed flux of two cool subgiant stars which show UV excess. The units of flux is 10^{-18} ergs cm^{-2} s^{-1}. Column 2 gives the detection limit for each UVOT filter in the given observations, Column 3 gives the extinction corrected observed flux, Column 4 gives the red-leak and extinction corrected observed flux, Column 5 gives the best fitting Kurucz model flux, and Column 6 gives the percentage contribution from red leak ($\frac{Observed - Observed_{RC}}{Observed}$) in the Swift UVOT filters.

Filter	Background	Observed		Observed$_{RC}$		Model		% Red Leak in Observed Flux	
		SXOM49	SXOM51	SXOM49	SXOM51	SXOM49	SXOM51	SXOM49	SXOM51
UVW2	7	134	96	4	3	5	7	97	97
UVM2	8	-	-	-	-	2	3	-	-
UVW1	4	152	147	54	52	53	66	65	65

The stellar parmaters of stars (given in Table 5) that suffer from significant red leakage (SXOM49 and SXOM51) corresponds to a spectral type of G5 VI. From the spectral models available in Brown, et al. (2010), the spectral type closest to G5 VI is G5 V. To estimate the contribution from red leakage, we corrected the magnitudes of SXOM49 and SXOM51 using the red-leak magnitude correction factors for a spectral type G5 V given in Table 12 of Brown, et al. (2010). The red leak corrected magnitudes were converted to fluxes using the conversion factors given in Table 13 of Brown, et al. (2010) and the fluxes were corrected for extinction. The extinction and red-leak corrected observed fluxes, and the percentage contribution from red-leak is given in Table 7. For these stars, the red-leak contributes approximately 97% and 65% of the observed flux in the UVW2 and UVW1 filters, which is extremely high. Therefore, the UV excess in SXOM49 and SXOM51 is most likely due to red leakage.
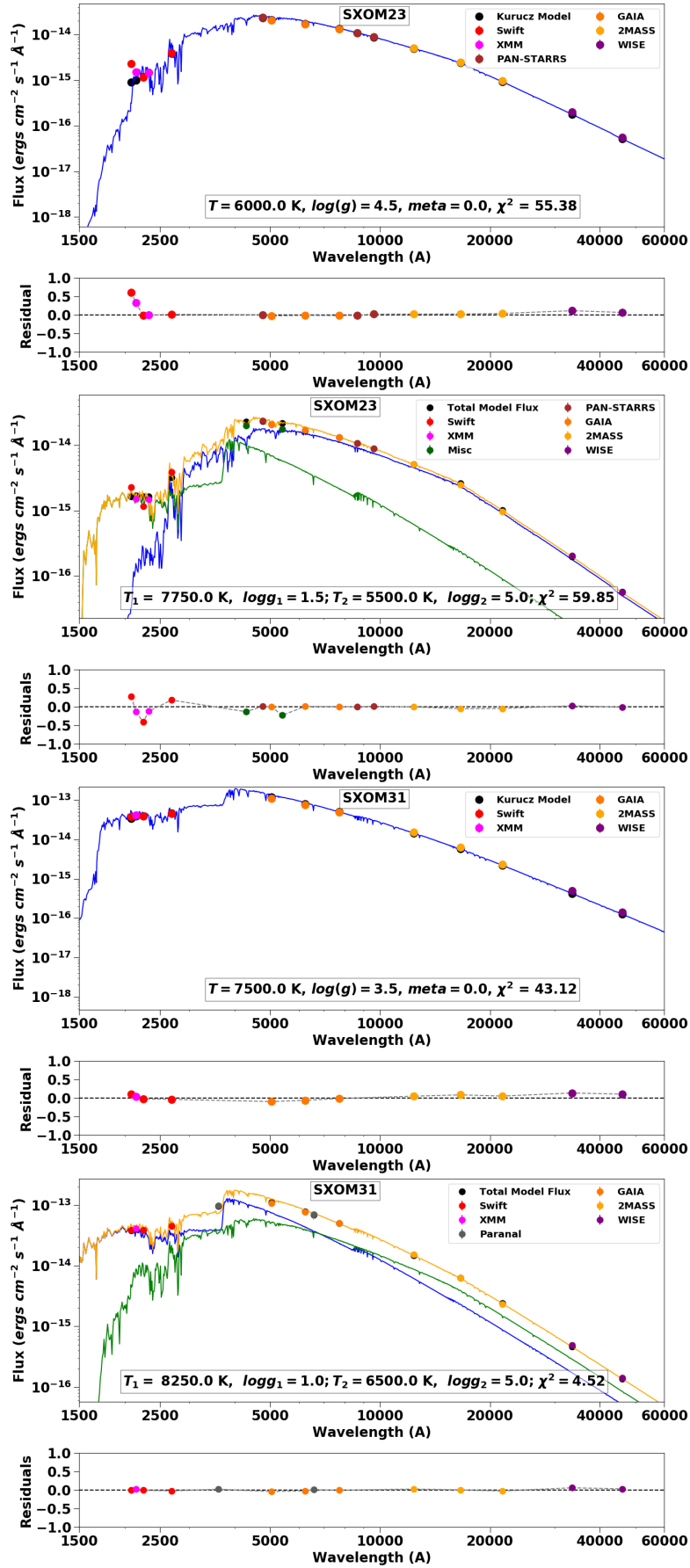
Figure 2.13: Multi-wavelength SED of 2 potential RS CVn candidates.

2.4.4 Potential Binaries

RS CVn Binaries

A few stars (SXOM23, SXOM31, SXOM33, SXOM34, and SXOM48) that lie close to the binary isochrone in the optical CMD are found to emit X-rays. SXOM23 is the only star which shows excess UV flux in single spectrum SED fit (see Figure 2.13). The composite spectrum fit of SXOM23 based on both Kurucz models gives reasonable parameters and also reduces the excess UV residual from 70% to 30%. The spectral type of hotter, and cooler star based on the estimated T_{eff} and radius (see Table 2.6) from composite Kurucz model fit is A8 V, and G4 V respectively. SXOM23 has an X-ray luminosity of $1.08 \times 10^{29}\ ergs\ s^{-1}$, typical L_X of RS CVn binaries. The χ^2_{red} of other stars decreases significantly on performing composite spectrum SED fit, suggesting that these stars are also potential binaries. Their X-ray luminosity is in the range $1.3 - 3.0 \times 10^{29}\ ergs\ s^{-1}$, typical of RS CVn type binaries. The X-ray observations and broad-band SEDs of these stars indicate that they are potential RS CVn binaries.

Sub-subgiant and Red Straggler

Sub-subgiants (SSGs) and red stragglers (RS) are peculiar stars that defy standard evolutionary models. We identify 5 stars in the optical CMD that are cluster members and lie in the SSG region and 1 star which lies in the RS region as defined by Geller, et al. (2017). Of these stars, only 1 SSG (SXOM47) is detected in UV. SXOM47 lies in the SSG region in the optical CMD. The other 5 stars are too bright and saturated or lie outside the fov of Swift UVOT and XMM OM detectors. Geller, et al. (2017) identified 43 SSG in previous studies of open and globular star clusters. These SSG belong to star clusters which are older than 2 Gyr. Of these 43 SSG stars, 25 are X-ray sources with typical 0.5-2.5 keV luminosities of order $10^{30-31}\ ergs\ s^{-1}$. SXOM47 lies in the fov of XMM detectors but is not detected, so we can estimate the upper limit of X-ray luminosity. SXOM47 is the first detection of a SSG in an intermediate-age open cluster with an upper limit of X-ray luminosity $\sim 10^{29}\ ergs\ s^{-1}$. SXOM47 lies in the region of optical CMD where SSGs are mostly formed by mass transfer mechanism as proposed by Leiner, et al. (2017).

Gap Objects

We identify 5 stars in the optical CMD which lie in the gap region similar to that found by Knigge, et al. (2002) in their FUV-optical CMD and Pala, et al. (2019) in the optical CMD based on Gaia filters. The stellar types which occupy these regions are Cataclysmic Variables (CV), MS+WD binaries, and He WDs. These stars lie outside the fov of XMM and Swift detectors, so are not detected in X-ray or UV. These stars are potential CV candidates which need further study.
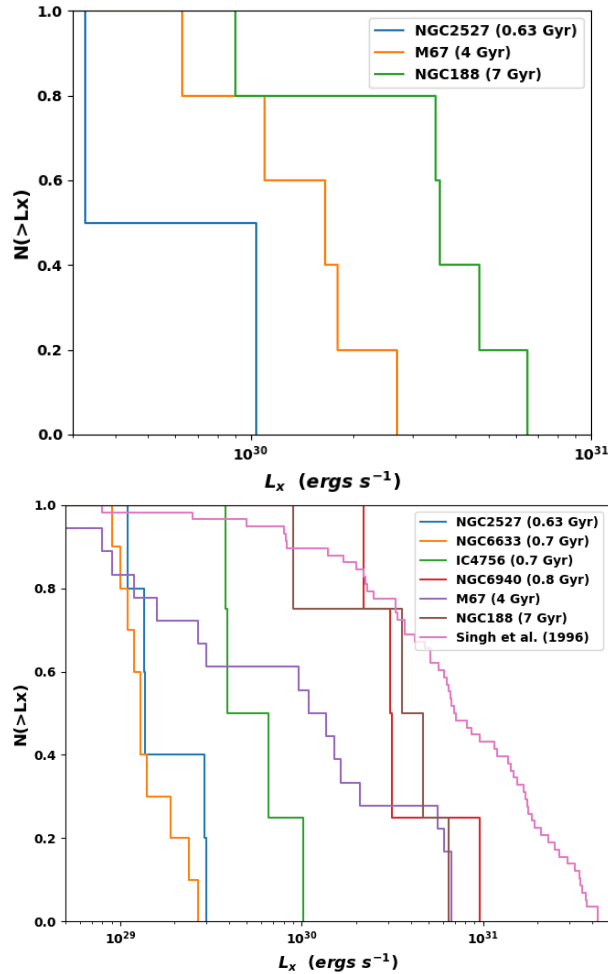
Figure 2.14: Comparison of the X-ray luminosity function of W UMa and FK Comae stars (top), and RS CVn binaries (bottom) observed in various open star clusters.

Active UV binary

SXOM8 lies close to the binary isochrone and shows significant excess in the UV band. Though the composite spectrum fit of SXOM8 reduces the χ^2_{red} as compared to the single spectrum fit (see Table 2.6), it does not reduce the excess flux significantly (see Figure 2.11). The excess UV flux and the position of SXOM8 in the CMD, suggests that it is a potential chromospherically active binary star.

2.5 Discussion

Though NGC 2527 is a nearby open cluster, it has hardly been studied in detail. The optical CMD of NGC 2527, with only definite members allows us to identify and study various stages of stellar evolution distinctly. Several non-standard stellar evolutionary products such as red stragglers, sub-subgiants, band gap stars, and active binaries are identified. Several open clusters in the $\sim$ a few Gyr age range have been extensively studied in X-ray. This study is an attempt towards characterization of UV and X-ray emission from a relatively younger cluster ($\sim$ 630 Myr) to throw light on the type of population which dominates emission in

these wavelengths. We have combined UV observations from Swift and XMM-OM, along with X-ray observations from XMM-EPIC to study the behavior of NGC 2527 members.

2.5.1 X-ray emission

We detect strong X-ray emission from 12 stars, out of which 2 are potential FK Comae candidates, 5 are RS CVn candidates, and 5 are MS stars which are coronally active. A comparison of X-ray luminosity function (XLF) of FK Comae and RS CVn stars in intermediate to old open clusters is shown in Figure 2.14. The star clusters used for comparison with NGC 2527 (0.63 Gyr) are : NGC 6633, IC 4756 (0.7 Gyr; Briggs, et al., 2000), M67 (4 Gyr; Mooley & Singh, 2015), and NGC 188 (7 Gyr; Belloni, et al., 1998; Gondoin, 2005). We have shown a comparison with the XLF of field RS CVn binaries (Singh, et al., 1996). NGC 6633 and IC 4756 do not have any significant detection of FK Comae type or contact binaries. The XLF suggest that the X-ray luminosity of both RS CVn and contact binaries increases with age i.e., more active binaries are present in older clusters as compared to younger clusters. Mooley & Singh (2015) have also compared the XLF of OCs of various ages, and they also find a similar trend.

Main sequence stars as they evolve off the main sequence undergo rapid loss of angular momentum as a result of magnetic braking through coronal winds. These massive RGB stars can emit X-rays only if they are fast rotating stars. Webbink (1976) modeled the formation of FK Comae stars by the coalescence of W UMa contact binaries. During the merger, the orbital angular momentum of the binary is converted to rotational momentum of the single star which spins it up. The high X-ray luminosity is most likely due to dynamo action induced by the rapid rotation. Recently Howell, et al. (2016) found 18 rapidly rotating FK Comae type of stars, in a sample of bright X-ray sources in the Kepler field. The detection of 2 potential FK Comae candidates suggests that there are many other hidden contact binaries or post-interaction mass transfer products lying along the main sequence in intermediate-age OCs.

2.5.2 UV emission

We detect UV excess from several stars lying close to the main sequence and binary isochrone, or the red giant branch in the optical CMD. The UV excess in these stars could be due to high chromospheric activity, presence of a hot WD companion or red leakage in UVW2 and UVW1 filters. The absence of a FUV flux data makes it difficult to distinguish between chromospheric activity and the presence of a WD companion.

We find that cool subgiant stars (T $\leq$ 5000 K) whose flux is close to detection limits could suffer from significant red leakage. These stars are detected only in UVW1 and UVW2 filters that suffer from red leak at optical wavelengths, suggesting that the UV excess in these stars is an artefact. Though RGB stars have
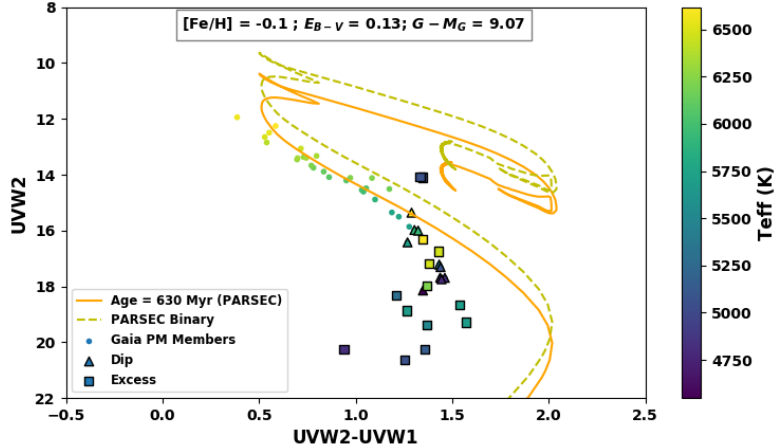
Figure 2.15: UV-optical CMD of NGC 2527 based on UVW2 magnitude. The best fitting PARSEC isochrone along with an equal mass binary isochrone is overlaid on the observed CMD. The stars which show a prominent dip feature in the SED and excess NUV flux are marked as triangles and squares respectively.

similar temperatures (T $\sim$ 5000 K), their intrinsic flux is $\sim 10^3$ larger than the cool subgiant stars. Therefore, the origin of UV excess in the RGB stars is a reliable feature.

In a recent study of UV population in M67 by Sindhu, et al. (2018), they detected 2 RGB stars which show excess in the GALEX NUV and FUV bands and the presence of Mg II h+k emission lines in the UV spectra suggestive of chromospheric activity. The models explaining the origin of chromospheric activity are not yet well-established (Pérez Martínez, et al., 2011). The chromospheric activity could be due to acoustic heating of the atmosphere (Schrijver, 1995) or magnetic activity. Since SXOM42 is not observed in X-ray, the origin of the excess UV flux can be attributed to acoustic heating of the atmosphere leading to high chromospheric activity.

Several cool stars deviate from the single star isochrones in the UVW1-UVW2 CMD as shown in the Figure 2.15. Siegel, et al. (2019) had also identified this strange feature in the UVW2-UVW1 CMDs of a few star clusters. They had suggested that this feature could be due to red leak in UVW1 and UVW2 filters or deficiencies in the underlying atmosphere models. According to the broad-band SED, most of these stars show a prominent saddle dip feature around 2250 Å indicating the presence of strong absorption lines. These UV absorption features are not well characterized by atmosphere models of cool stars. The UVBLUE project by Rodríguez-Merino, et al. (2005, 2009) and Chavez, et al. (2007) also highlights this problem of incomplete characterization of absorption features in cool stars. They had retained the models longward of 2200 Å for intermediate-type F, and G stars as the lower wavelengths do not properly fit the observed spectrum. In Figure 2.15 the stars have been differentially coloured based on their Teff obtained by comparing the optical magnitudes with the best fitting PARSEC isochrone. We notice that the deviation of these cool stars from isochrones begins around 6500 K, which is similar to that identified by Siegel, et al. (2019). These

deviations from isochrones have also been noted in NUV photometry of cool stars by Barker & Paust (2018). The conspicuous dip feature in most of these stars suggests that the deviations are likely due to the inefficient characterization of absorption lines in atmospheric models of cool stars.

2.6   Summary of Results

The main results of our study are as follows:

1. We have re-estimated the fundamental parameters of NGC 2527 based on the recent Gaia DR2 data, and find an age of 630 Myr, distance of 642±30 pc, and a mean radial velocity of 41 ± 9 km/s. We estimate a reddening of 0.13 mag in the direction of this OC.

2. We have discovered 5 MS stars that show high coronal activity and are potentially fast-rotating stars of F spectral type.

3. We have discovered 2 potential FK Comae stars. One of these RGB stars shows strong X-ray and UV emission.

4. We have characterized the fundamental parameters of 5 active binaries that emit X-rays and are potential candidates for being RS CVn type binaries.

5. We have identified a sub-subgiant star with an upper limit of X-ray luminosity as $\sim 10^{29}$ $ergs$ s^{-1} − first such detection in an intermediate age OC.

6. We confirm that the X-ray luminosity of both RS CVn and contact binaries increases with age suggesting that more active binaries may be present in the old and intermediate age open clusters.

7. This study also suggests possible presence of W UMa and FK Comae type stars in younger (age $\simeq$ 630 Myr) clusters.

Chapter 3

Future Work

3.1 Evolution of binary systems

Several stars in the CMDs of OCs deviate from the standard evolutionary tracks, making them peculiar. The most common of these peculiar stars are Blue Straggler Stars (BSSs) that are bluer and brighter than the Main Sequence Turn Off (MSTO) in the CMD. BSSs make up only half of the population of peculiar stars. The other half of the peculiar stars include Yellow Stragglers (YSs) lying between the BSS region and the RGB, Red Stragglers (RSs) that are brighter and redder than the giant branch, Sub-Subgiants (SSGs) which are fainter and redder than the giant branch, Blue Lurkers (BL) are fast rotating stars along the MS, Far-Ultraviolet (FUV) bright stars along the MS and Bright Gap (BG) stars lying between the MS and WD region.

3.1.1 Gaps in binary evolution

There are several gaps in understanding the formation mechanism of these peculiar stars. The anomalous position of BSSs in the CMD indicates that they are more massive than the other visible stars in the cluster, as direct mass estimates also confirm it (Ferraro, et al., 2006; Baldwin, et al., 2016). Therefore, BSSs are proposed to have formed through various channels such as mass-transfer in binary systems (McCrea, 1964) and stellar mergers due to direct collisions (Hills & Day, 1976). Even though some of the evolved BSSs are detected as YSs and RSs in the CMDs, it is difficult to detect the old post-interaction BSSs with cold WD companions (Ferraro, et al., 2016). Recently, 11 fast-rotating MS stars were found in M67 (Leiner, et al., 2019). These stars also known as blue lurkers (BL) are rejuvenated by mass-transfer/mergers like the BSSs but blend with the normal MS population in the CMD. The identification of BL provides the first picture of the low-luminosity end of the blue straggler distribution. Apart from BSSs and BL, recently Sindhu, et al. (2018) using GALEX have found 15 FUV bright MS stars in M67 which can harbour a hot companion or be chromospherically active. Using UVIT FUV observations of M67, Jadhav, Sindhu & Subramaniam (2019) detected a few potential post-MT binaries and extremely low mass WD companions to stars lying along the main-sequence. The detection of these peculiar stars

clearly shows the need to account for the impact of binaries on stellar evolution, as a significant number of post-interaction binaries exist on the main sequence.

3.1.2 Asteroseismology of BSS

In many clusters, BSS lie in the classical instability strip, i.e. in the region occupied by classical pulsating stars like δ Scuti and SX Phe oscillations. It is difficult to discriminate whether a BSS is formed from coalescence or stellar collisions. Gilliland & Brown (1992); Gilliland, et al. (1998) have identified oscillating BSS in old OCs like 47 Tuc and M67. The oscillations can be used to model the interior of the BSS. Detailed asteroseismic studies of OCs can allow us to compare the oscillation frequencies of stars and BSSs.

3.1.3 X-ray emission from RS

Till now RS has only been detected in X-ray studies of old OCs or GCs (Belloni, et al., 1998; van den Berg, et al., 2013; Shishkovsky, et al., 2018). To explain the X-ray emission from RS, Shishkovsky, et al. (2018) have proposed several mechanisms like flares from accreting white dwarf companion, ionized red straggler wind, and coronal emission. Though the average X-ray luminosity of RS is $\sim 3 \times 10^{30}$ ergs s^{-1}, the number of X-ray counts in their spectra were insufficient to perform spectral analysis in the previous observations. Therefore, the fundamental mechanism of X-ray emission from RS remains unknown.

3.1.4 Extended main sequence turn-off

The origin of multiple populations in intermediate-age clusters is one of the most intriguing open issues in stellar astrophysics. Several recent studies of OCs in Milky Way show an extended main sequence turn-off (eMSTO) in the optical and UV Color-Magnitude Diagrams (CMDs) (Marino, et al., 2018; Siegel, et al., 2019). The main cause for eMSTO is likely to be stellar rotation. It is found that rapidly-rotating stars are more red-shifted in the CMDs as compared to slow rotators. These fast-rotating stars that lie close to the eMSTO could be post-mass transfer products in a close binary system, or spun-up intrinsically due to star formation.

3.2 Proposed observations

An extensive X-ray and UV study of OCs combined with optical Gaia data can unveil the exotic population of binaries and bridge the gap between various stages of binary stellar evolution. We successfully proposed deep FUV UVIT observations of an OC NGC 2506, and XMM-Newton observations of the OC NGC 6940 to
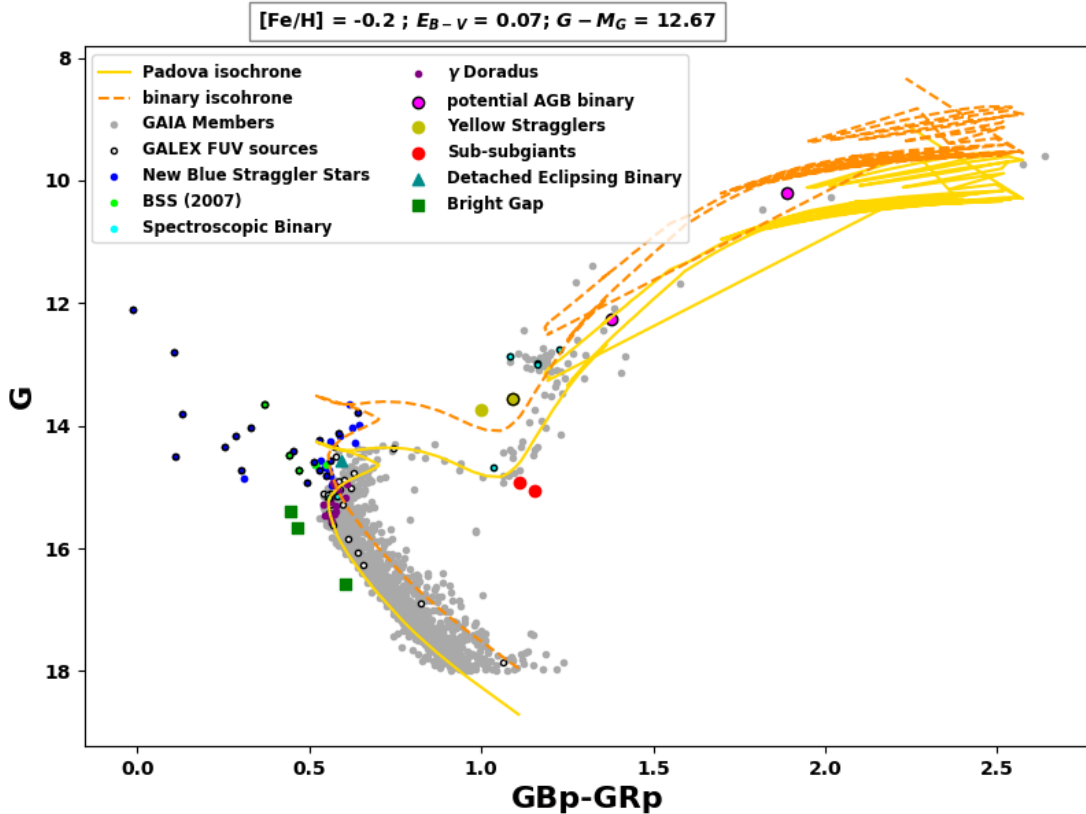
Figure 3.1: Optical CMD of NGC 2506 based on Gaia magnitudes. The best fitting isochrones are overlaid on the CMD, and the peculiar stars are marked with different colors.

study these peculiar stars. Of these NGC 2506 has already been observed and a preliminary analysis of suggests the presence of several post-mass transfer products like low mass He-core WD binaries, fast-rotating stars (FK Comae, BY Dra), BSS, RS, and other active binaries. A detailed study of these clusters will allow us to connect the various stages of binary stellar evolution.

3.3 NGC 2506: Younger sister of M67

NGC 2506 ($\alpha_{2000} = 08^h00^m01^s$, $\delta_{2000} = -10° 46' 12''$) is a metal deficient old open star cluster, i.e. slightly younger then M 67. The first photometric study of NGC 2506 was done by McClure, Twarog & Forrester (1981) and they derived the age of NGC 2506 as 3.4×10^8 years. Marconi, et al. (1997) determined the cluster parameters as distance modulus = 12.6±0.1 mag, age = 1.5-2.2 Gyr and E(B-V) = 0-0.07 mag. A more recent study by Lee, Kang & Ann (2012) investigated this cluster using VI CCD data and estimated E(B-V) = 0.03 ± 0.04 mag, age = 2.32 ± 0.16 Gyr, and [Fe/H] = -0.24 ± 0.06 dex. It is a mildly elongated cluster, spread over a radius of 6' and lies at a distance of ∼3500 pc. The previous studies of NGC 2506 have identified oscillating BSS, spectroscopic binaries, γ Doradus and spectroscopic binaries making this cluster an ideal target to connect various stages of binary stellar evolution (Chiu & van Altena, 1981; Anthony-Twarog, et al., 2018; Arentoft, et al., 2007).
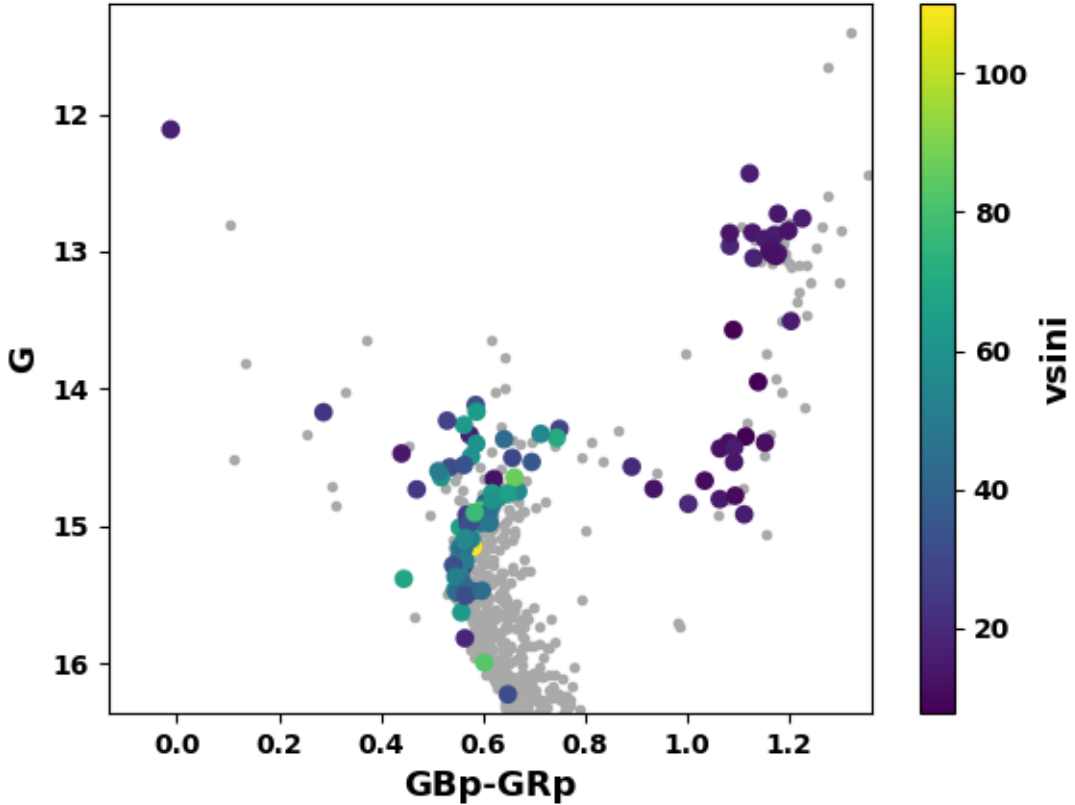
Figure 3.2: Variation of rotational velocity of stars across the optical CMD of NGC 2506.

3.3.1 Preliminary study

We performed a preliminary study of NGC 2506 using Gaia, and GALEX UV data of NGC 2506. We obtained the Gaia photometric magnitudes and membership probability of cluster members from the Gaia DR2 open cluster population in Milky Way Catalogue (Cantat-Gaudin, et al., 2018b). Optical CMD of NGC 2506 based on Gaia magnitudes is shown in Fig. 3.1. The grey points are the stars with cluster membership probability greater than 50%. We used the Gaia parallaxes of cluster members and inferred the mean distance to NGC 2506 to be 3424 pc, which corresponds to a distance modulus of $G - M_G = 12.7$ mag. We find that a 2 Gyr Padova isochrone with E(B-V) = 0.07 best fits the observed CMD. We have identified various peculiar stars BSS, gap stars, RS, YS, potential AGB binary/symbiotic stars and SSG that deviate from standard evolutionary isochrones (see Fig. 3.1). The sources detected in GALEX FUV are marked as black circles, and the spectroscopic binaries, γ Doradus, BSS, and detached eclipsing binary as identified in previous studies of NGC 2506 are marked in the CMD. The v sini measurements of the MS stars observed in the WIYN OC survey (Anthony-Twarog, et al., 2018), show a huge spread from $\sim$ 20 - 110 km s^{-1} (see Fig. 3.2). These fast-rotating stars (vsini > 80 km s^{-1}) are potential BLs or BSS candidates which host WD companions.

Filter	Exposure Time (s)
F148W	9142
F154W	7452
F169M	7202

Table 3.1: Summary of UVIT observations.

Table 3.2: Summary of total number of sources, and cluster members observed in Gaia, GALEX and UVIT fov of NGC 2506.

Energy Band	No. of observed sources	No. of cluster members
Gaia Optical	1520	1498
GALEX FUV	366	51
UVIT F148W	771	401
UVIT F154W	634	348
UVIT F169M	466	275

3.3.2 UVIT Observations and Analysis

Photometry

We obtained deep FUV band observations of NGC 2506 using the Ultra-Violet Imaging Telescope (UVIT) onboard the Indian space observatory, AstroSat. A summary of UVIT observations of NGC 2506 is given in Table 3.1). UVIT data were corrected for distortion, flat fielding, and spacecraft drift using the CCDLAB (Postma & Leahy, 2017). A comparison of UVIT and GALEX images of the same field of view is shown in Fig. 3.3. The deep UVIT observations allow us to detect a large number of sources as compared to GALEX. We corrected the astrometry of the UVIT images using IRAF task ccmap. We performed point-spread function photometry on all the UVIT images using standard IRAF routines to obtain the aperture corrected magnitudes in all the filters.
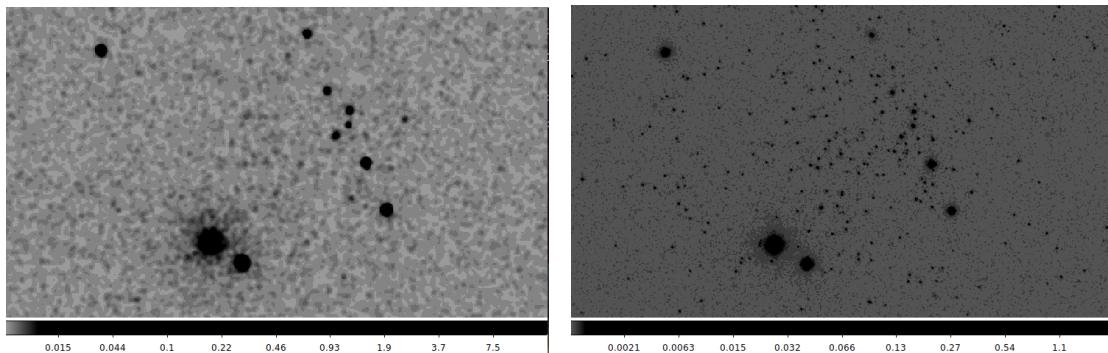
Figure 3.3: Comparison of smoothed GALEX FUV (left) and UVIT F154W (right) filter images.

CMD

We cross-matched the GALEX and UVIT catalogue with the Gaia cluster members catalogue within a cross-correlation radius of 3". A summary of number of sources and cluster members detected in GALEX and UVIT observations is given in Table
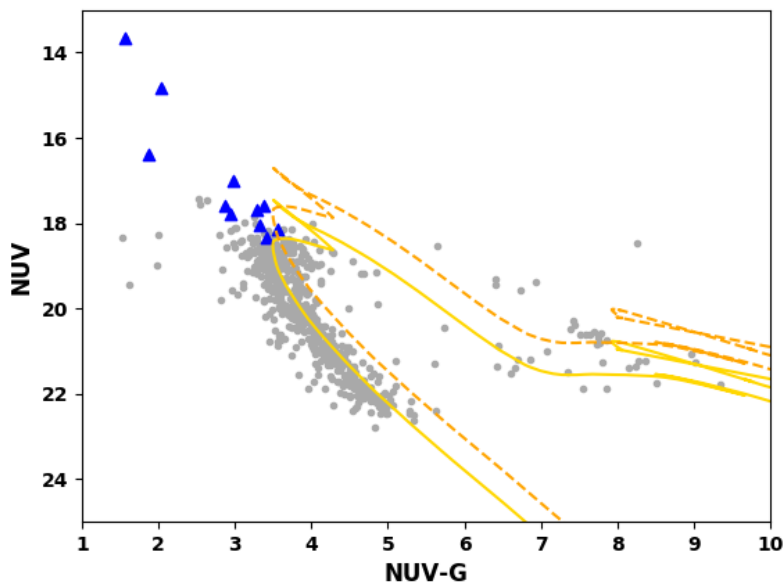
Figure 3.4: NUV CMD of NGC 2506 based on NUV-G magnitude. Best fitting PARSEC isochrones is plotted over the CMD.

3.2. We constructed the NUV and FUV CMD as shown in Fig. 3.4 and 3.5 respectively. It is found that most of the stars shown an excess FUV-NUV color as compared to the best fitting isochrones. It could be due to high chromospheric activity or the presence of hot WD companions. In the NUV-G CMD, few stars deviate from the isochrones indicative of chromospheric activity. A detailed SED analysis can allow us determine the nature of FUV excess.

3.4 Active and eMSTO stars in NGC 6940

NGC 6940 is a nearby ($\sim$1050 pc) intermediate-age OC spread over a diameter $\sim$ 30'. Fig. 3.6 shows the DSS image of NGC 6940 and distribution of cluster members with the XMM field of view (fov) superposed. A preliminary analysis of NGC 6940 using Gaia optical, GALEX NUV, and UVIT FUV (AstroSat) shows the presence of an exotic population of binaries and a prominent eMSTO in the optical and UV CMDs, as shown in Fig. 3.8 and 3.9. The optical and UV CMDs show the presence of a conspicuous binary sequence, several evolved subgiant/red giants, two RS, two BSS and two potential cataclysmic variables (CV) candidates.

Previous X-ray study of NGC 6940 using ROSAT had found the presence of 4 evolved active binaries in the subgiant/red giant phase up to a limiting X-ray luminosity (Lx) $\sim$ 2.2 $\times$ 10^{30} ergs s^{-1} (Belloni & Tagliaferri 1997, A&A, 326, 608B). X-ray luminosity function based upon ROSAT observations of NGC 6940 (see Fig. 3.10), suggests that the active members have unusually high X-ray activity as compared to other clusters of similar age.
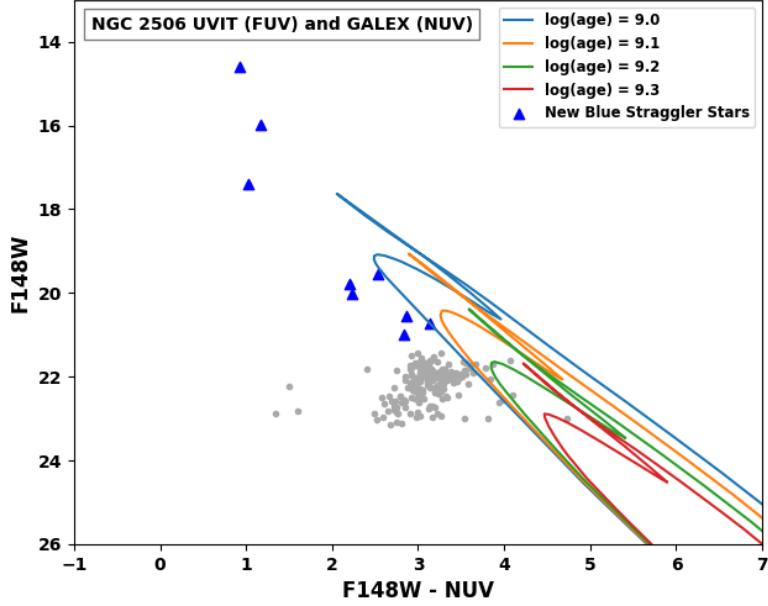
Figure 3.5: FUV CMD of NGC 2506 based on F148W-NUV magnitude. PARSEC isochrones of various ages are plotted over the CMD.

3.4.1 Objectives with XMM-Newton

We have been awarded 100 ksec of XMM-Newton observation time to study the X-ray and UV emission from active stars in the OC NGC 6940. X-ray observations will be carried out using EPIC PN, MOS1 and MOS2 in the full frame mode along with the medium filter. UV observations are planned as multiple 5 ks XMM-OM observations with UVM2, and UVW1 filters in the imaging mode. Multiple filter rotations will be employed to obtain consecutive 5 ks exposures using UVM2 and UVW1 filters. The large field of view of XMM-Newton is best suited to cover ~80% of 567 cluster members (see Fig.3.7), and its spatial resolution of a few arcsec is sufficient to avoid any confusion in this part of the sky based on the flux limit achievable.

The simultaneous X-ray and UV observations will achieve the following objectives :

- Check for X-ray emission from rapidly rotating stars lying along the eMSTO and determine whether the sources are intrinsically spun-up during star formation or present in active binary systems.

- Determine the mechanism of X-ray emission from RS and BSS by fitting various spectral models to the medium-resolution X-ray spectrum obtained from the EPIC PN observations.

- Check for correlation between X-ray-FUV-NUV emission as a function of rotation.
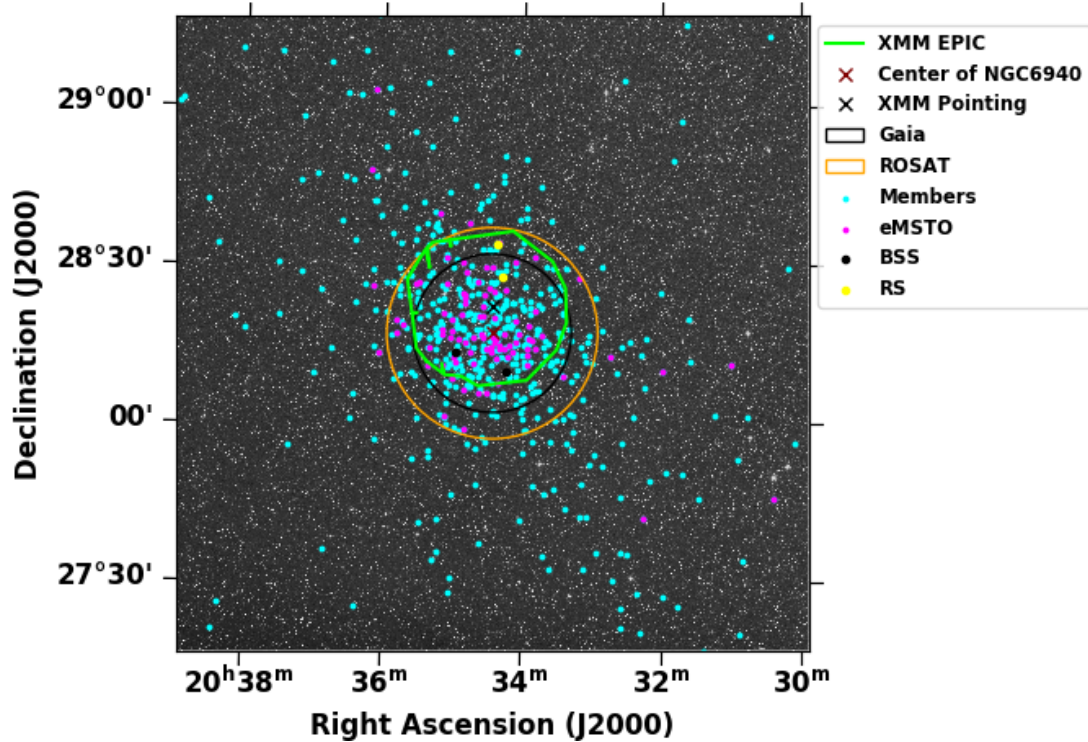
Figure 3.6: Optical image of NGC 6940 from the Digitized Sky Survey (DSS) with the footprint of XMM EPIC (PN, MOS1 and MOS2) filed of view overplotted. The cluster members and the peculiar stars are marked. The crosses indicates the proposed pointing of the XMM EPIC detector and the center of NGC 6940.

- Check for the presence of hot WD companions in RS, fast-rotating stars lying along the MSTO and other active binaries.

- Determine the X-ray luminosity function of active binaries up to a limiting $L_x \sim 7.5 \times 10^{28}$ ergs s^{-1}.

- Correlate the coronal and chromospheric emission from active stars thus detected.

3.4.2 Expected results

In the XMM-Newton EPIC observations, we expect to detect many type of active stars and binaries - BY Dra, CV, BSS, RS, L/HMXB, RS CVn and FK Comae. ROSAT observations of NGC 6940 had detected only 4 active binaries. Based on the X-ray luminosity function we expect to detect at least 20 more active binaries that are cluster members. The deep XMM-Newton observations will allow us to constrain the X-ray luminosity function for active binaries present in NGC 6940 up to a limiting $L_x \sim 10^{29}$ - an order of magnitude deeper than done previously. We expect to detect atleast 3 fast rotating stars like FK Comae as detected in clusters of similar age (NGC 2527; Shah, Singh & Subramaniam 2020). L_X/L_{bol} for intrinsically spun-up fast rotating stars like BY Dra lies in between 10^{-7} to 10^{-3} Singh, et al. (1999). L_{bol} of cluster members with Gmag in the range 17 to
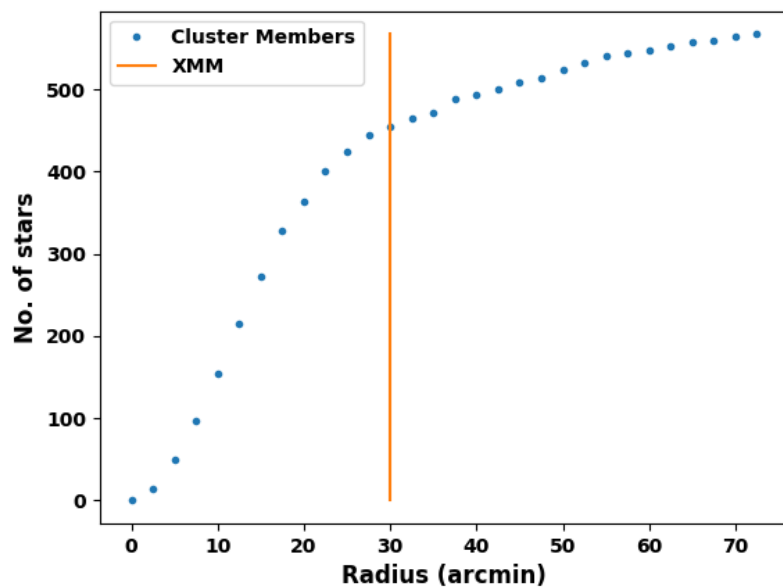
Figure 3.7: Cumulative distribution of the cluster members with radius.
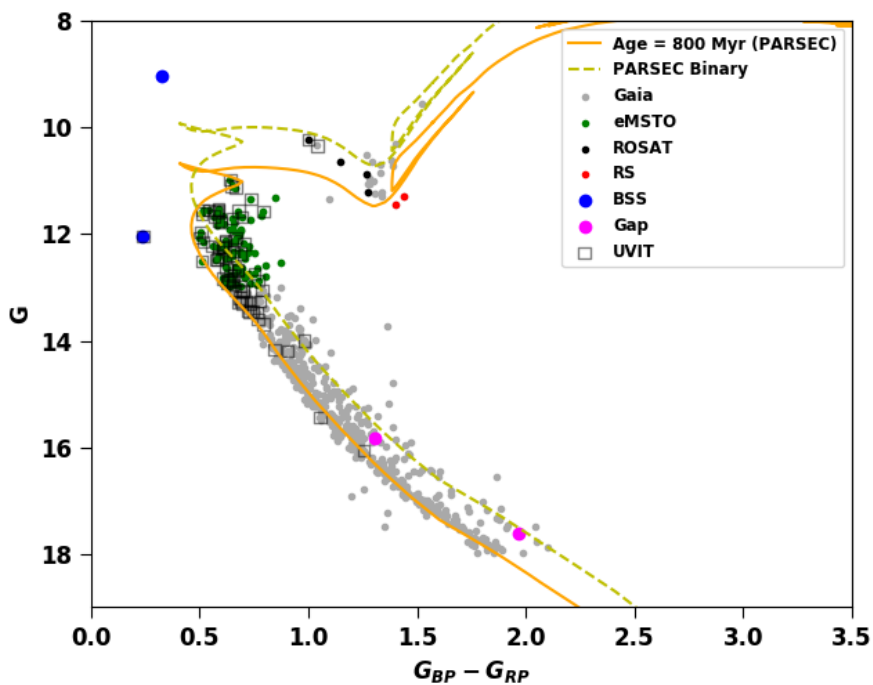
Figure 3.8: Optical CMD of NGC 6940 based on colors from Gaia data. The best fitting PARSEC isochrone along with an equal mass binary isochrone is overlaid.
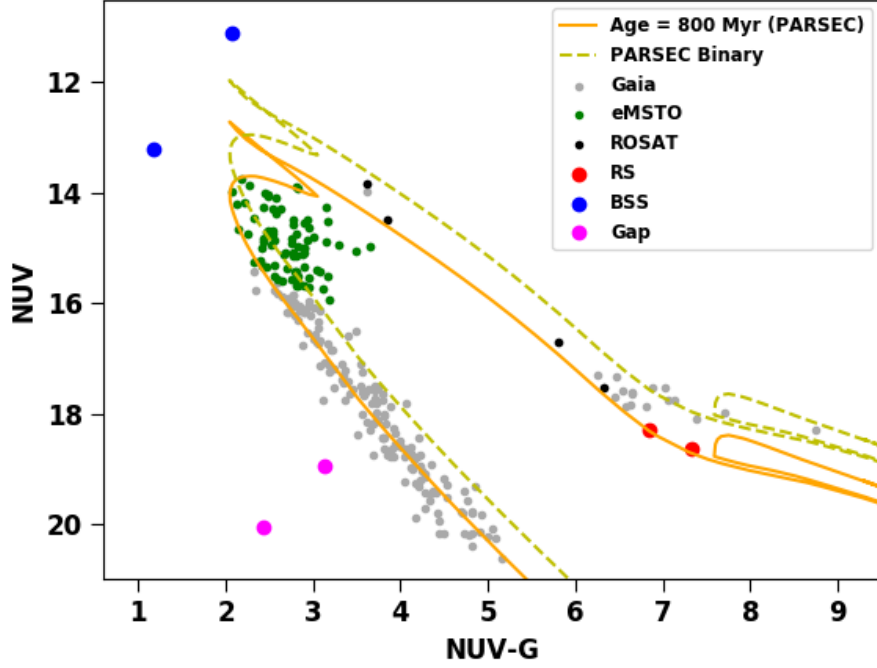
Figure 3.9: UV CMD of NGC 6940 based on NUV GALEX and Gaia Gmag. The best fitting PARSEC isochrone along with the equal mass binary isochrone is overlaid.

9 mag, lies in between 0.1 $L_\odot$ to 200 $L_\odot$. L_X corresponding to an $L_X/L_{bol} \sim 10^{-3}$ lies in between 10^{-4} $L_\odot$ to 0.1 $L_\odot$, which is much lower than limiting value of L_X attained by the proposed XMM-Newton observations, so we are unlikely to detect fast rotating stars like BY Dra. Overall, the detection of X-ray emission from fast rotating stars near the MSTO will allow us to confirm the presence of active binaries in the TO.

We estimate that roughly 100 extragalactic sources will be observed in our observations, by comparing the limiting flux 1.7×10^{-15} ergs cm^{-2} s^{-1} in 0.5-2.0 keV energy band for a 5-sigma detection for a power-law model (index = 2), with the log N-log S distribution derived from the ROSAT deep survey. The X-ray count rates of the detected sources will be divided into three bands: soft (0.3-0.7 keV), medium (0.7-2.0 keV) and hard (2.0-7.0 keV) energy bands, which will be used to construct an X-ray color-color plot as shown in Fig. 3.10 (right). The X-ray color-color plot will allow us to distinguish between the extragalactic sources and the cluster members. X-ray luminosity (Lx) of RS detected in previous studies of GCs is $\sim 3 \times 10^{30}$ ergs s^{-1}. Due to low counts, the previous X-ray studies of GCs could not obtain X-ray spectra. The proposed X-ray observations will allow us to obtain a medium resolution spectral studies of the brightest X-ray sources (very rapidly rotating stars, active binary systems etc.) which will be used to understand the origin of their X-ray emission, specially the RS.
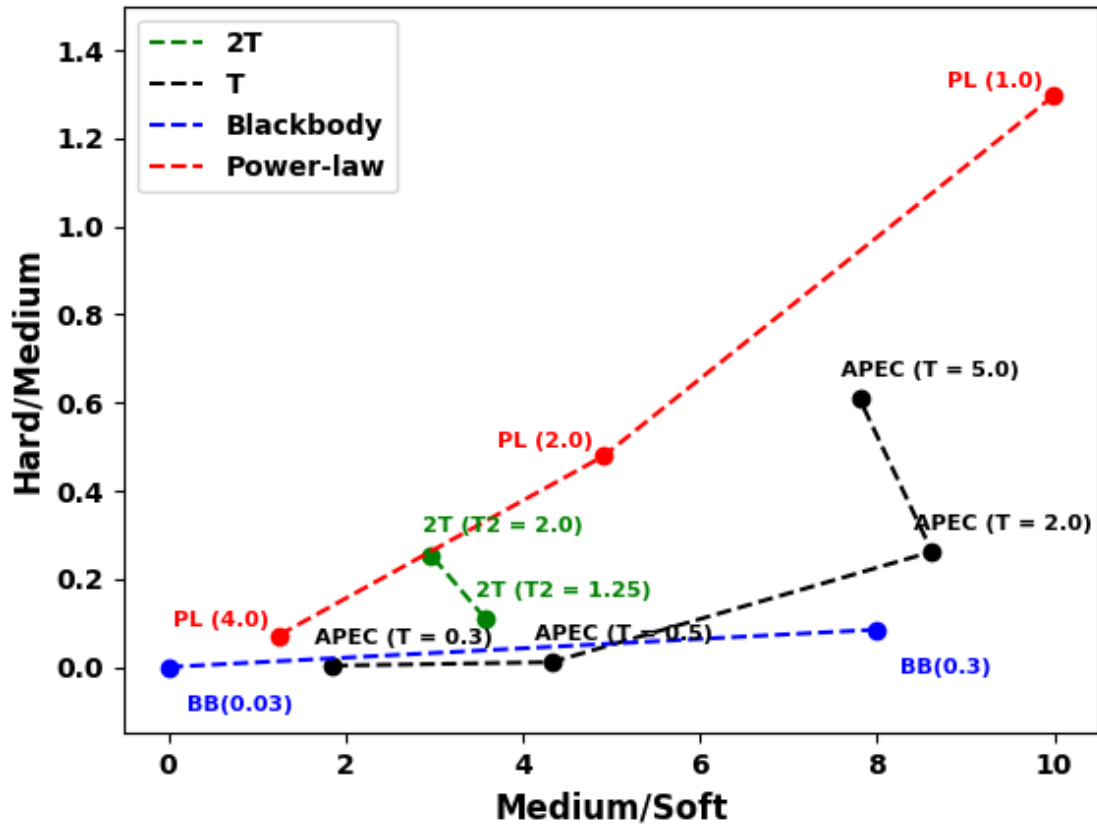
Figure 3.10: X-ray Color-Color plot based on Soft (0.3-0.7 keV), Medium (0.7-2.0 keV), and Hard (2.0-7.0 keV) energy bands. The expected hardness ratios for four kinds of spectra, power law, blackbody (BB), single (T) and two (2T) component collisionally-ionized plasma (APEC) are shown. These were calculated using WebSpec using a fixed Galactic hydrogen column density of 2.6×10^{21} cm^{-2} in that direction.

Bibliography

Althaus L. G., Serenelli A. M., Benvenuto O. G., 2001, MNRAS, 323, 471

Anthony-Twarog B. J., Lee-Brown D. B., Deliyannis C. P., Twarog B. A., 2018, AJ, 155, 138

Arentoft T., et al., 2007, A&A, 465, 965

Arnaud K. A., 1996, ASPC, 17, ASPC..101

Asplund M., Grevesse N., Sauval A. J., Scott P., 2009, ARA&A, 47, 481

Baldwin A. T., Watkins L. L., van der Marel R. P., Bianchini P., Bellini A., Anderson J., 2016, ApJ, 827, 12

Barker H., Paust N. E. Q., 2018, PASP, 130, 034204

Bayo A., Rodrigo C., Barrado Y Navascués D., Solano E., Gutiérrez R., Morales-Calderón M., Allard F., 2008, A&A, 492, 277

Belloni T., Tagliaferri G., 1997, A&A, 326, 608

Belloni T., Verbunt F., Mathieu R. D., 1998, A&A, 339, 431

Berdyugina S. V., 2005, LRSP, 2, 8

Bopp B. W., Stencel R. E., 1981, ApJL, 247, L131

Briggs K. R., Pye J. P., Jeffries R. D., Totten E. J., 2000, MNRAS, 319, 826

Briggs K. R., Pye J. P., 2003, MNRAS, 345, 714

Breeveld A. A., Landsman W., Holland S. T., Roming P., Kuin N. P. M., Page M. J., 2011, AIPC, 373, AIPC.1358

Brown P. J., et al., 2010, ApJ, 721, 1608

Brown W. R., Kilic M., Allende Prieto C., Kenyon S. J., 2010, ApJ, 723, 1072

Brown P. J., Breeveld A., Roming P. W. A., Siegel M., 2016, AJ, 152, 102

Calcaferro L. M., Córsico A. H., Althaus L. G., Romero A. D., Kepler S. O., 2018, A&A, 620, A196

Cantat-Gaudin T., et al., 2018, A&A, 615, A49

Cantat-Gaudin T., et al., 2018, A&A, 618, A93

Carroll, B. W. & Ostlie, D. A. 2007, An Introduction to Modern Astrophysics

Castelli F., Gratton R. G., Kurucz R. L., 1997, A&A, 318, 841

Chavez M., Bertone E., Buzzoni A., et al. 2007, ApJ, 657, 1046

Chen X., Han Z., 2009, MNRAS, 395, 1822

Chiu L.-T. G., van Altena W. F., 1981, ApJ, 243, 827

Conrad C., et al., 2014, A&A, 562, A54

Dias W. S., Alessi B. S., Moitinho A., Lépine J. R. D., 2002, A&A, 389, 871

Dodd R. J., MacGillivray H. T., Hilditch R. W., 1977, MNRAS, 181, 729

Ferraro F. R., et al., 2006, ApJL, 647, L53

Ferraro F. R., Lapenna E., Mucciarelli A., Lanzoni B., Dalessandro E., Pallanca
    C., Massari D., 2016, ApJ, 816, 70

Fitzpatrick E. L., 1999, PASP, 111, 63

Gaia Collaboration, et al., 2016, A&A, 595, A1

Gaia Collaboration, et al., 2018, A&A, 616, A1

Gehrels N., et al., 2004, ApJ, 611, 1005

Geller A. M., et al., 2017, ApJ, 840, 66

Gilliland R. L., Brown T. M., 1992, AJ, 103, 1945

Gilliland R. L., et al., 1998, ApJ, 507, 818

Gondoin P., 2005, A&A, 438, 291

Gosnell N. M., Mathieu R. D., Geller A. M., Sills A., Leigh N., Knigge C., 2014,
    ApJL, 783, L8

Guinan E. F., Engle S. G., 2009, IAUS, 258, 395, IAUS..258

Hasinger G., et al., 1993, A&A, 275, 1

HI4PI Collaboration, et al., 2016, A&A, 594, A116

Hills J. G., Day C. A., 1976, ApL, 17, 87

Howell S. B., Mason E., Boyd P., Smith K. L., Gelino D. M., 2016, ApJ, 831, 27

Indebetouw R., et al., 2005, ApJ, 619, 931

Istrate A. G., Marchant P., Tauris T. M., Langer N., Stancliffe R. J., Grassitelli
    L., 2016, A&A, 595, A35

Jadhav V. V., Sindhu N., Subramaniam A., 2019, ApJ, 886, 13

Jansen F., et al., 2001, A&A, 365, L1

Jeffries R. D., Thurston M. R., Pye J. P., 1997, MNRAS, 287, 350

Knigge C., Zurek D. R., Shara M. M., Long K. S., 2002, ApJ, 579, 752

Lee S. H., Kang Y.-W., Ann H. B., 2012, MNRAS, 425, 1567

Leiner E., Mathieu R. D., Geller A. M., 2017, ApJ, 840, 67

Leiner E., Mathieu R. D., Vanderburg A., Gosnell N. M., Smith J. C., 2019, ApJ, 881, 47

Liebert J., et al., 2004, ApJL, 606, L147

Lindegren L., et al., 2018, A&A, 616, A2

Lindoff U., 1973, A&AS, 9, 229

Marconi G., Hamilton D., Tosi M., Bragaglia A., 1997, MNRAS, 291, 763

Marigo P., et al., 2017, ApJ, 835, 77

Marino A. F., et al., 2018, ApJL, 863, L33

Mason K. O., et al., 2001, A&A, 365, L36

McClure R. D., Twarog B. A., Forrester W. T., 1981, ApJ, 243, 841

McCrea W. H., 1964, MNRAS, 128, 147

Mooley K. P., Singh K. P., 2015, MNRAS, 452, 3394

Pala A. F., et al., 2019, arXiv, arXiv:1907.13152

Pallavicini R., 1989, A&ARv, 1, 177

Panei J. A., Althaus L. G., Chen X., Han Z., 2007, MNRAS, 382, 779

Pérez Martínez M. I., Schröder K.-P., Cuntz M., 2011, MNRAS, 414, 418

Poole T. S., et al., 2008, MNRAS, 383, 627

Postma J. E., Leahy D., 2017, PASP, 129, 115002

Radich S., 1997, MmSAI, 68, 971

Raso S., Ferraro F. R., Dalessandro E., Lanzoni B., Nardiello D., Bellini A., Vesperini E., 2017, ApJ, 839, 64

Reddy A. B. S., Giridhar S., Lambert D. L., 2013, MNRAS, 431, 3338

Reiners A., Giampapa M. S., 2009, ApJ, 707, 852

Rodrigo C., Solano E., Bayo A., 2012, ivoa.rept

Rodríguez-Merino L. H., Chavez M., Bertone E., Buzzoni A., 2005, ApJ, 626, 411

Rodríguez-Merino L. H., Cardona O., Bertone E., Chávez M., Buzzoni A., 2009, ASSP, 7, 239

Roming P. W. A., et al., 2004, X-Ray and Gamma-Ray Instrumentation for Astronomy XIII, 262, SPIE.5165

Rosner R., Tucker W. H., Vaiana G. S., 1978, ApJ, 220, 643

Sahu S., Subramaniam A., Côté P., Rao N. K., Stetson P. B., 2019, MNRAS, 482, 1080

Salpeter E. E., 1955, ApJ, 121, 161

Sandage A., 1957, ApJ, 126, 326

Schrijver C. J., 1995, A&ARv, 6, 181

Shah N., Singh K. P., Subramaniam A., 2020, MNRAS, 493, 5565

Shishkovsky L., et al., 2018, ApJ, 855, 55

Siegel M. H., Hoversten E., Bond H. E., Stark M., Breeveld A. A., 2012, AJ, 144, 65

Siegel M. H., et al., 2014, AJ, 148, 131

Siegel M. H., et al., 2019, AJ, 158, 35

Sindhu N., Subramaniam A., Radha C. A., 2018, MNRAS, 481, 226

Singh K. P., Drake S. A., White N. E., 1996, AJ, 111, 2415

Singh K. P., Drake S. A., Gotthelf E. V., White N. E., 1999, ApJ, 512, 874

Stetson P. B., 1994, PASP, 106, 250

Stetson P. B., 1987, PASP, 99, 191

Strüder L., et al., 2001, A&A, 365, L18

Taylor M., 2011, ascl.soft, ascl:1101.010

Tremblay P.-E., et al., 2017, MNRAS, 465, 2849

Trumpler R. J., 1930, LicOB, 420, 154

Turner M. J. L., et al., 2001, A&A, 365, L27

van den Berg M., Verbunt F., Tagliaferri G., Belloni T., Bedin L. R., Platais I., 2013, ApJ, 770, 98

Vennes S., et al., 2011, ApJL, 737, L16

Webbink R. F., 1976, ApJ, 209, 829

Wu Z.-Y., Zhou X., Ma J., Du C.-H., 2009, MNRAS, 399, 2146

Zhu H., Tian W., Li A., Zhang M., 2017, MNRAS, 471, 3494

Appendices

A   Cross-correlation

To determine the optimal cross-correlation radius in between the soft band X-ray catalogue and the Gaia cluster members catalogue, we followed a technique used by Jeffries, et al. (1997). We generated the cumulative distribution of X-ray sources, $\phi(r)$, for a correlation radius within range 0.1" to 30" with a step of 0.1". We fitted the cumulative distribution function assuming it is formed from the sum of cumulative distribution of the true and spurious correlations as given in Eqn. A.

$$\phi(r) = A[1 - exp(\frac{-r^2}{2\sigma^2})] + (N - A)[1 - exp(-\pi r^2 B)] \qquad \text{(A)}$$

where N is the number of soft band X-ray sources, A is the number of true correlations with the Gaia cluster members catalogue, and B is the number density of objects in the Gaia cluster members catalogue.
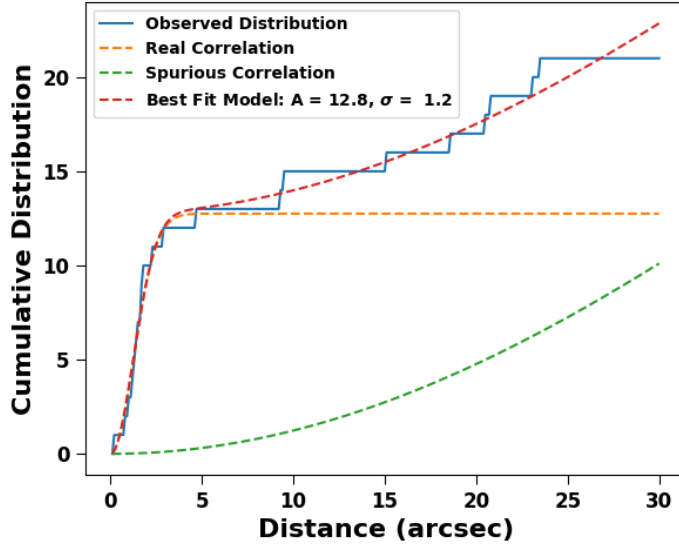
Figure A: Cumulative distribution function of the distances in between the soft band X-ray catalogue and the Gaia cluster members catalogue.

For the soft band X-ray and Gaia cluster members catalogue, we find that the cross-corelation function gives an extremely good fit with parameters A = 12.8,

$\sigma = 1.2$", and B = 7.8×10^{-5} arcsec^{-2} as shown in Fig. A. Using this fit, we choose a maximum cross-correlation radius of 3", within which we should be able to detect approximately 12 true correlations and 0 spurious correlations.

B UVOT Data - background flux

We reprocessed the Swift UVOT observations of NGC 2527 to estimate the background flux limits. The UVOT images and exposure maps of NGC 2527 in each filter were added using HEASOFT image analysis package ximage. We processed the images using 'uvotdetect' task, which detects all the sources in the given image, and provides the background flux or threshold flux. The background flux limits attained in the Swift UVOT observations of NGC 2527 are given in Table 2.7.

C Effect of red leak on the dip feature

To check whether the dip feature could be due to red leak, we corrected the UVOT observed magnitudes of SXOM57 (shows a prominent dip feature) using the red-leak magnitude correction factors for a spectral type F5 V given in Table 12 of Brown, et al. (2010). These red leak corrected magnitudes were converted to fluxes using the conversion factors given in Table 13 of Brown, et al. (2010) and the fluxes were corrected for extinction. We re-estimated the residuals for UVW2 and UVW1 filters using the red-leak and extinction corrected observed fluxes as shown in Fig. B. After correcting the fluxes for red-leak, we observe a more prominent dip feature in the NUV band. Therefore, we conclude that the saddle dip feature is most likely due to inefficient characterization of absorption lines in atmospheric models of cool stars.

Figure B: Red-leak corrected observed SED of a star that shows prominent dip feature. The green stars represent the red-leak corrected observed flux and residual.

D Supplementary Material

Table A: Magnitudes and fluxes of cluster members that are detected in XMM OM and Swift UVOT observations. The units on the XMM OM and Swift UVOT fluxes are 10^{-14} ergs cm^{-2} s^{-1} Å^{-1}.

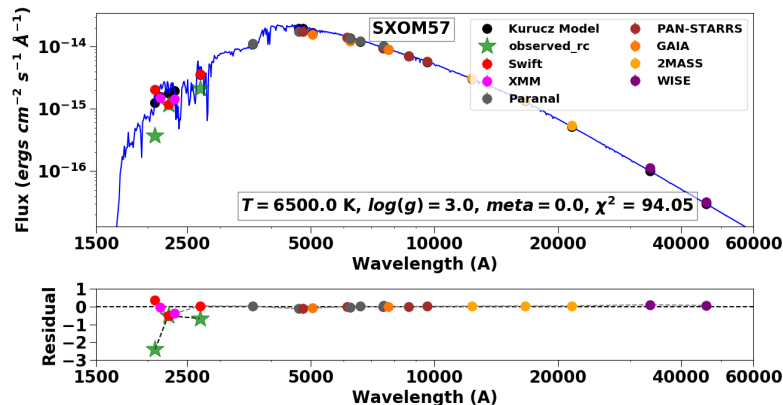| SXOM	UVOT Magnitude			UVOT Flux			OM Flux		OM Quality Flag	
	UVW2 (mag)	UVM2 (mag)	UVW1 (mag)	UVW2	UVM2	UVW1	UVW2	UVM2	UVW2	UVM2
1	13.33±0.02	13.1±0.01	12.53±0.01	7.92±0.15	8.08±0.07	7.93±0.09	-	-	-	-
2	15.35±0.01	15.11±0.01	14.16±0.01	1.23±0.01	1.26±0.01	1.76±0.01	-	-	-	-
3	14.61±0.01	14.34±0.01	13.57±0.01	2.44±0.02	2.56±0.03	3.05±0.04	-	-	-	-
4	17.69±0.02	18.27±0.03	16.23±0.01	0.14±0.0	0.07±0.0	0.26±0.0	0.1±0.01	-	130	-
5	13.37±0.01	13.12±0.02	12.64±0.01	7.64±0.09	7.92±0.11	7.19±0.08	-	-	-	-
6	11.94±0.03	11.85±0.02	11.56±0.03	28.33±0.78	25.54±0.44	19.42±0.5	-	-	-	-
7	15.86±0.01	15.73±0.01	14.58±0.01	0.77±0.01	0.72±0.01	1.2±0.01	0.74±0.02	0.8±0.01	0	128
8	17.97±0.03	18.99±0.05	16.6±0.03	0.11±0.0	0.04±0.0	0.19±0.0	0.06±0.01	0.04±0.0	0	0
9	12.85±0.01	12.71±0.01	12.31±0.02	12.33±0.14	11.48±0.12	9.73±0.16	13.06±0.08	11.13±0.05	0	256
10	16.31±0.05	16.36±0.03	14.96±0.02	0.51±0.02	0.4±0.01	0.85±0.02	-	-	-	-
11	17.69±0.02	18.05±0.03	16.25±0.01	0.14±0.0	0.08±0.0	0.26±0.0	0.11±0.01	0.11±0.01	130	128
12	20.25±0.08	-	18.9±0.05	0.01±0.0	-	0.02±0.0	-	-	-	-
13	-	-	-	-	-	-	0.03±0.01	0.05±0.0	128	128
14	13.4±0.01	13.21±0.01	12.65±0.01	7.42±0.08	7.3±0.06	7.08±0.08	8.01±0.06	7.19±0.04	0	0
15	18.65±0.04	19.51±0.09	17.11±0.04	0.06±0.0	0.02±0.0	0.12±0.0	0.03±0.01	0.03±0.0	0	0
16	17.22±0.03	17.68±0.06	15.78±0.03	0.22±0.01	0.12±0.01	0.4±0.01	0.16±0.02	0.14±0.01	0	0
17	20.74±0.15	21.78±0.49	-	0.01±0.0	0.0±0.0	-	-	-	-	-
18	-	-	-	-	-	-	26.9±0.12	21.79±0.08	256	274
19	-	-	-	-	-	-	56.42±0.14	45.65±0.09	274	274
20	16.42±0.03	16.76±0.04	15.15±0.03	0.46±0.01	0.28±0.01	0.71±0.02	0.32±0.02	0.33±0.01	0	0
21	14.89±0.01	14.68±0.01	13.79±0.01	1.88±0.01	1.88±0.02	2.49±0.02	2.05±0.03	2.02±0.02	0	0
22	15.98±0.01	15.9±0.01	14.68±0.01	0.69±0.01	0.61±0.01	1.1±0.01	0.63±0.02	-	0	-
23	17.18±0.03	17.69±0.05	15.8±0.06	0.23±0.01	0.12±0.01	0.39±0.02	0.15±0.01	0.15±0.01	0	0
24	15.5±0.02	15.35±0.02	14.28±0.02	1.07±0.02	1.02±0.02	1.58±0.02	-	-	-	-
25	18.14±0.03	18.94±0.06	16.8±0.02	0.09±0.0	0.04±0.0	0.16±0.0	-	-	-	-
26	14.21±0.01	13.99±0.02	13.26±0.02	3.52±0.02	3.54±0.05	4.06±0.06	3.98±0.03	3.77±0.03	0	0
27	12.5±0.01	12.34±0.01	12.06±0.03	17.07±0.18	16.21±0.19	12.22±0.32	-	-	-	-
28	-	-	-	-	-	-	117.76±0.31	94.47±0.24	274	274
29	14.09±0.01	13.86±0.01	13.22±0.01	3.94±0.03	4.0±0.03	4.18±0.06	4.21±0.05	-	0	-
30	-	-	-	-	-	-	0.04±0.01	0.03±0.0	0	0
31	14.11±0.01	13.89±0.01	13.14±0.02	3.85±0.04	3.88±0.03	4.52±0.07	4.1±0.05	-	0	-
32	-	-	-	-	-	-	39.59±0.15	32.55±0.09	274	274
33	14.51±0.01	14.35±0.01	13.34±0.02	2.66±0.02	2.54±0.03	3.77±0.05	2.84±0.04	-	0	-
34	15.36±0.01	15.2±0.01	14.07±0.01	1.22±0.01	1.16±0.01	1.92±0.02	1.22±0.03	1.29±0.02	2	2
35	14.55±0.01	14.3±0.01	13.52±0.02	2.57±0.02	2.67±0.03	3.2±0.05	2.85±0.04	-	2	-
36	12.65±0.02	12.49±0.01	12.12±0.02	14.76±0.23	14.12±0.14	11.54±0.26	15.6±0.06	13.57±0.05	0	256
37	13.75±0.01	13.54±0.01	12.97±0.01	5.37±0.05	5.37±0.04	5.3±0.07	5.85±0.02	5.37±0.01	32	288
38	-	-	-	-	-	-	57.43±0.2	-	274	-
39	18.87±0.03	19.89±0.09	17.6±0.02	0.05±0.0	0.02±0.0	0.07±0.0	0.03±0.01	-	2	-
40	13.67±0.01	13.46±0.01	12.9±0.02	5.78±0.06	5.8±0.05	5.65±0.09	6.49±0.06	-	0	-
41	14.49±0.01	14.26±0.02	13.43±0.02	2.73±0.01	2.75±0.05	3.46±0.06	3.11±0.03	2.95±0.02	0	0
42	14.1±0.01	15.74±0.01	12.75±0.02	3.89±0.05	0.71±0.01	6.47±0.14	-	-	-	-
43	13.89±0.01	13.64±0.01	13.06±0.01	4.72±0.03	4.89±0.05	4.89±0.05	5.28±0.05	4.95±0.03	0	0
44	12.5±0.02	12.39±0.02	11.94±0.04	17.06±0.31	15.42±0.34	13.62±0.47	-	-	-	-
45	14.49±0.02	14.33±0.05	-	2.72±0.06	2.6±0.11	-	-	-	-	-
46	-	-	-	-	-	-	0.03±0.01	0.02±0.0	0	0
47	12.26±0.02	12.11±0.01	11.67±0.03	21.26±0.48	20.01±0.27	17.5±0.51	22.01±0.11	18.94±0.06	2	274
48	14.12±0.01	13.85±0.01	13.03±0.02	3.83±0.04	4.03±0.04	4.99±0.1	4.06±0.05	4.12±0.03	128	128
49	20.26±0.07	-	19.32±0.07	0.01±0.0	-	0.02±0.0	-	-	-	-
50	13.06±0.01	12.88±0.02	12.35±0.02	10.11±0.08	9.82±0.17	9.39±0.17	-	-	-	-
51	20.62±0.1	-	19.36±0.05	0.01±0.0	-	0.01±0.0	-	-	-	-
52	19.29±0.08	20.0±0.14	17.72±0.06	0.03±0.0	0.01±0.0	0.07±0.0	-	0.02±0.0	-	0
53	16.0±0.01	15.88±0.01	14.68±0.01	0.67±0.01	0.62±0.01	1.1±0.01	0.67±0.02	-	0	-
54	13.46±0.01	13.27±0.01	12.76±0.01	7.05±0.06	6.87±0.07	6.43±0.09	7.54±0.06	6.6±0.04	0	0
55	18.75±0.06	19.36±0.1	-	0.05±0.0	0.03±0.0	-	0.04±0.01	0.03±0.0	2	2
56	18.31±0.04	18.5±0.05	17.1±0.04	0.08±0.0	0.06±0.0	0.12±0.0	0.05±0.01	0.06±0.0	128	0
57	17.31±0.01	17.69±0.03	15.87±0.01	0.2±0.0	0.12±0.0	0.37±0.0	0.15±0.01	0.14±0.01	0	0
58	19.38±0.05	20.59±0.15	18.01±0.03	0.03±0.0	0.01±0.0	0.05±0.0	-	-	-	-
59	16.74±0.01	16.85±0.01	15.31±0.01	0.34±0.0	0.26±0.0	0.61±0.01	0.26±0.02	-	0	-
60	13.41±0.01	13.28±0.01	12.71±0.02	7.36±0.08	6.8±0.05	6.73±0.13	7.7±0.06	6.58±0.04	34	34
61	14.08±0.02	15.5±0.01	12.74±0.02	3.97±0.09	0.89±0.01	6.51±0.13	1.8±0.01	1.2±0.01	33	33
62	17.74±0.02	18.21±0.03	16.3±0.01	0.14±0.0	0.07±0.0	0.25±0.0	0.07±0.01	-	0	-

Table B: Extinction corrected fluxes obtained from VO photometry. The units on APASS, PAN-STARRS, and Gaia fluxes are 10^{-14} ergs s^{-1} cm^{-2} Å^{-1}.

| SXOM | APASS | | PAN-STARRS | | | | | Gaia | | |
	B	V	g	r	z	y	i	Gbp	G	Grp
1	21.59±0.54	15.85±0.16	-	-	-	-	-	15.67±0.16	10.78±0.11	6.73±0.07
2	6.23±0.2	5.02±0.05	-	-	-	1.32±0.0	-	4.57±0.05	3.28±0.03	2.21±0.02
3	9.24±0.05	7.11±0.11	-	-	-	1.85±0.0	-	6.97±0.07	4.86±0.05	3.15±0.03
4	1.4±0.07	1.36±0.05	1.44±0.01	1.16±0.0	0.59±0.0	0.48±0.0	0.79±0.01	1.28±0.01	1.02±0.01	0.76±0.01
5	19.3±0.43	13.23±0.15	-	-	-	-	-	13.43±0.13	8.89±0.09	5.33±0.05
6	43.16±0.6	27.16±0.6	-	-	-	-	-	27.97±0.28	17.77±0.18	9.89±0.1
7	4.2±0.04	3.5±0.03	-	-	-	1.09±0.0	-	3.55±0.04	2.59±0.03	1.78±0.02
8	1.48±0.05	1.6±0.02	1.67±0.01	1.47±0.03	0.78±0.01	0.66±0.0	1.02±0.0	1.46±0.01	1.23±0.01	0.97±0.01
9	24.11±0.82	16.22±0.27	-	-	-	-	-	16.78±0.17	10.96±0.11	6.38±0.06
10	3.49±0.09	3.02±0.08	-	-	-	0.95±0.0	-	2.83±0.03	2.13±0.02	1.52±0.02
11	1.35±0.06	1.3±0.03	1.4±0.0	1.12±0.0	0.58±0.0	0.47±0.0	0.82±0.0	1.24±0.01	0.99±0.01	0.74±0.01
12	-	-	0.29±0.0	0.32±0.0	0.2±0.0	0.17±0.0	0.25±0.0	0.28±0.0	0.27±0.0	0.24±0.0
13	0.97±0.05	1.02±0.03	1.07±0.0	0.88±0.0	0.46±0.0	0.39±0.0	0.63±0.0	0.93±0.01	0.76±0.01	0.59±0.01
14	20.13±0.74	14.14±0.21	-	-	-	-	-	14.43±0.14	9.67±0.1	5.88±0.06
15	0.71±0.04	0.92±0.01	0.85±0.0	0.74±0.0	0.4±0.0	0.33±0.0	0.54±0.0	0.75±0.01	0.63±0.01	0.5±0.0
16	2.32±0.09	2.32±0.07	2.53±0.0	-	1.07±0.0	0.87±0.0	-	2.23±0.02	1.79±0.02	1.36±0.01
17	-	-	0.06±0.0	0.08±0.0	-	-	0.12±0.01	0.11±0.0	0.1±0.0	0.16±0.0
18	43.12±1.15	26.91±0.57	26.96±1.17	-	0.32±0.0	0.94±0.0	1.84±0.11	27.5±0.27	17.3±0.17	9.42±0.09
19	84.0±2.32	49.51±1.5	-	-	-	-	-	52.47±0.52	32.53±0.33	17.21±0.17
20	3.42±0.11	3.21±0.03	3.5±0.0	-	-	1.09±0.0	-	3.01±0.03	2.34±0.02	1.71±0.02
21	7.67±0.23	5.99±0.08	-	-	-	1.63±0.0	-	5.94±0.06	4.19±0.04	2.75±0.03
22	4.21±0.04	3.54±0.02	-	-	-	1.04±0.0	-	3.39±0.03	2.49±0.02	1.72±0.02
23	2.02±0.04	1.78±0.02	2.37±0.0	-	1.08±0.0	0.9±0.0	-	2.09±0.02	1.71±0.02	1.33±0.01
24	-	-	-	-	-	1.48±0.0	-	4.7±0.05	3.47±0.03	2.41±0.02
25	1.07±0.01	1.09±0.02	1.15±0.0	0.95±0.0	0.49±0.0	0.41±0.0	0.67±0.0	0.98±0.01	0.8±0.01	0.61±0.01
26	12.03±0.21	8.89±0.11	-	-	-	2.26±0.0	-	8.86±0.09	6.09±0.06	3.87±0.04
27	30.72±0.62	19.88±0.51	-	-	-	-	-	20.5±0.21	13.25±0.13	7.52±0.08
28	106.04±1.06	-	-	-	-	-	-	95.85±0.96	59.49±0.59	31.54±0.32
29	-	-	-	-	-	2.18±0.01	-	8.8±0.09	6.01±0.06	3.79±0.04
30	0.8±0.01	0.95±0.01	0.85±0.0	0.74±0.0	0.4±0.0	0.33±0.0	0.54±0.0	0.76±0.01	0.63±0.01	0.5±0.0
31	14.81±0.37	11.37±0.27	-	-	-	-	-	10.82±0.11	7.63±0.08	4.99±0.05
32	79.48±2.64	50.2±2.31	-	-	-	-	-	51.89±0.52	33.26±0.33	18.48±0.18
33	12.73±0.28	10.0±0.1	-	-	-	-	-	9.68±0.1	6.93±0.07	4.62±0.05
34	6.95±0.15	5.89±0.04	-	-	-	1.75±0.0	-	5.64±0.06	4.17±0.04	2.88±0.03
35	10.02±0.24	7.56±0.1	-	-	-	2.0±0.01	-	7.5±0.08	5.24±0.05	3.4±0.03
36	31.18±0.8	20.41±0.45	-	-	-	-	-	20.91±0.21	13.65±0.14	7.9±0.08
37	14.65±0.49	10.47±0.23	-	-	-	-	-	10.55±0.11	7.13±0.07	4.42±0.04
38	110.63±16.51	80.82±0.74	-	-	-	-	-	82.84±0.83	53.44±0.53	30.2±0.3
39	-	-	0.65±0.0	0.6±0.0	0.33±0.0	0.27±0.0	0.43±0.0	0.59±0.01	0.5±0.01	0.4±0.0
40	16.27±0.24	11.54±0.2	-	-	-	-	-	11.54±0.12	7.77±0.08	4.79±0.05
41	10.33±0.22	7.78±0.06	-	-	-	2.03±0.0	-	7.7±0.08	5.37±0.05	3.47±0.03
42	67.65±1.87	87.16±2.09	-	-	-	-	-	75.95±0.76	68.91±0.69	57.19±0.57
43	12.9±0.46	9.32±0.26	-	-	-	-	-	9.4±0.09	6.37±0.06	3.97±0.04
44	39.61±0.91	25.56±0.24	-	-	-	-	-	26.08±0.26	16.64±0.17	9.23±0.09
45	9.7±0.18	7.35±0.14	-	-	-	1.93±0.0	-	7.33±0.07	5.1±0.05	3.29±0.03
46	-	-	0.1±0.0	0.15±0.0	0.11±0.0	0.1±0.0	0.13±0.0	0.12±0.0	0.12±0.0	0.13±0.0
47	50.89±1.92	33.66±0.74	-	-	-	-	-	34.35±0.34	22.52±0.23	13.16±0.13
48	15.27±0.14	12.22±0.42	-	-	-	-	-	11.96±0.12	8.46±0.08	5.54±0.06
49	-	-	0.2±0.0	0.23±0.0	0.15±0.0	0.13±0.0	0.2±0.0	0.2±0.0	0.2±0.0	0.18±0.0
50	26.25±0.58	18.36±0.19	-	-	-	-	-	18.54±0.19	12.56±0.13	7.68±0.08
51	0.18±0.01	0.31±0.03	0.23±0.0	0.26±0.0	0.17±0.0	0.14±0.0	0.21±0.0	0.22±0.0	0.22±0.0	0.2±0.0
52	-	-	0.66±0.0	0.6±0.0	0.33±0.0	0.27±0.0	0.44±0.0	0.6±0.01	0.51±0.01	0.41±0.0
53	3.99±0.15	3.36±0.02	3.72±0.1	-	-	1.0±0.0	-	3.25±0.03	2.39±0.02	1.65±0.02
54	17.94±0.61	12.74±0.27	-	-	-	-	-	13.02±0.13	8.81±0.09	5.43±0.05
55	0.82±0.06	0.98±0.1	0.88±0.0	0.75±0.0	0.41±0.0	0.34±0.0	0.55±0.0	0.78±0.01	0.65±0.01	0.51±0.01
56	0.84±0.05	0.89±0.02	0.43±0.0	0.42±0.0	0.24±0.0	0.21±0.0	0.31±0.0	0.39±0.0	0.35±0.0	0.29±0.0
57	1.68±0.05	1.64±0.02	1.74±0.04	1.42±0.0	0.7±0.0	0.58±0.0	0.95±0.01	1.57±0.02	1.22±0.0	0.9±0.01
58	0.43±0.07	0.54±0.01	0.52±0.0	0.51±0.0	0.29±0.0	0.24±0.0	0.38±0.0	0.49±0.0	0.43±0.0	0.36±0.0
59	2.63±0.08	2.35±0.03	2.55±0.0	-	0.93±0.0	0.75±0.0	-	2.24±0.02	1.7±0.02	1.21±0.01
60	21.02±0.64	14.51±0.21	-	-	-	-	-	14.75±0.15	9.77±0.1	5.82±0.06
61	64.96±0.78	83.78±1.77	-	-	-	-	-	72.82±0.73	66.01±0.66	54.49±0.54
62	1.37±0.09	1.41±0.05	1.42±0.0	1.14±0.0	0.58±0.0	0.47±0.0	0.8±0.0	1.24±0.01	0.99±0.01	0.74±0.01

Table C: The units on Paranal, 2MASS and WISE fluxes are 10^{-14}, 10^{-15} and 10^{-17} ergs s^{-1} cm^{-2} Å^{-1} respectively.

SXOM	Paranal/OmegaCAM					2MASS			WISE	
	u	Halpha	g	r	i	J	H	Ks	W1	W2
1	13.78±0.14	9.84±0.1	-	-	-	1.97±0.04	0.78±0.02	0.31±0.01	0.06±0.0	0.02±0.0
2	4.2±0.04	3.11±0.03	5.58±0.06	3.38±0.03	2.5±0.03	0.69±0.02	0.28±0.01	0.11±0.0	0.02±0.0	0.01±0.0
3	6.3±0.06	4.54±0.05	-	-	3.45±0.03	0.96±0.02	0.38±0.01	0.15±0.0	0.03±0.0	0.01±0.0
4	0.85±0.01	1.03±0.01	1.44±0.01	1.13±0.01	0.85±0.01	0.27±0.01	0.12±0.0	0.05±0.0	0.01±0.0	0.0±0.0
5	11.9±0.12	7.67±0.08	-	-	-	1.5±0.03	0.57±0.01	0.22±0.0	0.04±0.0	0.01±0.0
6	-	14.62±0.15	-	-	-	2.68±0.06	0.92±0.02	0.37±0.01	0.07±0.0	0.02±0.0
7	3.1±0.03	2.49±0.02	4.2±0.04	2.66±0.03	1.99±0.02	0.57±0.02	0.24±0.01	0.09±0.0	0.02±0.0	0.01±0.0
8	0.77±0.01	1.31±0.01	1.62±0.02	1.32±0.01	1.08±0.01	0.38±0.01	0.18±0.0	0.07±0.0	0.01±0.0	0.0±0.0
9	14.3±0.14	9.31±0.09	-	-	-	1.75±0.04	0.66±0.01	0.25±0.0	0.05±0.0	0.01±0.0
10	2.33±0.02	2.15±0.02	3.18±0.03	2.31±0.02	1.71±0.02	0.53±0.01	0.23±0.01	0.09±0.0	0.02±0.0	0.0±0.0
11	0.85±0.01	1.0±0.01	1.43±0.01	1.09±0.01	0.83±0.01	0.27±0.01	0.12±0.0	0.05±0.0	0.01±0.0	0.0±0.0
12	0.08±0.0	0.32±0.0	0.26±0.0	0.31±0.0	0.26±0.0	0.05±0.0	0.03±0.0	0.01±0.0	0.01±0.0	0.0±0.0
13	0.54±0.01	0.79±0.01	1.03±0.01	0.83±0.01	0.66±0.01	0.22±0.0	0.1±0.0	0.04±0.0	0.01±0.0	0.0±0.0
14	12.46±0.12	8.34±0.08	-	-	-	1.66±0.04	0.64±0.01	0.24±0.0	0.05±0.0	0.01±0.0
15	0.4±0.0	-	0.81±0.01	0.73±0.01	0.54±0.01	0.19±0.0	0.09±0.0	0.04±0.0	0.01±0.0	0.0±0.0
16	1.39±0.01	-	2.41±0.02	1.98±0.02	1.45±0.01	0.5±0.01	0.23±0.0	0.09±0.0	0.02±0.0	0.0±0.0
17	0.03±0.0	0.62±0.01	0.28±0.0	0.56±0.01	0.71±0.01	0.69±0.02	0.5±0.01	0.23±0.01	0.05±0.0	0.01±0.0
18	23.95±0.24	13.71±0.14	-	-	-	2.43±0.05	0.87±0.02	0.34±0.01	0.07±0.0	0.02±0.0
19	-	-	-	-	-	4.34±0.1	1.5±0.03	0.56±0.01	0.11±0.0	0.03±0.0
20	2.16±0.02	-	3.33±0.03	2.57±0.03	1.86±0.02	0.62±0.01	0.27±0.01	0.11±0.0	0.02±0.0	0.01±0.0
21	5.34±0.05	-	6.96±0.07	4.62±0.05	3.01±0.03	0.85±0.02	0.34±0.01	0.13±0.0	0.03±0.0	0.01±0.0
22	2.91±0.03	2.38±0.02	4.01±0.04	2.54±0.03	1.93±0.02	0.54±0.01	0.23±0.01	0.09±0.0	0.02±0.0	0.0±0.0
23	1.33±0.01	1.71±0.02	2.33±0.02	1.88±0.02	1.51±0.02	0.51±0.01	0.25±0.01	0.1±0.0	0.02±0.0	0.01±0.0
24	3.87±0.04	3.35±0.03	5.53±0.06	3.75±0.04	2.69±0.03	0.79±0.02	0.34±0.01	0.13±0.0	0.03±0.0	0.01±0.0
25	0.6±0.01	0.83±0.01	1.09±0.01	0.86±0.01	0.68±0.01	0.23±0.01	0.11±0.0	0.04±0.0	0.01±0.0	0.0±0.0
26	7.93±0.08	5.46±0.05	-	6.2±0.06	-	1.12±0.03	0.44±0.01	0.17±0.0	0.03±0.0	0.01±0.0
27	-	10.79±0.11	-	-	-	2.01±0.05	0.75±0.02	0.29±0.01	0.06±0.0	0.02±0.0
28	-	-	-	-	-	7.48±0.2	2.81±0.07	1.08±0.02	0.22±0.0	0.06±0.0
29	7.93±0.08	5.46±0.05	-	-	-	1.1±0.03	0.43±0.01	0.16±0.0	0.03±0.0	0.01±0.0
30	-	-	-	0.74±0.01	-	0.19±0.0	0.09±0.0	0.04±0.0	0.01±0.0	0.0±0.0
31	9.8±0.1	7.0±0.07	-	-	-	1.53±0.04	0.63±0.02	0.23±0.01	0.05±0.0	0.01±0.0
32	-	-	-	-	-	4.83±0.12	1.7±0.04	0.66±0.01	0.13±0.0	0.04±0.0
33	8.62±0.09	6.56±0.07	-	-	-	1.43±0.03	0.58±0.01	0.23±0.0	0.04±0.0	0.01±0.0
34	4.82±0.05	3.99±0.04	6.59±0.07	4.47±0.04	3.36±0.03	0.94±0.02	0.4±0.01	0.16±0.0	0.03±0.0	0.01±0.0
35	6.78±0.07	4.8±0.05	-	5.5±0.06	-	1.0±0.02	0.4±0.01	0.16±0.0	0.03±0.0	0.01±0.0
36	-	11.51±0.12	-	-	-	2.14±0.05	0.8±0.02	0.3±0.01	0.06±0.0	0.02±0.0
37	9.36±0.09	6.5±0.07	-	-	-	1.28±0.03	0.49±0.01	0.19±0.0	0.04±0.0	0.01±0.0
38	-	-	-	-	-	7.83±0.17	2.93±0.06	1.11±0.02	0.22±0.0	0.06±0.0
39	0.28±0.0	-	0.61±0.01	0.56±0.01	-	0.15±0.0	0.08±0.0	0.03±0.0	0.01±0.0	0.0±0.0
40	9.99±0.1	6.93±0.07	-	-	-	1.33±0.03	0.53±0.01	0.2±0.0	0.04±0.0	0.01±0.0
41	6.91±0.07	-	-	-	3.82±0.04	1.03±0.02	0.4±0.01	0.16±0.0	0.03±0.0	0.01±0.0
42	-	-	-	-	-	24.5±0.54	12.87±0.37	5.4±0.13	1.13±0.05	0.29±0.01
43	8.7±0.09	-	-	-	-	1.12±0.03	0.45±0.01	0.17±0.0	0.03±0.0	0.01±0.0
44	-	13.84±0.14	-	-	-	2.32±0.06	0.81±0.02	0.32±0.01	0.06±0.0	0.02±0.0
45	6.6±0.07	-	-	-	3.65±0.04	0.98±0.02	0.4±0.01	0.15±0.0	0.03±0.0	0.01±0.0
46	0.02±0.0	0.14±0.0	0.1±0.0	0.14±0.0	0.14±0.0	0.07±0.0	0.04±0.0	0.02±0.0	0.0±0.0	0.0±0.0
47	-	-	-	-	-	3.67±0.08	1.36±0.03	0.54±0.01	0.1±0.0	0.03±0.0
48	10.75±0.11	-	-	-	-	1.72±0.04	0.69±0.02	0.26±0.0	0.05±0.0	0.01±0.0
49	0.05±0.0	0.23±0.0	0.18±0.0	0.23±0.0	0.2±0.0	0.09±0.0	0.05±0.0	0.02±0.0	0.0±0.0	0.0±0.0
50	15.83±0.16	-	-	-	-	2.23±0.05	0.89±0.02	0.33±0.01	0.06±0.0	0.02±0.0
51	0.05±0.0	0.25±0.0	0.2±0.0	0.25±0.0	0.21±0.0	0.09±0.0	0.05±0.0	0.02±0.0	0.0±0.0	0.0±0.0
52	0.27±0.0	-	0.61±0.01	0.59±0.01	0.45±0.0	0.17±0.0	0.08±0.0	0.03±0.0	0.01±0.0	0.0±0.0
53	2.8±0.03	2.38±0.02	3.76±0.04	2.66±0.03	1.83±0.02	0.55±0.01	0.23±0.0	0.09±0.0	0.02±0.0	0.0±0.0
54	11.05±0.11	7.6±0.08	-	-	-	1.57±0.04	0.63±0.01	0.25±0.0	0.05±0.0	0.01±0.0
55	0.42±0.0	0.66±0.01	0.84±0.01	0.72±0.01	0.57±0.01	0.2±0.01	0.09±0.0	0.04±0.0	0.01±0.0	0.0±0.0
56	-	-	-	0.41±0.0	0.32±0.0	0.13±0.01	0.1±0.0	0.04±0.0	0.01±0.0	0.0±0.0
57	1.13±0.01	1.23±0.01	1.77±0.02	1.33±0.01	1.03±0.01	0.31±0.01	0.14±0.0	0.05±0.0	0.01±0.0	0.0±0.0
58	0.2±0.0	0.47±0.0	0.49±0.0	0.49±0.0	0.39±0.0	0.14±0.0	0.07±0.0	0.03±0.0	0.01±0.0	0.0±0.0
59	1.83±0.02	1.66±0.02	2.67±0.03	1.74±0.02	1.36±0.01	0.41±0.01	0.18±0.0	0.07±0.0	0.01±0.0	0.0±0.0
60	12.12±0.12	8.57±0.09	-	-	-	1.63±0.03	0.6±0.01	0.24±0.0	0.04±0.0	0.01±0.0
61	25.55±0.26	-	-	-	-	24.14±0.6	12.2±0.52	5.31±0.15	1.1±0.04	0.28±0.0
62	0.82±0.01	1.04±0.01	1.35±0.01	1.12±0.01	0.81±0.01	0.27±0.01	0.13±0.0	0.05±0.0	0.01±0.0	0.0±0.0

Table D: Properties of peculiar stars that deviate from standard evolutionary models in the optical CMD. Column 1, 2, 3, 6 & 7 list the RA, Dec, distance, radial velocity from Gaia DR2, and membership probability of stars, columns 4 & 5, give the G mag and the G_{BP}-G_{RP} colour taken from Gaia DR2 catalogue, and column 8 gives the type of stars depending upon their position in the optical CMD.

RA	Dec	Dist	Gmag	BP-RP	RV	PMemb	Type
(^{h} ′ ″)	(° ′ ″)	(pc)	(mag)	(mag)	(km/s)		
8:03:22	-28:26:43	656.0 ± 16.9	9.65	0.48	-	0.9	SSG[1]
8:04:33	-27:47:13	711.3 ± 19.0	10.06	0.38	-	1.0	SSG
8:05:09	-27:56:50	665.8 ± 16.1	10.06	0.4	-	1.0	SSG
8:04:57	-28:08:46	640.1 ± 13.6	10.09	0.32	-	1.0	SSG
8:03:46	-26:58:56	672.5 ± 65.8	17.04	1.25	-	0.6	Gap[2]
7:58:13	-27:41:5	733.3 ± 56.2	15.67	0.96	-	0.6	Gap
8:03:42	-29:21:39	604.2 ± 31.4	16.02	1.02	-	0.6	Gap
8:06:23	-28:42:31	737.7 ± 93.8	17.91	1.33	-	0.6	Gap
8:07:46	-28:29:59	628.7 ± 21.8	16.41	1.67	-	1.0	Gap
7:59:46	-27:06:30	682.7 ± 14.6	9.73	1.64	90 ± 1	0.9	RS[3]

SSG : Sub-subgiant
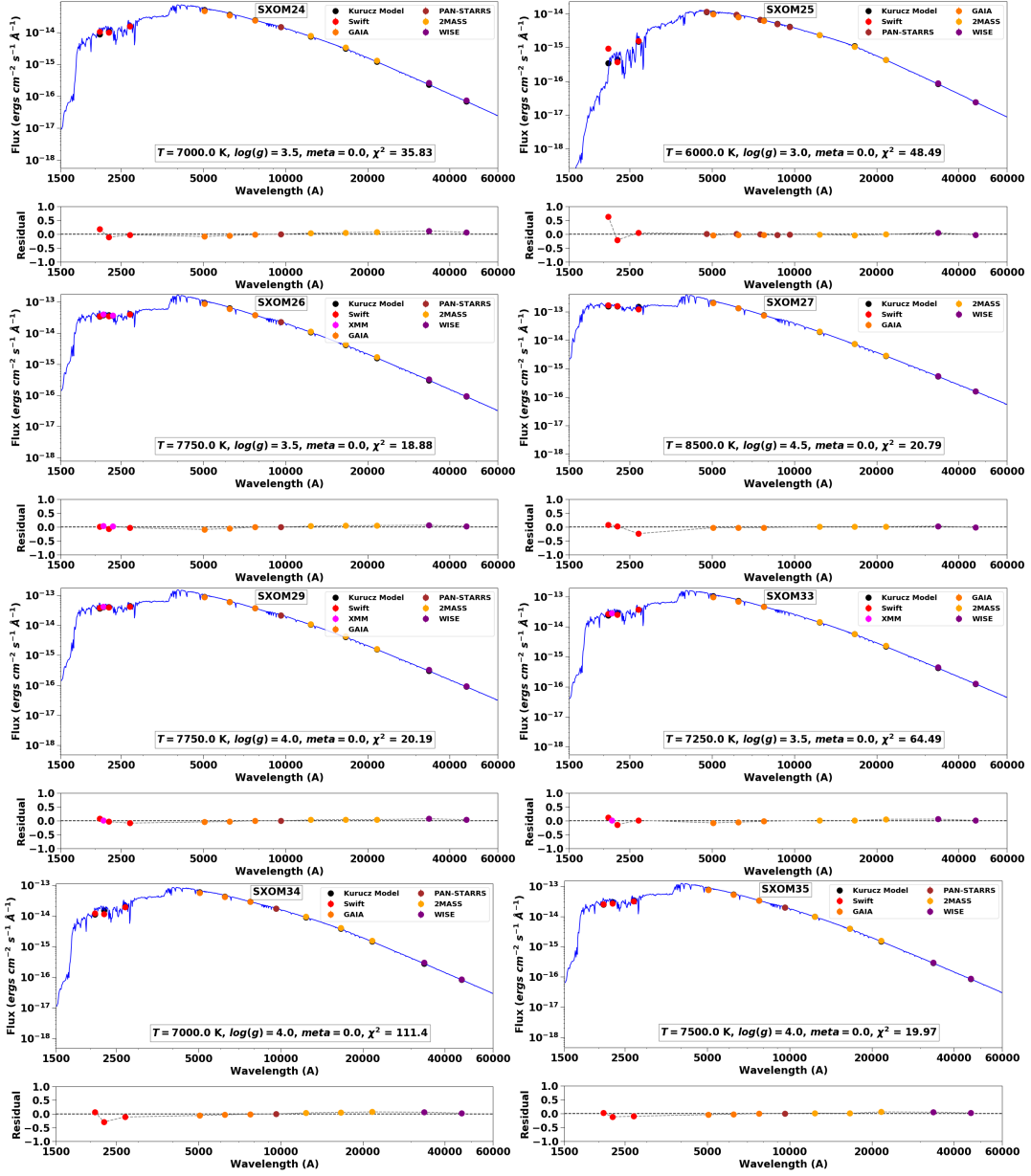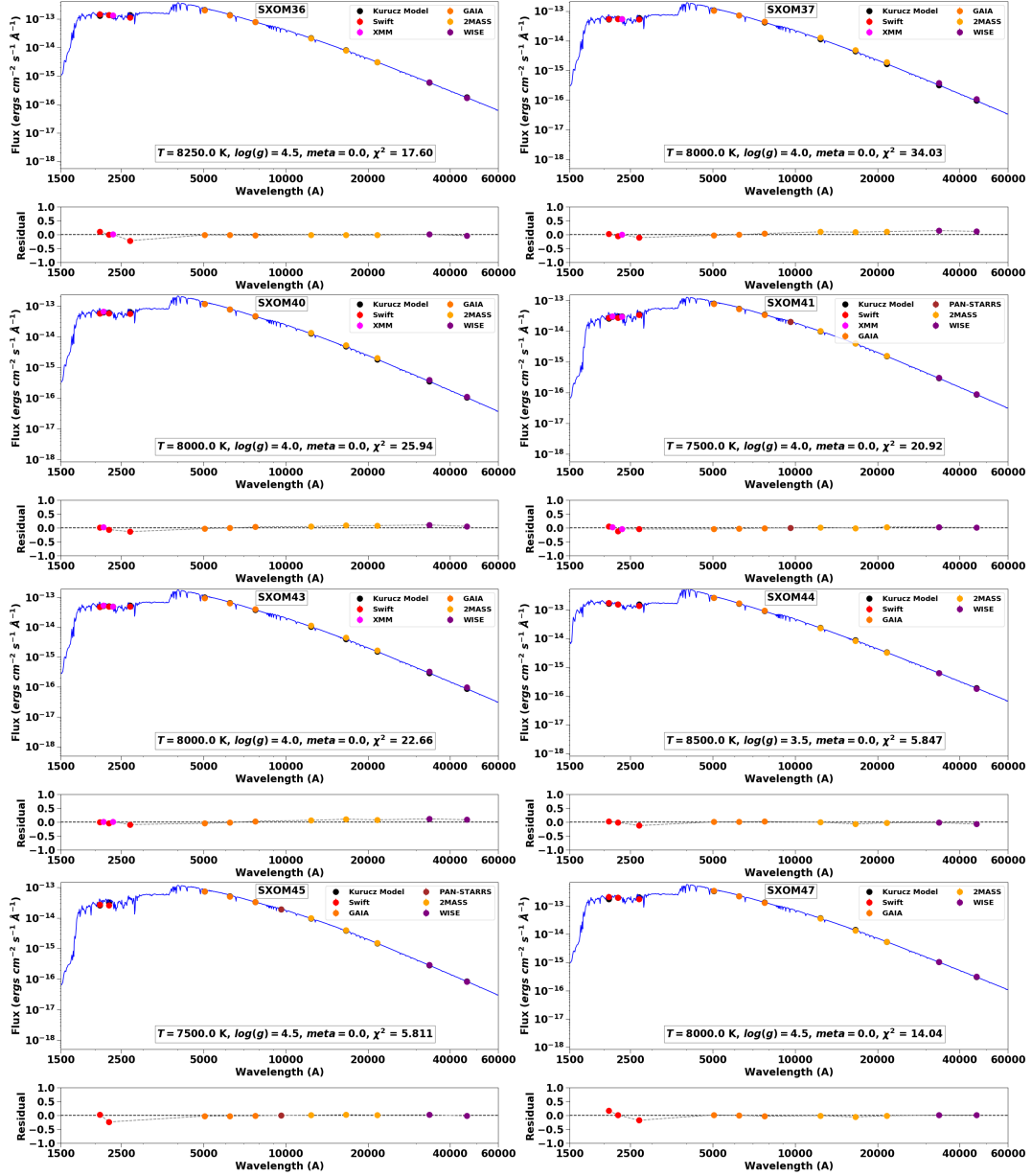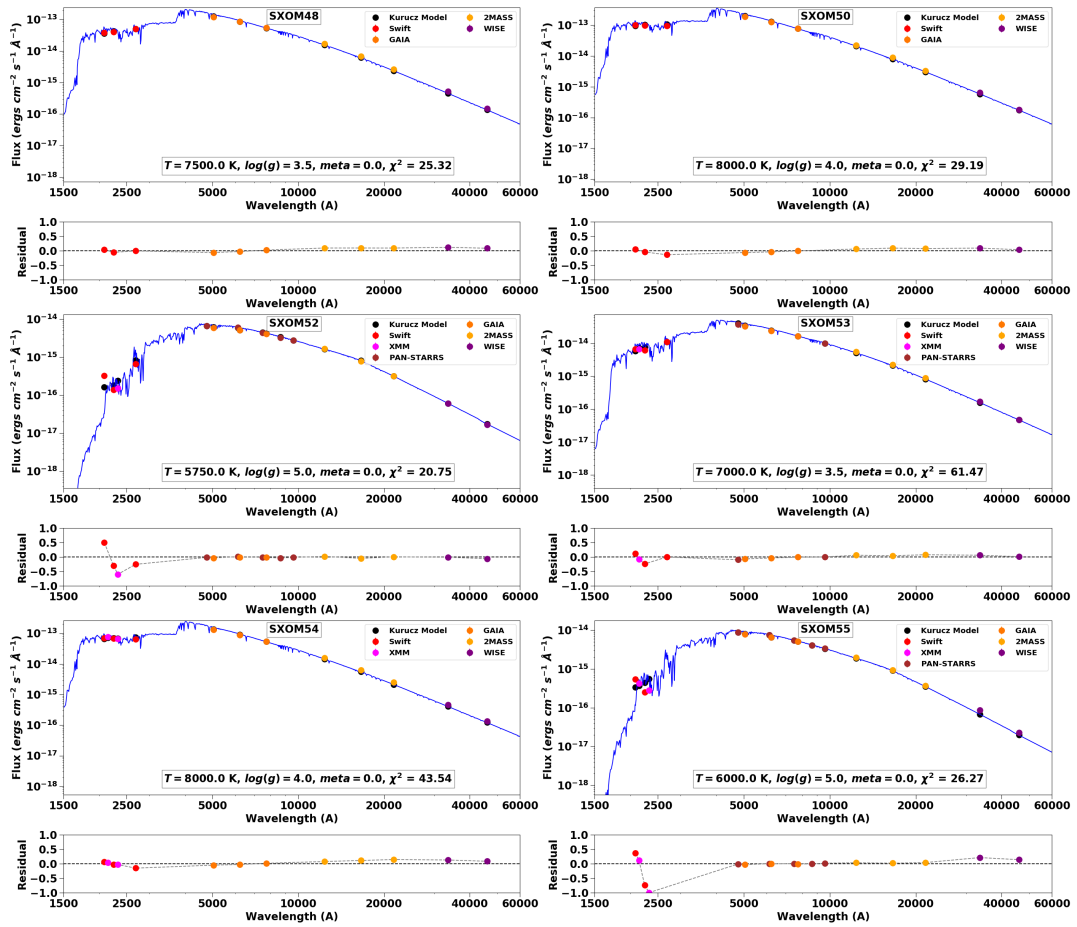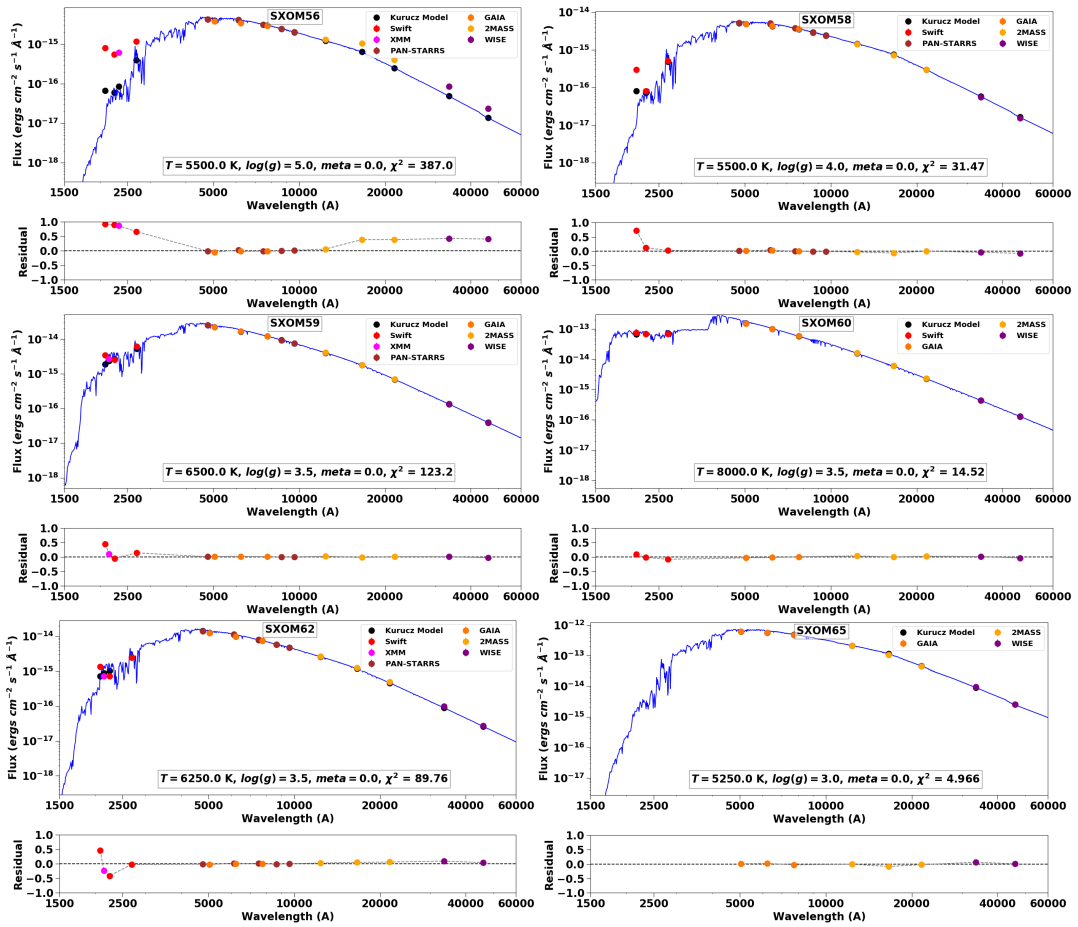Gap : Gap stars
RS : Red Straggler
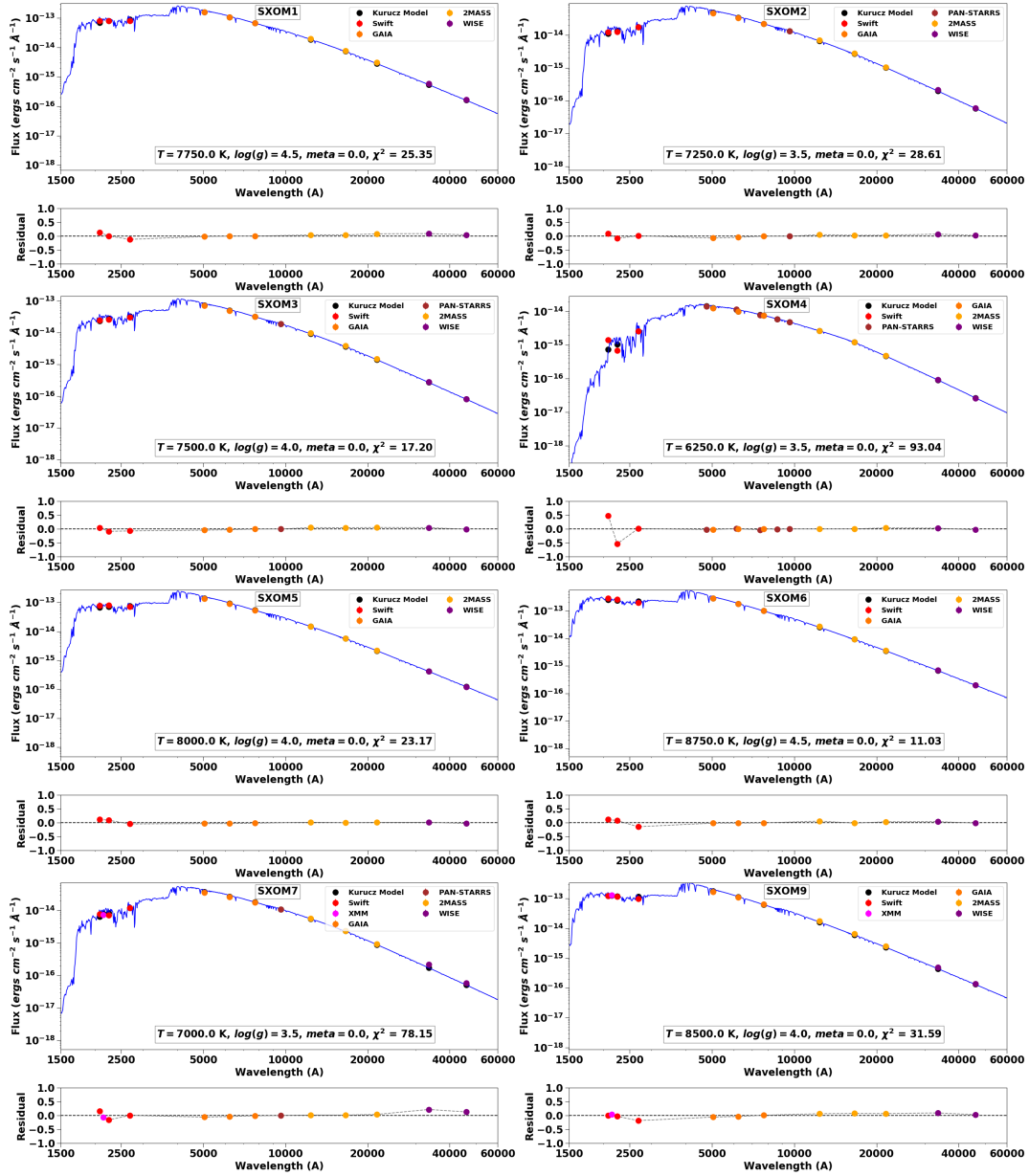
Figure C: Broad band SED of cluster members detected in Swift UVOT and XMM-OM. The blue line is the best fitting Kurucz model spectrum. Residual is defined as difference between the observed flux and the model flux, normalized by the observed flux.

SXOM24 — T = 7000.0 K, log(g) = 3.5, meta = 0.0, χ² = 35.83

SXOM25 — T = 6000.0 K, log(g) = 3.0, meta = 0.0, χ² = 48.49

SXOM26 — T = 7750.0 K, log(g) = 3.5, meta = 0.0, χ² = 18.88

SXOM27 — T = 8500.0 K, log(g) = 4.5, meta = 0.0, χ² = 20.79

SXOM29 — T = 7750.0 K, log(g) = 4.0, meta = 0.0, χ² = 20.19

SXOM33 — T = 7250.0 K, log(g) = 3.5, meta = 0.0, χ² = 64.49

SXOM34 — T = 7000.0 K, log(g) = 4.0, meta = 0.0, χ² = 111.4

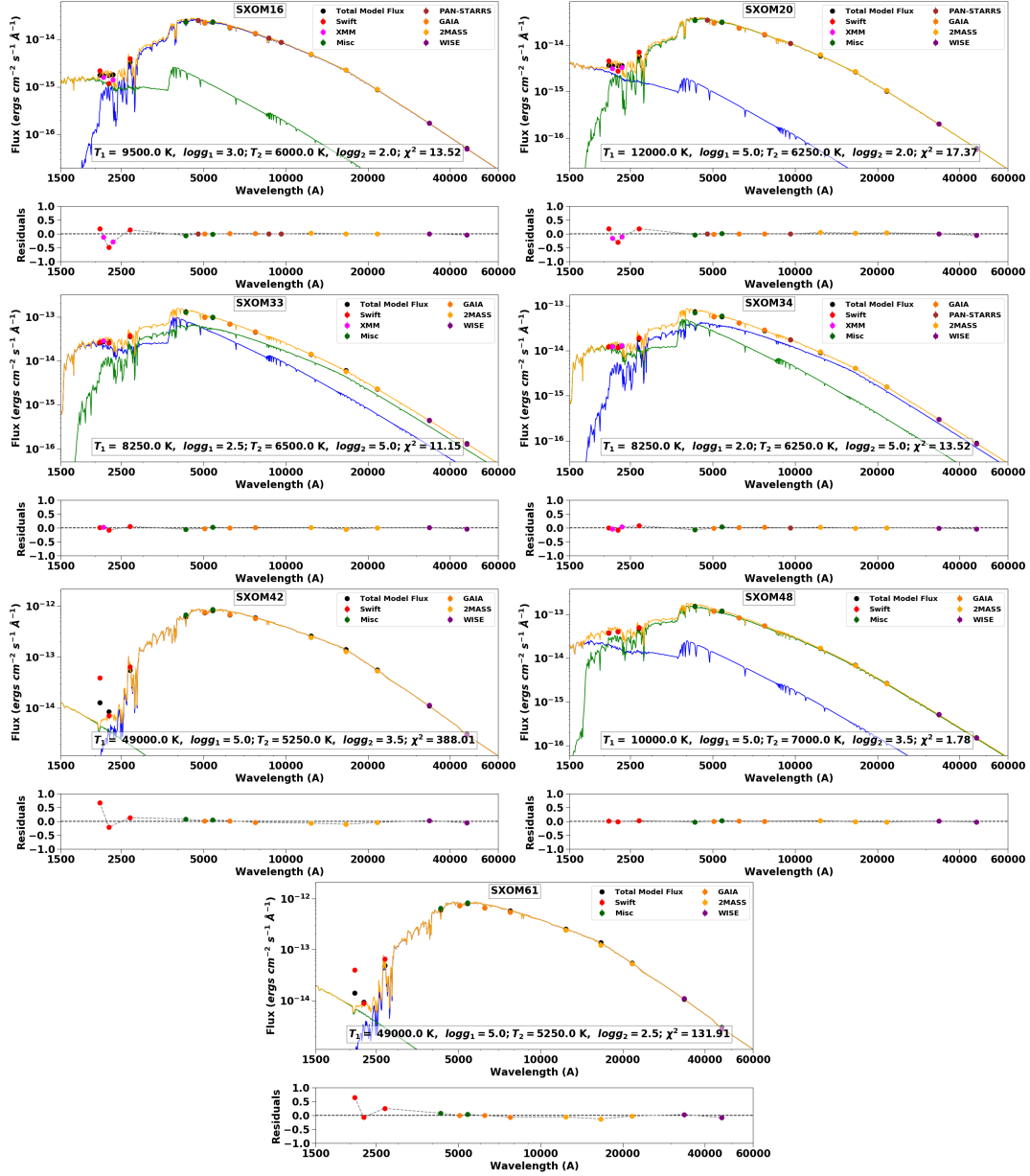SXOM35 — T = 7500.0 K, log(g) = 4.0, meta = 0.0, χ² = 19.97
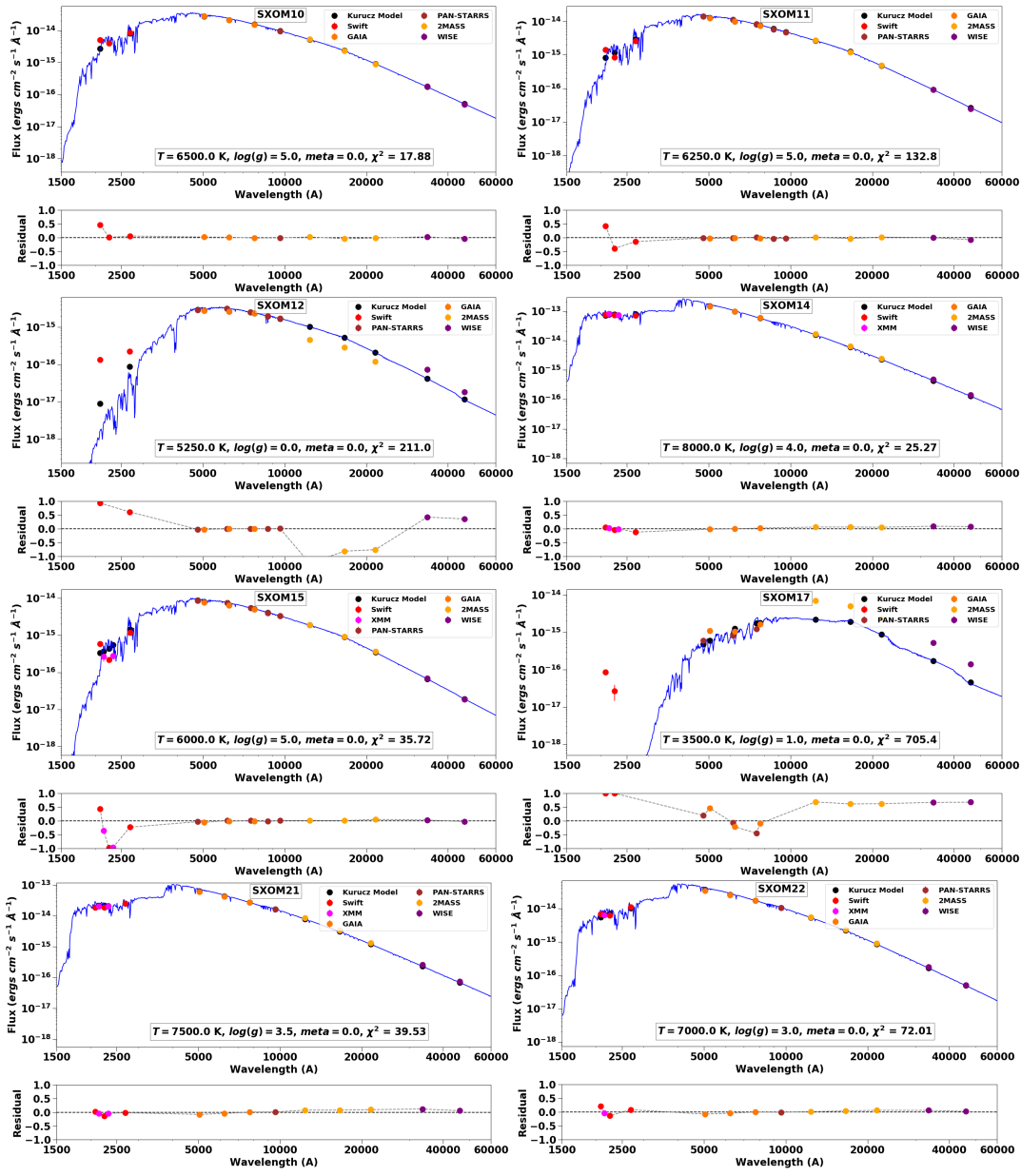
Figure D: Broad band SEDs of potential binaries. The blue and green lines are the Kurucz model spectrum and orange line is the total spectrum.